Doctoral Dissertation
Doctoral Program in Environmental Engineering (38^{th}cycle)

Evaluating Blue Water Demand and Alpine Green Water Supply for Italian Agriculture

Agro-hydrological and moisture tracking modelling applied to the Alps and Pianura Padana system

By

Nike Chiesa Turiano

******

Supervisor(s):
Prof. Luca Ridolfi, Supervisor
Prof. Francesco Laio, Co-Supervisor
Prof. Marta Tuninetti, Co-Supervisor

Doctoral Examination Committee:
Prof. Franziska Aemisegger, University of Bern
Prof. Stefano Ferraris, University of Torino
Prof. Stefania Tamea, Politecnico di Torino
Prof. Daniel Viviroli, University of Zurich

Politecnico di Torino
2026

Declaration

I hereby declare that, the contents and organization of this dissertation constitute my own original work and does not compromise in any way the rights of third parties, including those relating to the security of personal data.

Nike Chiesa Turiano
2026

* This dissertation is presented in partial fulfillment of the requirements for **Ph.D. degree** in the Graduate School of Politecnico di Torino (ScuDo).

Berg Bewegen

Acknowledgements

During these three years, I have encountered many people who contributed to this thesis both professionally and personally. As this study has shown, some connections are more visible than others, yet no less important.

First, I would like to thank my supervisors, Luca Ridolfi, Marta Tuninetti, and Francesco Laio, for their guidance and support throughout this work. Luca, thank you for always finding the time to discuss my work and for your constant encouragement, especially during moments of uncertainty. Marta, thank you for challenging my ideas and for continually offering new perspectives. Francesco, thank you for your insightful comments and valuable suggestions, which have significantly improved this work. I would also like to thank my reviewers and the members of the committee— Franziska Aemisegger, Stefano Ferraris, Stefania Tamea, and Daniel Viviroli—for the time and care they devoted to reviewing this thesis and for their valuable feedback they provided.

A heartfelt thank you goes to all my colleagues, and especially to the friends from "La Comune", who are too many to name individually and without whom I might have given up many times along the way.

I would also like to express my sincere thanks to the hydrology group in Bern, in particular Bettina Schaefli and Natalie Ceperley, for their guidance and for giving me the opportunity to spend time in such an inspiring research environment. I am also grateful to Basil and Justine for their warm welcome and for the many enjoyable moments we shared.

A special mention goes to Francesco Avanzi, who has been not only a good friend but also an important mentor throughout this journey.

Finally, I would like to thank my family and friends for their constant support, patience, and encouragement throughout these years. I am particularly grateful to

Antonio for his friendship and support, which meant a great deal during this journey. Above all, I thank my mother and father for teaching me that learning is, above all, a voluntary act.

Fundings

This study was carried out within the "National Research Centre for Agricultural Technologies – AGRITECH" and received funding from the European Union Next-GenerationEU (PIANO NAZIONALE DI RIPRESA E RESILIENZA (PNRR) – MISSIONE 4 COMPONENTE 2, INVESTIMENTO 1.4 – Avviso n. 3138 del 16/12/2021, Codice Programma CN00000022). This manuscript reflects only the authors' views and opinions, neither the European Union nor the European Commission can be considered responsible for them.

Abstract

Mountain regions and lowland agriculture are fundamental players in the hydrological cycle. Mountains act as water storage and regulators, supplying meltwater and rainwater to downstream communities, while lowland agriculture is one of the largest anthropogenic users of these water resources through irrigation withdrawals. Irrigated agriculture is responsible for 60–70% of total freshwater withdrawals with two-thirds depending directly on runoff originating in mountains. The link between mountain regions and lowland areas, however, is not limited to the supply of seasonal meltwater but expands to atmospheric moisture exchanges that contribute to local precipitation. In fact, evapotranspiration from mountain regions releases water vapour into the atmosphere, which is then transported by local winds and large-scale circulation and contributes to precipitation over lowland areas, influencing agricultural water availability. While the riverine connection depicts a giver upstream and a receiver downstream, in the atmospheric connection, the link is not unidirectional: lowland agriculture can act as a source of atmospheric moisture contributing to precipitation on the Alps.

Despite the growing attention and identification of the existing interactions between mountains and lowlands through atmospheric pathways, the connections remain poorly quantified and understood, especially for what concerns lowland agriculture. At the same time, even though riverine linkages have been more extensively studied, quantifying regional-scale agricultural dependence on irrigation water remains challenging. In the context of projected changes in river water availability, these knowledge gaps limit the effectiveness of water management and policy planning. This highlights the need for reliable agro-hydrological modelling approaches to support water governance strategies in sustainable water allocation and reducing agricultural vulnerability to climate changes.

To shed light on these gaps, we investigated mountain–lowland interdependencies through three complementary approaches: (i) the development and application of a physically-based agro-hydrological model to quantify crop irrigation water requirements; (ii) assessment of lowland dependence on alpine evapotranpiration through the quantification of Alpine contributions to lowland precipitation thanks to the coupling of moisture-tracking data and high-resolution reanalysis; and (iii) evaluation of the atmospheric moisture fluxes from lowland agriculture to high alpine catchments through the combined analysis of glacier ice samples and moisture tracking

Our results assessed the performance of the here-presented and newly developed agro-hydrological model WaterCROPv2 in evaluating irrigation water demands. We show how it is able to provide reliable estimates of irrigation water demand consistent with independent datasets and previous local studies. Applying it to the Italian maize cultivation, we proved its suitability and the advantages of using it as a decision-support tool for water management at the regional scale. The analysis identified regions where maize production is climatically sustainable and others where it is highly water-demanding, showing the application as a tool to define better water allocations. Furthermore, thanks to the flexibility of the model to test alternative irrigation strategies, simulations evaluated that a complete transition to micro-irrigation could reduce irrigation water use by an average of 21% with potential savings of up to 30–40% in areas with currently low efficiency irrigation systems. Beyond these riverine dependencies, the results also highlight the importance of atmospheric pathways linking mountain and lowland systems. Atmospheric analysis revealed that Alpine evapotranspiration contributes, on average, approximately to 5% of annual precipitation over agricultural land in the Pianura Padana, increasing to up to 7% in localized hotspots. Single sink locations highlighted the local nature of agricultural dependency from Alpine evapotranspiration, hinting at the existence of stronger convective seasonal fluxes. Furthermore, even though moisture transport from the Pianura Padana back to the Alps is weaker, localized feedbacks exist, especially between the western plain and the central Southern Alps. We show the relevance of moisture transport from lowland agricultural land to the Alps providing evidences on the detection of pesticide, agriculture-born pollutants, in the water of the high alpine SteinWasser stream. Specifically, we report the results from the field work carried out to collect ice and snow samples from the surface of Steingletscher, the glacier upstream of SteinWasser, to determine whether the glacier acts as a

secondary source of pollutants or pesticide inputs are ongoing. Moisture tracking analysis showed the marked atmospheric link to the surrounding areas, depicting potential sources of pollution.

Contents

1 Introduction **1**

1.1 Major players: Italian agriculture and the Alps 3

1.2 Agro-hydrological modelling 8

1.2.1 Timeline of agro-hydrological modelling 9

1.2.2 Modelling approaches in agro-hydrology 10

1.2.3 Spatial scale of agro-hydrological models 12

1.3 Moisture tracking modelling 17

1.3.1 Timeline of moisture tracking modelling 17

1.3.2 Types of moisture tracking models 18

2 Evaluating country-scale irrigation demand through parsimonious agro-hydrological modelling **27**

2.1 Materials and Methods 29

2.1.1 Model 29

2.1.2 Data 39

2.2 Results 45

2.2.1 Evaluation 46

2.2.2 Examples of model application 49

2.3 Sensitivity analysis 55

2.4 Conclusions and recommendations 57

3 Hydroclimatic link between the Alps and agriculture in the Pianura Padana region 59

3.1 Data and Methods . . . 60

3.1.1 RECON and ERA5-Land consistency . . . 63

3.1.2 Major players: RECON, Pianura Padana and the Alps . . . 66

3.2 Results and Discussion . . . 70

3.2.1 The Alps as sink and source of moisture . . . 70

3.2.2 Alps-agricultural land link . . . 97

3.3 Conclusions . . . 109

4 Field and Lab activities 111

4.1 SteinWasser discharge estimation and lab uncertainty analysis . . . 113

4.1.1 River discharge estimation through salt slug method . . . 113

4.1.2 SteinWasser discharge evaluation . . . 119

4.1.3 Results and Discussion . . . 125

4.1.4 Conclusions . . . 130

4.2 Steingletscher glacier sampling for pesticides and PFAS transported by incoming moisture fluxes . . . 130

4.2.1 Sampling campaign . . . 131

4.2.2 Origin of pesticide and PFAS traces in SteinWasser: glacier samples and moisture tracking . . . 140

4.2.3 Results and discussion . . . 140

4.2.4 Conclusions . . . 144

5 Conclusions 146

References 150

Chapter 1

Introduction

Worldwide, mountain regions play a fundamental role in regulating the hydrological cycle and supplying water to downstream communities [1, 2]. At the same time, lowland agricultural systems represent one of the largest anthropogenic modifiers of these water resources through irrigation withdrawals [3, 4].

Globally, irrigated agriculture supports roughly 40% of the food production and is responsible for 60–70% [4, 5] of total freshwater withdrawals with two-thirds depending on essential runoff contributions from mountains [6]. This pressure is expected to intensify under climate change, as shifts in precipitation patterns and rising temperatures are likely to increase agricultural reliance on riverine water [7, 8]. At the same time, changes in snow and glacier melt dynamics are altering the timing and availability of mountain-derived water, even in traditionally water-rich regions [9, 10].

Frequently, the mountain–lowland connection is depicted so that mountains sustain the lowland agriculture through river discharge fed by seasonal snowmelt and rain. However, this view captures only part of the coupling between highlands and lowlands. Lowland agriculture can depend on mountain regions through two complementary pathways. The first is the classical riverine connection thanks to which mountain regions supply water to the plains for irrigation purposes through river discharge [11, 12]. The second, less commonly highlighted, is an atmospheric pathway, through which mountain evapotranspiration influence lowland precipitation. In fact, evapotranspiration from mountain regions releases water vapour into the atmosphere, which is then transported by winds and large-scale circulation and

contributes to precipitation over lowland areas also influencing local agriculture water availability. It is also important to note, how this coupling is not unidirectional. Lowland areas themselves can act as sources of atmospheric moisture contributing to precipitation on the Alps. A few studies [13, 14] even reported how irrigated agriculture regions provide substantial precipitation to mountain regions, acting not only as recipient but also as a source of water.

Despite the growing attention and identification of the existing interactions between mountain and lowland through atmospheric pathways, the connections remain poorly quantified and understood, especially for what concerns lowland agriculture. At the same time, even though riverine linkages have been more extensively studied, quantifying regional-scale agricultural dependence on mountain water through river abstractions remains challenging. In the context of projected changes in river water availability, these knowledge gaps limit the effectiveness of water management and policy planning. This highlights the need for reliable agro-hydrological modelling approaches to support water governance strategies in sustainable water allocation and reducing agricultural vulnerability to climate variability.

Within this context, this study evaluates the riverine and atmospheric dependence and interconnection between lowland agriculture in the Pianura Padana and the Alpine region. Specifically, we propose and apply a physically-based agro-hydrological model to quantifies the volume of irrigation water (blue water) that should be abstracted from Alpine-fed rivers to sustain crop production, and we assesses the contribution of the Alps to precipitation (green water) supporting agricultural systems in the Pianura Padana through atmospheric moisture tracking analyses. The bidirectional interconnection between agricultural land and the Alps is further highlighted revealing the role of agricultural land in alpine precipitation and in the transport of agriculture-born pollutants to high alpine catchment. Evidence of this latter process are reported thanks to the combined study of ice samples from the alpine Steingletscher glacier and moisture tracking.

The following chapters describe the methodological workflow adopted to answer the research question. The present Chapter introduces the broader context by describing the main characteristics of Italian agriculture, the hydro-climatic role of the Alps, and the principles of agro-hydrological and moisture tracking modelling. Chapter 2 presents the agro-hydrological model developed to estimate the riverine dependence of maize cultivation in Italy through the quantification of its irrigation water demand.

Chapter 3 investigates the bidirectional moisture exchange between the Alpine region and the agricultural areas of the Pianura Padana, with a specific focus on the role of the Alps as both a sink and a source of atmospheric moisture. Chapter 4 highlights the importance of moisture transport from lowland agricultural areas to high-elevation Alpine environments through detailed field and laboratory analyses of pesticide traces detected in meltwater discharged from the alpine glacier, Steingletscher.

1.1 Major players: Italian agriculture and the Alps

Italian agricultural land Agriculture represents a fundamental sector both for Italy and for Europe. In fact, together with the agri-food sector, it represents, 17% of the country's GDP making Italy one of the largest agricultural producers and food processors in the EU [15]. Thanks to the strong spatial heterogeneity in climate, soils and water availability, Italy is able to produce a wide range of agricultural goods. The northern regions are well known for grains, soybeans, rice and fruit production, while the mediterranean south is specialized in fruit, especially citrus, vegetables, olives, and vine. Agricultural productivity is concentrated in lowland and coastal regions, with the Po Valley, called Pianura Padana, representing one of the most intensively cultivated and economically important agricultural areas in Europe (Figure 1.1).

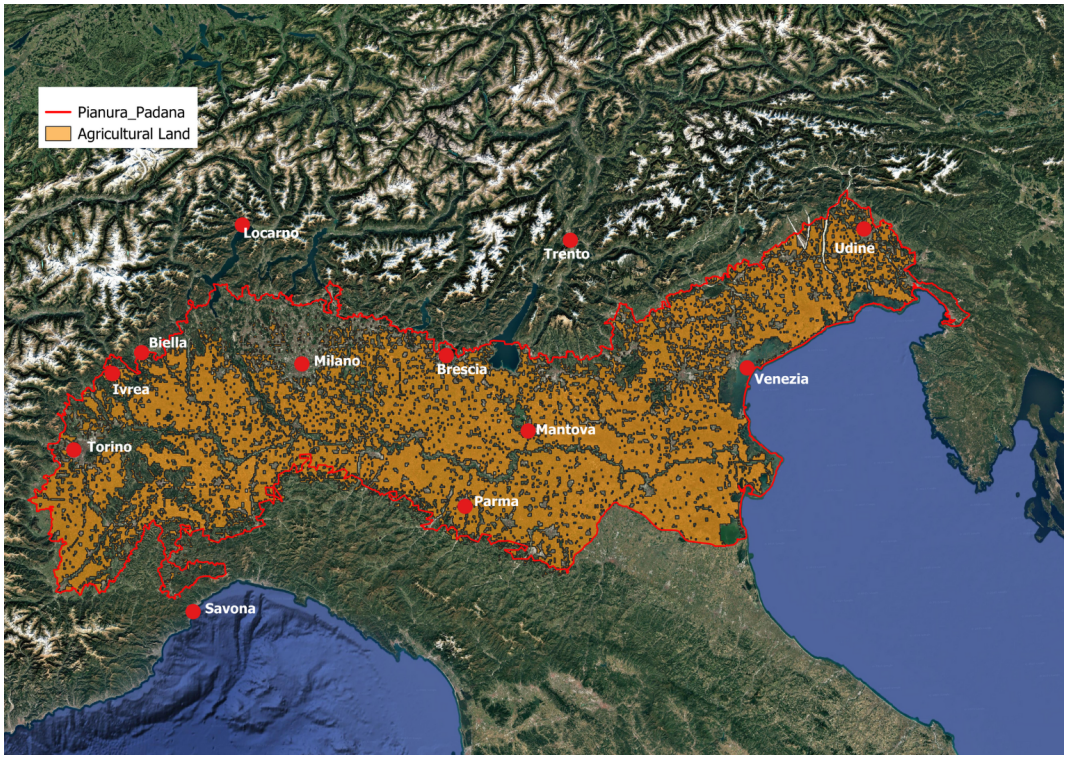

Fig. 1.1. In red the the borders of Pianura Padana, in orange agricultural land derived from the FAO GCL-SHARE dataset [16]. Visualization according to the coordinate reference system WGS 84 / UTM zone 32N (EPSG:32632).

Pianura Padana produces almost 35% of all crops farmed in Italy [17]. The important role of agriculture in this region is reflected by the fact that 41% of the utilized agricultural area is irrigated, with the remaining 59% managed under rainfed conditions [18]. Most of the irrigated areas, furthermore, host water-intensive crops such as rice and maize, which are the key cash-crop of the region accounting for 50% and 90% of the total national maize and rice production [19].

Pianura Padana receives relatively a large amount of precipitation ranging from 800 to 1500 mm/yr with higher values close to the alpine slopes due to orographic enhancement. Rainfalls are unevenly distributed thought the year and, being mainly concentrated in winter, often mismatch the increasing water demand during the summer growing season. This implies strong irrigation requirement and subsequent river withdrawals [17, 20]. It has been estimated that in Pianura Padana, irrigated agriculture abstracts 12 billion m^3 of water every year, accounting for 60% of total abstractions and being the major player in riverine water use [21]. This highlights the importance of precipitation patterns not only locally but also in the mountainous

regions of the catchment that provide lowland with seasonal river discharge. Even though historically the hydro-climatic conditions in Pianura Padana have been favorable for agricultural production, in the recent years the whole mediterranean areas has experienced a reduction in summer rainfall [21] and in increase in frequency and severity of drought events [17, 22, 23]. The extreme 2022 drought that Pianura Padana experienced is an example of the strong correlation between the hyro-climatic conditions in the alpine regions and the ones that develop in the lowland. In fact this drought was characterized by a strong winter snow deficit in the Alps, reduced spring precipitation, and persistent summer heatwaves in the lowland, leading to widespread irrigation restrictions and significant production losses across the basin [21, 24]. This event highlighted the vulnerability of Pianura Padana agriculture and the dependence on precipitation and river water inputs. Thus, in this context, the spatial and temporal distribution as well as the origin of the precipitation play a major role in determining the vulnerability of Italian agriculture. In this regard, the Alps play a multi-faceted role on Italian agriculture as they provide riverine water but also influence large-scale atmospheric moisture transport, and provide moisture themselves for lowland precipitation formation. Understanding the role of the Alps not only as source of river discharge but also as precipitation source helps disentangling the dependence between high and low lands.

The Alps The Alps represent a key component of the European hydrological cycle by receiving precipitation, directly feeding river flow, storing water seasonally in the form of snow, ice, and soil moisture, and releasing it to downstream regions through both river discharge and atmospheric pathways supporting lowland water availability [1, 25, 26]. When talking about the Alps, different definitions can be found according to the source and what the definition is intended for. In this study, we adopt the definition provided by the Alpine Convention, which delineates the Alps as the entire area enclosed by the red boundary shown in Figure 1.2. This definition is based on geographic extent rather than elevation and therefore includes both high-altitude environments and valley floors within the mountain system. Such a broad definition aligns with the objective of this work, as our aim is to assess the contribution of the alpine region to lowland agriculture, not only the relief. For this reason, the entire Alpine area is considered, regardless of altitude.

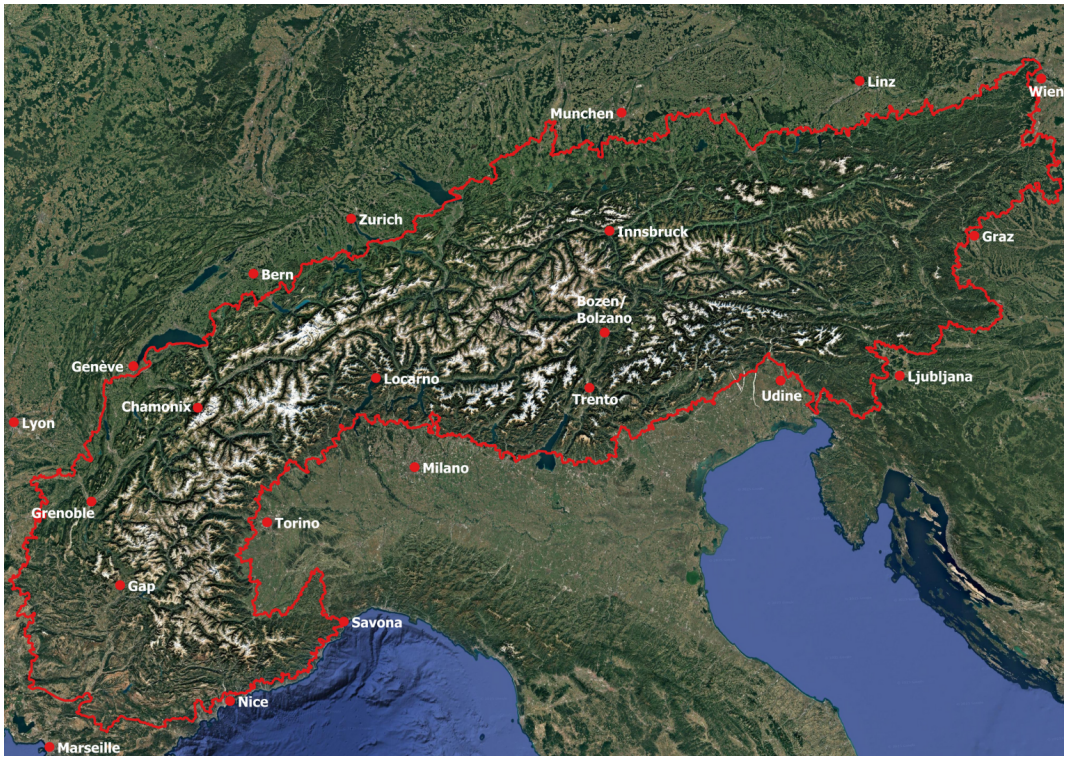

Fig. 1.2. In red the definition of the borders of the Alps according to the Alpine Convention. Visualization according to the coordinate reference system WGS 84 / UTM zone 32N (EPSG:32632).

The Alpine arc represents, as a whole, one of the most important orographic barriers in Europe and has a major impact on atmospheric circulation, moisture transport, and precipitation patterns across the continent. Extending over more than 1,000 km with an area of more than 190'000 km^2 and reaching elevations above 4,000 m, the Alps interact with atmospheric flow across a wide range of spatial and temporal scales, from synoptic-scale circulation to mesoscale and boundary-layer processes. Through these interactions, the Alps affect the atmospheric airflow and the relative moisture transport, influencing both mountain and lowland hydro-climatic conditions. At the synoptic scale of 1,000–3,000 km and several days, the Alps interact with the tropospheric large-scale pressure systems, frontal structures, and extratropical cyclones that control the advection of moist air masses toward Central Europe. The main moisture transport from the North Atlantic and the Mediterranean is related to these synoptic systems and its local redistribution is determined by the interaction with the Alpine barrier [27]. At this scale, the main influence that the Alps have on

atmospheric circulation is the blocking and deflection of the air flow. According to the stratification of the incoming airflow, in fact, mountains can block and deflect the air masses or force them to uplift and lose humidity. When the air density varies with height due to temperature gradients, the resulting buoyancy forces have a stabilizing effect that prevents vertical motion. Thus, air masses are partially blocked and forced to diverge horizontally around the Alps rather than overpassing them, resulting in the windward side receiving more moistured air [28]. These conditions are common in winter and under persistent high-pressure situations [29]. On the contrary, when stratification is weaker, air flows, encountering the mountain range, are uplifted and can cross over the Alps, transporting moisture to the leeward side. These interactions between synoptic-scale transport and the Alps have a major role in defining whether moisture is transported across the Alps or redistributed along its sides, with direct impact on precipitation patterns upstream and water availability downstream.

At the mesoscale of 10-500 km and from hours to days, The Alps have a strong effect on inducing local precipitation. Major examples are the topographic uplift or air masses and mesoscale flow channeling through the valleys [30]. The topographic uplift is the process that strongly contributes to inhomogeneities in precipitation patterns between the opposite sides of ranges. Uplifting air cools down with a consecutive reduction in dew point values. If the cooling of the air is important enough to reach condensation, precipitation occurs on the windward side and releases drier air on the leeward side [31]. This causes a rain-shadow effect as the adiabatic warming on the leeward side reduces the specific humidity and inhibits precipitation. This mechanism leads to drier conditions in regions such as the inner alpine valleys and parts of the Po Basin; valley channeling, instead, causes inhomogeneities within valley as it contributes to the transport of moisture to specific regions. In fact, the lateral confinement imposed by valley walls induces the mesoscale airflow to follow constrained geometries, forcing winds to align with valley orientations rather than with the large-scale geostrophic flow.

Within the first 1-2 km of the atmosphere and within timescales of minutes to hours, the Alps have an impact on the processes occurring within the boundary layer through the exchange of heat and moisture between its surfaces and the air masses. Over the complex alpine terrain, the atmospheric boundary layer is strongly influenced by slope and valley winds, diurnal heating contrasts, and surface heterogeneity. These features have a strong impact on convective processes affecting local precipitation and vertical vapor distribution. During the day, this interaction enhances turbulent

mixing and upslope flows that can transport moisture from the surface into the free troposphere, while at night, the cooling and downslope winds tend to reduce vertical exchange. Studying these interactions is relevant for understanding the extent of the influence that the Alps exert well beyond the mountain range, besides the riverine aspects. In fact, changes in precipitation pattern not only impact the magnitude of seasonal water availability in rivers but also the delayed moisture release to the atmosphere from snow-covered surfaces. Furthermore, strong orographic precipitation may locally intensify flood risks, while reduced moisture transport across the Alps during blocked conditions influences soil moisture deficits and atmospheric dryness that, in turn, can propagate as droughts in downstream regions. While the hydrological role of the Alps as a source of river discharge has been extensively studied, their function as an atmospheric moisture player is less fully quantified, particularly in relation to agricultural water availability. Understanding how Alpine orographic processes interact with atmospheric circulation is therefore essential for a comprehensive assessment of mountain–lowland connectivity and for anticipating future changes in hydro-climatic conditions under climate warming.

Given the complexity of interactions between climate, atmospheric moisture transport, hydrology, and agricultural water use in the lowland, hybrid agro-hydrological models provide essential tools for analysing Italian agricultural systems.

In particular, linking agro-hydrological modelling with atmospheric moisture tracking offers a promising framework for disentangling the contribution of Alpine processes to precipitation over agricultural regions. Such an approach supports a more physically consistent assessment of mountain–lowland connectivity and provides insights into how changes in Alpine hydro-climatic dynamics may affect agricultural water availability in Italy under future climatic conditions.

1.2 Agro-hydrological modelling

Agro-hydrological models are numerical models developed to estimate water fluxes in the soil-plant-atmosphere continuum (SPAC). They were first developed in order to respond to the increasing demand for efficient agricultural water use, to understand SPAC functioning, and to assess the environmental impact of agriculture across spatial and temporal scales.

1.2.1 Timeline of agro-hydrological modelling

The earliest agro-hydrological models started appearing around mid-20th century, with simplified approaches based on simple water balance approaches and that strongly relied on field observations and empirical relationships [32, 33].

A major milestone was the development of the physically-based evaporation formulation by Penman in 1948 [33]. He provided an equation that related evaporation to radiation, temperature, humidity, and wind speed. Subsequent lysimeter studies provided empirical estimates of crop water use and laid the foundation for crop water requirement calculations [34]. The approaches, however, were still limited in the number and accuracy of represented processes. In the 1960s and 1970s, advances in computational power allowed Richards' equation for unsaturated flow [35] to be introduced in agro-hydological modelling. This allowed the vertical soil moisture dynamics, including infiltration and drainage, to be described in models [36]. At the same time the concept of the soil–plant–atmosphere continuum (SPAC) started emerging, emphasizing the role of water as the connector of soil and atmosphere through plants [37, 38]. These developments laid the foundation for integrating soil hydrology with plant water uptake. In fact, from the late 1970s onwards, agro-hydrological models increasingly combined soil water balance with crop growth and phenological development. Early crop simulation models such as CERES [39], WOFOST [40], and EPIC [41] incorporated water stress functions to link soil moisture deficits with reductions in photosynthesis, biomass accumulation, and yield.

During the 1990s, agro-hydrological modelling expanded to catchment and basin scales driven by an increased concern on the diffusion of pollution. For this reason, models such as SWAT [42] and MIKE-SHE [43] integrated agricultural water use with surface and groundwater processes, which enabled the assessment of nutrient transport and the cumulative impacts of agricultural management practices [44–46]. In the 2000s, increasing computational power facilitated the development of more detailed coupled soil–plant–atmosphere models, with explicit representation of root water uptake, transpiration, and energy balance processes. The release of AquaCrop by FAO [47] provided a parsimonious yet robust model focused on water productivity, making agro-hydrological modelling more accessible for water management and policy applications, particularly in data-scarce regions. Another turning point in agro-hydrological modelling arrived in the 2010s when the widespread availability

of satellite observations enabled the integration of remote sensing data [48, 49]. Traditional agro-hydrological models rely on point-based measurements (e.g., rain gauges, soil moisture probes), which often fail to capture spatial heterogeneity but remote sensing, providing spatially continuous observations over large areas, enables models to represent spatial variability in evapotranspiration, vegetation cover, and soil moisture more realistically. Furthermore, remote sensing-based energy balance approaches allow direct estimation of actual evapotranspiration (ET), rather than relying solely on empirical crop coefficients.

In parallel with field and catchment-scale agro-hydrological models, large-scale agro-hydrological models, such as LPJmL [50], were formulated. They were developed to respond to the increasing demand for regional support and global assessments of agricultural water use and food security under climate change scenarios [51–53].

The most recent developments are focusing on hybrid approaches that combine process-based agro-hydrological models with machine learning and data-driven techniques for precision irrigation, climate adaptation planning, and integrated water–food–energy nexus analyses [54, 55].

Overall, agro-hydrological modelling has evolved from empirical water balance approaches focused mainly on the soil water dynamics to integrated, multi-scale frameworks that couple hydrological processes with crop growth but also with food and energy production compartments. This progression reflects an ongoing trade-off between model complexity, data requirements, and applicability.

1.2.2 Modelling approaches in agro-hydrology

Agro-hydrological models can be broadly distinguished according to how hydrological and crop processes are represented, independently of the spatial scale at which they are applied. Traditionally, agro-hydrological modelling has relied on process-based formulations, in which water fluxes and state variables are governed by conservation laws and empirically parameterized process relationships. In recent years, however, increasing data availability and computational capacity have enabled the development of data-driven and hybrid modelling approaches, which complement or partially replace process representations with statistical or machine-learning techniques.

Data-driven agro-hydrological models infer relationships between inputs (e.g. climate variables, remote sensing indicators) and outputs (e.g. evapotranspiration, soil moisture, yield) directly from observational data, often achieving high predictive skill within the range of observed conditions. Hybrid approaches combine data-driven components with process-based cores, preserving physical consistency while improving parameter estimation, state updating, or sub-process representation. Importantly, these modelling paradigms are not associated with a specific spatial scale and can be applied across field-, catchment-, and large-scale agro-hydrological models, modifying how processes are represented rather than redefining the underlying model structure.

Process-based Models Process-based agro-hydrological models represent soil, plant, and atmospheric processes through explicit formulations derived from conservation laws and empirically parameterized physical relationships. Water fluxes such as infiltration, evapotranspiration, runoff, and drainage are computed by solving water balance equations at the soil–plant or land-surface level, while crop growth is simulated through process representations of phenology, biomass accumulation, and stress responses. The key strength of process-based models lies in their physical interpretability and extrapolation capability, allowing them to be applied under changing climatic or management conditions, provided that model assumptions remain valid. However, their performance is often constrained by parameter uncertainty, structural simplifications, and the availability of detailed input data, particularly when applied over large spatial domains.

Data-driven Models Data-driven agro-hydrological models infer relationships between inputs and outputs directly from observational data using statistical or machine-learning techniques, without explicitly representing the underlying physical processes. These models are trained on historical datasets -— often including meteorological observations, remote sensing products, and in situ measurements -— to predict variables such as evapotranspiration, soil moisture, streamflow, or crop yield. Data-driven approaches can achieve high predictive accuracy within the range of observed conditions and are particularly effective when physical processes are poorly understood or difficult to parameterize. However, their reliance on data availability limits their robustness under extrapolation, and the lack of explicit

physical constraints can reduce interpretability and increase the risk of non-physical predictions under novel climate or management scenarios.

Hybrid approaches Hybrid agro-hydrological models combine process-based model structures with data-driven components in order to leverage the strengths of both paradigms. In these approaches, physical models provide a consistent framework for water and mass conservation, while machine-learning or statistical methods are used to improve parameter estimation, update model states, emulate computationally expensive sub-processes, or correct systematic model errors. Hybrid approaches are particularly well suited for applications involving data assimilation, precision irrigation, and climate adaptation planning, where observational data can be used to constrain model uncertainty in near–real time. While hybrid models offer improved predictive skill and flexibility, they also introduce additional complexity, requiring careful design to ensure physical consistency, transparency, and transferability across spatial scales and environmental conditions.

These modelling approaches are orthogonal to the classification of agro-hydrological models based on spatial scale and can be applied within field-scale, catchment-scale, and large-scale modelling frameworks.

1.2.3 Spatial scale of agro-hydrological models

Field-scale models. Field-scale agro-hydrological models are applied for irrigation scheduling, water productivity analysis, and the assessment of crop responses to water stress. These models explicitly simulate the soil water balance within the crop root zone and its coupling with crop growth processes. They typically operate at daily or sub-daily temporal resolution and represent the soil profile as a one-dimensional vertical domain extending from the soil surface to the lower boundary of the root zone or to the groundwater table.

At the core of these models, there is the water balance expressed as:

$$\Delta WC = P + I - ET - R - D \tag{1.1}$$

where P denotes precipitation, I irrigation, ET actual evapotranspiration, R surface runoff, and D deep percolation losses below the root zone. The change in soil

water storage (ΔWC) represents the integrated water content of the root zone rather than point-scale volumetric soil moisture. Most field-scale crop models adopt bucket-type representations of vertical soil water movement, rather than explicitly solving Richards' equation for unsaturated flow [35] despite operating at spatial scales where such solutions would be feasible. This choice is driven by the reduced data requirements and the higher computational efficiency. Vertical distribution of water is commonly represented by a tipping-bucket approach, which results in drainage occurring once soil water content exceeds field capacity. This simplification reduces data and computational requirements, but gives a simplified vision of the soil dynamics.

Crop development within these models is driven by phenological progression based on the accumulated thermal time, while biomass production is computed either from intercepted radiation or from transpiration-based water productivity relationships, depending on model structure. Soil water availability regulates water stress, which, with a cascade effect, governs processes such as transpiration, leaf expansion, photosynthesis, and biomass formation.

In models such as CERES [39] and WOFOST [40], water stress reduces biomass accumulation through multiplicative stress factors acting on crop growth and yield formation processes. In contrast, AquaCrop [47] adopts a more parsimonious formulation, explicitly linking biomass production to cumulative crop transpiration via conservative water productivity parameters.

Generally, in field-scale agro-hydrological models, variables are updated at each time step, such that soil moisture deficits immediately propagate to crop responses. Boundary conditions are defined by atmospheric forcing at the soil surface and either free drainage or fixed water table conditions at the lower boundary. Agricultural management practices, including irrigation timing and depth, planting dates, and cultivar selection, are prescribed explicitly, allowing scenario-based evaluation of water management strategies.

Catchment-scale models. Catchment-scale agro-hydrological models are applied to assess the integrated impacts of agricultural activities on water quantity and quality at the watershed or river-basin scale. Their primary applications include the evaluation of nutrient and sediment transport, allowing for the assessment of cumulative effects of land-use and agricultural management practices on the hydro-

logical systems. Unlike field-scale models, these models explicitly represent lateral water fluxes and include spatial heterogeneity in climate, soils, topography, and land management.

Catchment-scale models typically operate at a daily time step and discretize the basin into spatial units, hydrological response units (HRUs), characterized by homogeneous land use, soil properties, and topographic attributes. Within each spatial unit, soil water processes are represented in a vertically aggregated manner, while horizontal fluxes connect units through surface runoff, interflow, and groundwater flow pathways.

At the core of catchment-scale agro-hydrological models lies the catchment water balance, which can be expressed as:

$$\Delta S = P - ET - Q - G \tag{1.2}$$

where ΔS is the variation in total water storage within the catchment, P is precipitation, ET is actual evapotranspiration, Q represents surface and subsurface runoff contributing to streamflow, and G denotes groundwater outflow or deep percolation leaving the model domain. Storage changes may include soil moisture, shallow groundwater, and channel storage components.

Within individual spatial units, soil water balance formulations similar to field-scale models are applied; vertical soil water movement is typically represented through parameterizations based on soil hydraulic properties, slope, and moisture status, allowing computationally efficient simulation at the basin scale [42, 43]. In fact, at these scales, the explicit numerical solution of Richards' equation [35], would be computationally prohibitive. Agricultural water use is represented through irrigation abstractions from surface water or groundwater sources, which are coupled to the hydrological system by reducing available streamflow or groundwater storage. ET is typically calculated using reference evapotranspiration methods combined with land-use-specific parameters, while crop growth is often represented in a simplified manner through crop calendars and management schedules. In models such as SWAT [42], agricultural land is aggregated into HRUs, within which crop growth and soil water processes are simulated independently of their spatial location, and lateral fluxes are routed through the river network. In contrast, fully distributed models such as MIKE-SHE [43] explicitly couple surface flow, unsaturated zone processes, and groundwater

flow, providing a more physically-based representation of the interactions between surface and subsurface, with, however, higher computational costs. Catchment-scale agro-hydrological models frequently incorporate nutrient and sediment transport modules, allowing simulation of diffuse pollution from agricultural land. Nutrient cycling is driven by soil moisture dynamics, runoff generation, and management practices such as fertilization and tillage, enabling assessment of non-point source pollution and water quality responses to land-management scenarios [46**?**].

Model state variables are updated sequentially at each time step, with strong coupling between soil water, runoff generation, groundwater flow, and channel routing processes. Boundary conditions are defined by meteorological forcing at the land surface and prescribed hydraulic conditions at basin outlets. Agricultural management practices, including irrigation withdrawals, fertilization rates, and crop rotations, are defined as inputs, allowing scenario-based analysis of the cumulative hydrological and environmental impacts of agricultural systems.

Large-scale models. Large-scale agro-hydrological models are designed to assess agricultural water use, crop production, and water availability at regional to global scales, to assess climate change impacts and support food security analyses, and water–food–energy nexus studies. Their applications focus on highlighting large-scale patterns and long-term trends rather than providing site-specific guidance. Compared to catchment-scale models, large-scale models prioritize spatial coverage over detailed representation of local hydrological processes. These models typically operate at coarse spatial resolutions, ranging from tens of kilometers to half-degree grid cells, and are run at daily to monthly temporal resolutions over multi-decadal time horizons. The land surface is discretized into grid cells, where agricultural land is represented using imposing crop-specific cropland extension. Spatial heterogeneity in climate, soils, and land use is therefore represented through gridded input datasets rather than as hydrological units.

At the core of large-scale agro-hydrological models lies a grid-cell-based water balance, which can be expressed as:

$$\Delta S = P - ET - R - D \tag{1.3}$$

where ΔS represents the change in total terrestrial water storage within a grid cell, P is precipitation, ET is actual evapotranspiration, R denotes runoff generation contributing to river discharge, and D represents drainage or groundwater recharge leaving the soil column. Storage components typically include soil moisture and, in some models such as LPJml [50] and PCR-GLOBWB [56], shallow groundwater and snow storage, while channel routing is treated separately at the basin or continental scale. Within each grid cell, vertical soil water movement is represented using coarse formulations, often including defined storage capacities. Infiltration, percolation, and runoff generation are parameterized using empirical or semi-empirical relationships that capture average behavior at the grid-cell scale [50, 51].

Crop growth in large-scale agro-hydrological models is represented in a simplified and generalized manner, typically through crop functional types or representative crops rather than individual cultivars. Phenology is driven by temperature and photoperiod, while biomass accumulation is calculated based on radiation use efficiency or transpiration-based productivity formulations. Water stress is diagnosed from grid-cell soil moisture status and feeds back on transpiration and biomass production, allowing the estimation of yield reductions under water-limited conditions. Irrigation water use is defined as the potential irrigation demand and thus computed as the additional water required to avoid crop water stress. Irrigation withdrawals are then subtracted from surface water or groundwater stores. This approach allows for a spatial description of irrigation water demand and consumption.

Models such as LPJmL [50] integrate crop growth, irrigation water use, and terrestrial hydrology within a unified framework, enabling consistent assessments of agricultural water consumption, crop yields, and water availability across regions and continents. River routing schemes are employed to aggregate grid-cell runoff into discharge at basin outlets, allowing comparison with observed large-scale streamflow and water resource indicators.

State variables in large-scale agro-hydrological models are updated sequentially at each time step, with tight coupling between climate forcing, soil moisture dynamics, evapotranspiration, runoff generation, and crop growth. Boundary conditions are defined by gridded meteorological datasets and prescribed land-use and management scenarios. Agricultural practices such as crop distribution, irrigated area, and management intensity are typically prescribed externally, enabling scenario-based

analyses of climate change, land-use transitions, and water resource constraints at regional and global scales.

1.3 Moisture tracking modelling

1.3.1 Timeline of moisture tracking modelling

Moisture tracking modelling is the process of modelling the trajectory and the magnitude of moisture fluxes from their evaporative sources to their sinking regions through the atmospheric circulation transport. The study of moisture transport started appearing on atmospheric thermodynamics textbooks in the early 1900s with moisture budgets approaches that used water vapor continuity equations [57]. Significant mid-century advances occurred thanks to improvements in radiosondes [58], which provided vertical humidity profiles, as well as synoptic weather maps, which enabled the first attempts at observational moisture transport estimates and grid-based moisture advection calculations [59–62]. Yet, these tools, based on Eulerian budget approaches, were insufficient for detailed source attribution or regional moisture pathway reconstruction as they could not track parcels history.

The 1960s mark the first period in which physically-based moisture transport models caught on. They were based on the use of divergence of vertically integrated moisture fluxes to infer the net moisture incoming and outgoing from a region and approximate possible regions of source and sink [63–65]. However these Eulerian methods, limited by the computational power of those years, were grid-based and struggled to infer quantitative and detailed source–sink relationships.

A major transformation occurred during the 1980s, when increasing computational power made it feasible to track the movement of individual air parcels in the atmosphere. This allowed for the development of Lagrangian moisture tracking approaches which could be used to reconstruct moisture transport pathways and track humidity changes along the trajectories, identifying evaporation and precipitation events. One of the first widely used trajectory models was FLEXTRA, developed by Stohl et al. in 1995, which enabled the computation of forward and backward trajectories for the analysis of long-range air-mass transport and source–receptor relationships [66]. Developed within the same framework, the FLEXPART model was introduced in 1998 as a Lagrangian particle dispersion model capable of simulating

the transport and dispersion of atmospheric tracers by incorporating parameterizations of turbulence and convection [67–71]. Around the same period, in 1997, the LAGRANTO model was developed by Wernli and Davies [72]. A further refinement of Lagrangian moisture tracking was introduced by Sodemann et al. in 2008 with source and sink diagnostics. Sodemann et al. presented the WaterSip model, a mass-budgeting diagnostic method that allows for determining precipitation sinks and evaporation sources by analysing humidity changes along air-parcel trajectories while enforcing moisture conservation [69].

A new jump forward was taken in the 2010s with the coupling of tracking models (both Lagrangian and Eulerian [73, 74]) with reanalysis datasets such as ERA-Interim [75] and ERA5 [76]. These datasets, in fact, provided new spatial and temporal detailed inputs. With this update, the models improved the representation of weather systems, atmospheric rivers, monsoon circulation, and extreme events as drought and floods. Eulerian water vapour tagging also entered a new era with the implementation of numerical tracers into regional numerical models such as the COnsortium for SMall-scale MOdeling COSMO model [77].

Additionally, isotope-enabled climate models increased in popularity. These models simulate the fractionation of stable water isotopes as Oxygen-18, δ^{18}O, and Deuterium, δD, during evaporation and condensation, allowing researchers to connect atmospheric moisture pathways with stable isotope observations in rainfall, snowfall, and ice cores [78–82]. Recent advances in global cloud-resolving models (NICAM [83], COSMOiso [84], DYAMOND [85], ICON [86], and SAM [87]) now permit explicit simulation of convection at kilometer-scale resolution, improving moisture transport representation and reducing reliance on parameterizations. The general tendency is to bring moisture tracking models to turn from diagnostic to predictive tools in order to help the prediction of hydrological extreme events and long-range precipitation teleconnections.

1.3.2 Types of moisture tracking models

Nowadays there are two types of moisture tracking models: Eulerian and Lagrangian (Figure 1.3). Eulerian models are 3D grid-based and at each time step the moisture content in each grid cell is updated on the base of wind incoming and outgoing from the cell, precipitation and evapotranspiration fluxes. Lagrangian models, instead, are

trajectory-based and track the moisture content of moving air parcels according to 3D wind fields, precipitation and evaporation fluxes.

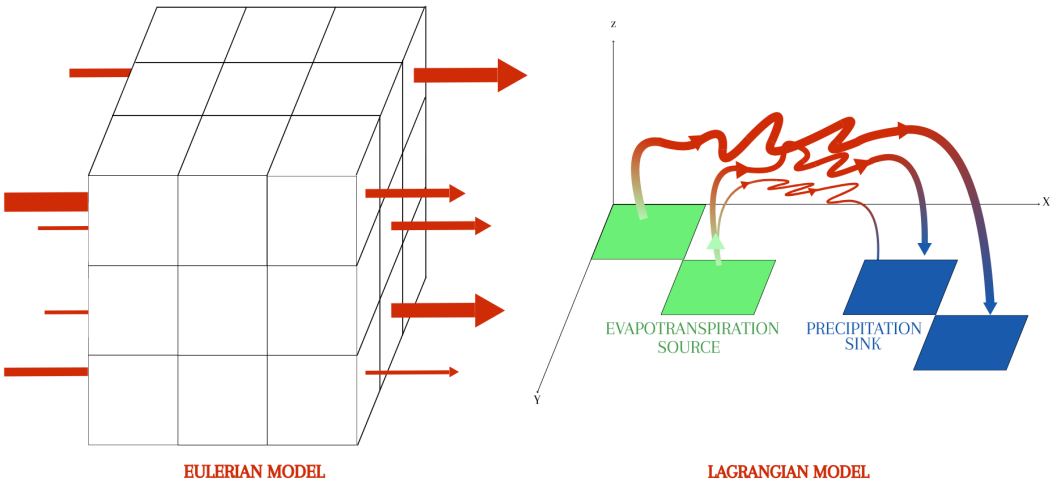

(a) (b)

Fig. 1.3. Graphical representation of (a) 3D grid-based Eulerian model: every grid cell has a moisture content which is updated according to incoming and outgoing fluxes (red arrows), (b) trajectory-based Lagrangian model: parcels moved in the atmosphere following 3D wind field and their trajectory (red arrows) is followed from evaporation sources (green cells) to precipitation sinks (blue cells)

Eulerian models. Classical Eulerian models are based on the principle of studying moisture transport through the evolution of the atmospheric water budget within 3D grid cells. At the core of the analysis, there is the vertically integrated moisture budget:

$$\frac{\partial W}{\partial t} = ET - P - \nabla \overrightarrow{F} \tag{1.4}$$

where W is the water vapor integrated over the air column, ET is the evapotranspiration, P is the precipitation, $\overrightarrow{F}$ is the vertically integrated horizontal moisture flux, and $\nabla \overrightarrow{F}$ is its divergence. The mid-century approach used Equation 1.4 to evaluate the flux divergence to diagnose net source or sink regions [60, 63, 65]:

$$\nabla \overrightarrow{F} < 0 \rightarrow \text{convergence} \rightarrow \text{sink region}$$
$$\nabla \overrightarrow{F} > 0 \rightarrow \text{divergence} \rightarrow \text{source region}$$

Even though this approach could spot source and sink regions, it was not able to evaluate the transport history of moisture and thus could not link sources to sinks. This is why modern Eulerian models such as WAM-2Layers [73] and WRF-WVT [74], to overcome this limitation, adopted the moisture tagging approach (Figure 1.4): moisture evaporating from different regions is labeled with different tags (e.g. $q_{land}, q_{ocean}, q_{Amazon}$) which are carried along the transport. This method, firstly attempted in the late 1980s [88] and then fully incorporated in Eulerian models by Sodemann et al. (2009) and Winschall et al. (2014), allows the humidity within every grid cell to be decomposed in its different origins thanks to these tags. The moisture labeled with a specific tag, q_i, satisfies its own Equation 1.4. When precipitation occurs the model removes moisture from the grid cell proportionally from each tag. This implies that tagging allows for computing how much precipitation in any region originated from each evaporative source to be computed, providing source-sink information and maps but it can not reconstruct physical transport. It is important to note that Eulerian moisture tracking models can operate either *online* (e.g. WRF-WVT [74]), where the tracking process is integrated within the atmospheric model during the simulation, or *offline* (e.g. WAM-2Layers [73]), where moisture sources and pathways are diagnosed afterwards using stored meteorological fields.

Lagrangian Models There are two main processes that build up a complete Lagrangian moisture tracking model: trajectory definition and diagnosis of source and sink areas. There are models such as Utrack [90] and BTrlMS [91] that include both processes, while there are others that rely on two models working in pairs: a model defines the trajectory, and another diagnoses the source areas. Models for calculating trajectories include FLEXTRA [66], FLEXPART [67], and LAGRANTO [72] while examples of diagnostic models are WaterSip [69], and SJ04 [92].

Regardless of the asset, Lagrangian models are models that work *offline*, meaning that the trajectory and source diagnosis are computed after or separately from the main simulation. On a practical level, this means that the main atmospheric model, like reanalysis (e.g. ERA5 [93]) or GCM, has already been run, producing output fields (e.g. winds, temperature, humidity, pressure, precipitation) that the moisture tracking model then uses. In fact, the moisture tracking model reads these outputs and performs calculations to obtain trajectories, moisture sources, flux divergence, and recycling ratios. This *offline* functioning implies that there is no feedback process

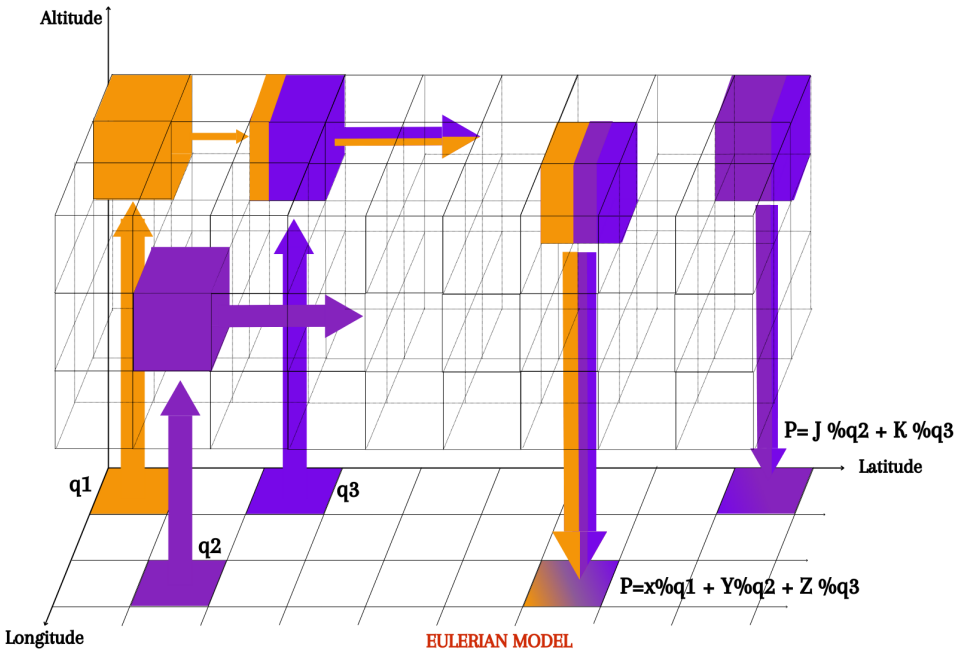

Fig. 1.4. Graphical representation of the functioning of an Eulerian moisture tracking model. Moisture is tagged according to the relative evaporation source (q1, q2, q3). Precipitation P is composed of water with the same percentage (J, K, X, Y, Z) tag-composition of the moisture contained in the grid cell.

and thus the offline computation cannot modify winds, humidity, or any part of the atmospheric model simulation.

The trajectory computation consists of defining the path that an air parcel follows through the atmosphere from the source cell to the sink cell. In Figure 1.5 this process is represented by the red-line pathway while sources and sinks are represented in green and blue, respectively. The computation of the trajectory implies interpolating wind fields $\overrightarrow{v}(\overrightarrow{x},t)$ between cells and in time and updating for every timestep the 3D position vector $\overrightarrow{x}(x(t),y(t),z(t))$ of the air parcel. The relationship between $\overrightarrow{v}$ and $\overrightarrow{x}$ is defined as:

$$\frac{d\overrightarrow{x}}{dt} = \overrightarrow{v}(\overrightarrow{x},t) \tag{1.5}$$

Generally, x represents the east-west location usually expressed in longitude coordinates, y the north-south location expressed as latitude, while z stands for the height expressed as pressure level or altitude. Simple kinematic trajectory models often neglect turbulent motion, whereas Lagrangian particle dispersion models such

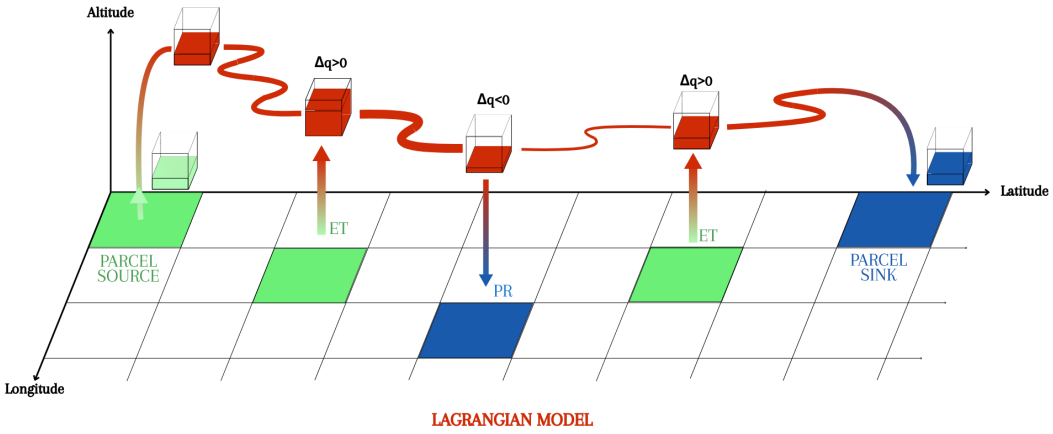

Fig. 1.5. Graphical representation of a Lagrangian moisture tracking model functioning with the "specific humidity changes" method. In red, the trajectory derived by wind fields, in green and blue, evapotranspiration input and precipitation outputs, respectively. The thickness of the red lines represents the water content (specific humidity) within the parcel.

as FLEXPART explicitly parameterize turbulent transport. This implies that an additional factor accounting for turbulence displacement is required:

$$\vec{x}_{t+\Delta t} = \vec{x}_t + \vec{v}\Delta t + \Delta\vec{x}_{turb} \tag{1.6}$$

where $\vec{v}\Delta t$ represents the large-scale wind advection and $\Delta\vec{x}_{turb}$ represents the turbulence corrections. Turbulence is an important factor in real air motion. In fact, while large-scale winds mainly carry moisture over large distances as the resolution of the atmospheric models is too coarse to catch turbulence phenomena, the turbulence correction allows for including subgrid-scale processes including convection turbulent mixing, cloud microphysics and downdrafts. Generally, horizontal turbulence results in small adjustments of moisture between neighboring cells as, in the boundary layer, it is much weaker than the vertical turbulence (usually at least an order of magnitude), and above the boundary layer it is negligible with respect to horizontal winds magnitudes. Vertical turbulence, instead, is crucial for more realistic trajectory assessments as it lifts and drops parcels rapidly and redistributes parcels within the clouds.

While air parcel-tracking models, FLEXPART, require an explicit simulation of turbulence motion because air parcels trajectories are governed by small-scale processes, UTrack, which tracks moisture parcels, adopts a simplified stochastic representation. The main difference between tracking air parcels or moisture parcels stands in the fact that, while air parcels are physical volumes of air containing dry air, water vapor, temperature, momentum, and pressure, that follow the dynamical equations of motion of the real atmosphere, moisture parcels only represent the (discrete) amount of water vapor mass. Moisture parcels do not carry temperature, density, or stability information. In this framework, the large-scale transport of moisture parcels is governed by the three-dimensional wind field provided by ERA5, while subgrid-scale mixing processes due to turbulence are partly represented through stochastic dispersion and partly inherited from the atmospheric physics embedded in the reanalysis fields.

Trajectories can be computed forward or backward in time. The algorithm depends on the same principles but the purpose varies: with the forward trajectory the parcel is traced from the emission source to the final sink and, thus, providing information on the downwind area where it contributes to precipitation; on the contrary, the backward trajectory starts at the precipitation sink cell and it is traces back to where it originally evaporated from, gaining information on the upwind basin providing moisture to the sink cell. Generally, moisture-tracking methods provide a powerful tool to explore atmospheric moisture transport, but suffer from limitations arising from imperfect reanalysis forcings and representation of sub-grid processes such as cloud microphysics and turbulence. Forward tracking is a good tool for analyzing moisture export and atmospheric connectivity but it has to be kept in mind that it might be complicated to match exact precipitation events because not all moisture can precipitate in a traceable way and particles can have an atmospheric lifetime longer than the one imposed in models. In fact, atmospheric moisture, even though it has mean maximum residence time of 5-10 days [94], it can persist in the atmosphere from a few hours, in case of convection, up to several months in the upper troposphere [73, 94, 95]. This means that forward tracing may underestimate actual contribution to precipitation. Furthermore, strong uncertainty in the attribution to specific sinks can arise from the divergence of trajectories in the free troposphere [96] and from the fact that parcels may lose moisture along the way and not at the moment and location of a precipitation formation due to cloud microphysics, detrainment and subgrid precipitation processes [68]. Since parcels disperse and mix across the domain it is

difficult to determine with confidence whether a given evaporation event contributed to a particular precipitation event and this is why, for source attribution, backward tracking is preferred. Backwards trajectories work very well to identify the source of precise strong events such as storm and floods but it has to be kept in mind that they are sensitive to turbulence parametrization and thus are numerically less stable: small errors in wind fields grow exponentially backwards and uncertainty increases strongly after 2-3 days [96, 97]. Finally, it is important to remember that backward tracking cannot handle multiple merges of humidity streams nor moisture that was lost but re-evaporated and rejoined the parcel, as may occur in convective processes.

At the end of the trajectory algorithm the available information is where the parcel traveled, not why or how its moisture changed. Thus, after the trajectories are computed, the diagnostic step determines where moisture was gained and lost along the path to identify sources and sinks. To do so, two main methods are generally applied [98]: the "well-mixed column" method, and the "specific humidity changes" method. While the first method, presented by Dirmeyer and Brubaker in 1999, is applied in UTrack and BTrlMS models, the second, introduced Sodemann et al. in 2008, is applied in WaterSip. The "well-mixed column" method assumes that surface moisture fluxes, such as evapotranspiration (ET) and precipitation (P), affect the entire atmospheric column: an injection of moisture through ET is instantaneously redistributed among all air parcels across the vertical layers of the column; analogously, when precipitation occurs, the moisture loss is proportionally removed from all parcels p within the column. As a result, the moisture content of each parcel, m_p, increases (or decreases) according to the ratio between the injected (or precipitated) moisture and the total amount of water present in the column at that time step:

$$\begin{aligned} m_p(t) &= m_p(t-1) + r m_p(t-1) \\ r &= \frac{ET}{\sum_{p=1}^{n} m_p(t-1)} \end{aligned} \tag{1.7}$$

This implies that, along a trajectory, each parcel is associated with a specific source or sink according to its moisture content rather than its position within the air column. The "specific humidity changes" method, instead, is based on the individual evaluation of changes in specific humidity q of each parcel p:

$$\frac{dq_p}{dt} = ET - P + h \tag{1.8}$$

where ET is evapotranspiration fluxes, P is precipitation, and h any microphysical-related phenomena such as cloud-phase change. While in Eulerian models the convergence/divergence term, $\nabla \overrightarrow{F}$, is present (Equation 1.4), in Lagrangian models it is not; this because the advection can not be seen as the reference system moves with the parcel. Thus, changes in humidity reflect actual moisture gain and losses due to the interaction with evaporative sources or precipitation events. However, to determine whether an uptake or loss occurs, WaterSip imposes the additional criteria that the variation has to exceed $\Delta q = 0.05$g/Kg and that it has to occur within the Planetary Boundary Layer (PBL). Thus, moisture sources and sinks are inferred from the variations in specific humidity in the parcel:

$$\begin{cases} \frac{dq}{dt} > 0.05 \rightarrow \textit{moisture source} \\ \frac{dq}{dt} < -0.05 \rightarrow \textit{moisture sink} \end{cases} \tag{1.9}$$

In Figure 1.5 this process is represented by the increase or decrease of q and the specific definition of source cells (in green) and sink cells (in blue). Wherever these variations in q occur, the model records location, time and amount of water gained or lost in order to be able to define source and sink maps. It is important to note that rises in humidity occurring in the free troposphere that can not be attributed to shallow or deep convection are not linked to surface evaporation as these injections only occur in the boundary layer. These increases can be attributed only to detrainment or horizontal convergence and can not be linked to a source location [95]. For either method, it is important to note that because a single parcel represents only part of the moisture precipitating on a target sink cell, Lagrangian diagnosis for a specific target cell requires integrating the trajectories and the specific sources over many parcels. Likewise for a target source cell.

The choice between Lagrangian and Eulerian moisture tracking approaches depends on the scientific objective. Lagrangian models are particularly suitable for identifying moisture source regions and reconstructing atmospheric transport pathways, as they explicitly follow parcels along their trajectories. This makes them especially useful for analyzing extreme precipitation events and air mass histories. Within the Lagrangian framework, different implementations exist. Integrated models such as

UTrack directly track moisture parcels and are particularly suited for large-scale analyses of evaporation–precipitation linkages and continental moisture recycling [90]. Other approaches, such as the combination of trajectory models (e.g. FLEXPART) diagnostic models (e.g. WaterSip), allow a detailed representation of atmospheric transport and turbulent dispersion and are therefore well suited for studies focusing on the origin of specific precipitation events or for reconstructing the pathways of individual air masses [100]. Eulerian approaches, by contrast, diagnose moisture transport from atmospheric water budgets within fixed grid cells and are therefore better suited for large-scale climatological analyses of moisture recycling and regional water budgets. For this reason, Lagrangian and Eulerian approaches are often considered complementary, as they provide different perspectives on atmospheric moisture transport.

Chapter 2

Evaluating country-scale irrigation demand through parsimonious agro-hydrological modelling

The following Section is strongly related to the work presented by Chiesa Turiano, N.; Tuninetti, M.; Laio, F.; Ridolfi, L. in Evaluating Country-Scale Irrigation Demand Through Parsimonious Agro-Hydrological Modeling. (Hydrology 2025, 12, 240)

Water governance operates at multiple levels, from international organizations down to local consortia [101]. This multi-level approach is essential to guarantee that water policies and laws ensure both (water-dependent) food and energy security without undermining environmental protection [102, 103]. In fact, nowadays, 40% of the world's food production comes from irrigated land which, despite accounting for only 18% of the global cultivated land [104], accounts for from 60% [5] to 70% of total freshwater withdrawals [3, 4]. This pressure on freshwater bodies is expected to increase significantly mainly due to the world population growth [105], dietary changes towards more water-demanding food choices [106, 107], and the need to buffer the increased vulnerability of cultivated lands to climate extremes [108]. Furthermore, future alterations of the hydrological cycle due to climate change [109–112] will likely impact the natural availability of freshwater resources, making effective water governance even more crucial [113]. This highlights the need for effective local water management even in water-rich areas where water exploitation has often been overlooked [114].

Under these conditions, there is an ongoing effort to improve national agricultural water management to reduce both the agriculture's vulnerability to climatic variability and the stress on freshwater bodies and the associated ecosystem [115–117]. Effective national water management has, in fact, the potential to regulate local water withdrawals from water bodies, preventing the regional excessive use of irrigation water and reducing crop losses due to water stress [118, 119].

To this aim, accurately evaluating irrigation demands, along with other water uses, is essential for right water management and allocation [120]. Comprehensive national-scale evaluations of agricultural water use can provide pictures of the current water consumption across different regions. This helps identifying areas where structural and management improvements are needed, thus supporting decision making. Furthermore, reliable models can simulate various potential scenarios and predict the impact of different water management practices, providing valuable insights for investments and action plans.

In this context, agro-hydrological models are powerful decision-support tools for evaluating agricultural water requirements at various scales [114, 121–124]. Numerous models have been developed over the years to this purpose (e.g. AquaCrop [125], SWAP [126], DSSAT [127], CropWat [128], APSIM [129], CropSyst [130]), encompassing a wide range of modelling approaches, accuracy levels, and flexibility [131, 132]. However, the use of most of these models is constrained by their data requirements and the spatial scales at which they can be applied. In fact, on one hand, highly complex models offer great accuracy and physical detail but are typically field-specific, computationally demanding, and require detailed input data that is often difficult to obtain [133]. It follows that these models are applied at the field scale, but are hardly upscalable at regional and national scales.

On the other hand, simpler large-scale models are adopted for simulations at continental and global scales [134, 135]. They require much less information than the previous class of models but may be too crude for agricultural water planning and management at the regional scale [136]: They often fail to account for variations in irrigation practices or soil diversity at the municipal scale, operate on a daily time scale, and approximate the modelling of the soil water balance.

In this framework, our aim is to propose a physically-based, agro-hydrological model that balances the complexity of detailed field-scale models with the lower data demand of large-scale models (for a description of these models refer to Section

1.2.3). Our model describes all the main hydrological processes that determine agricultural water demand but, at the same time, requires data typically available at municipal resolution rather than using coarse spatial resolution as typically done on regional and global models. By providing both quantitative outputs and spatially explicit maps, the model proves suitable for regional-scale water resource planning and management. Its accessibility and simplicity make the model usable by both specialists and non-experts, enabling process tracking, parameter adjustment, and critical evaluation of results.

The model WaterCROPv2 proposed here builds upon model WaterCROPv1 [137], introduced in 2015, enhancing it in several aspects by incorporating new hydrological processes and refining existing ones. Although the model presented in Tuninetti et al. was not originally named, it set the foundation for the present model. In agreement with its original developer, we refer to it here as WaterCROPv1.

To show the potential of the proposed model, we will (i) describe the physical processes considered and their modelling, (ii) show the typical WaterCROPv2 output, highlighting the advantages obtained with the updates in the crop water demand assessment, (iii) focus on the irrigated maize cultivation in Italy as an exemplifying case study. The case study allows us not only to show WaterCROPv2 reliability in assessing irrigation water demand but also to shed light on how the model can be used to analyse scenarios aimed at saving irrigation water and reducing the stress on freshwater resources.

2.1 Materials and Methods

2.1.1 Model

WaterCROPv2 is an agro-hydrological bucket model that simulates the crop and irrigation water demand during the growing season depending on soil, climate, crop, and irrigation system features. The bucket, as in large-scale models, is designed as a single soil layer to reduce the input data but, as field-scale models, its depth increases during the plant growth according to the length of the plant roots Zn. The bucket not only stores water but also receives and releases hourly volumes of water. The fluxes entering the storage are (see Figure 2.1) the effective precipitation (P_{eff}) and the crop blue water demand (I_b), while the exiting ones are the leakage (L) and

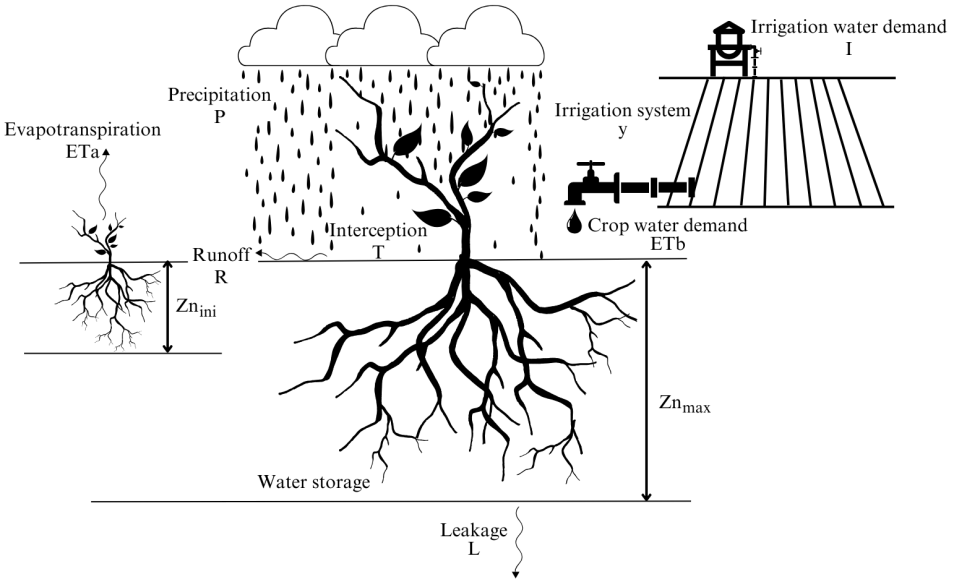

Fig. 2.1. Water balance components of the bucket model: precipitation P, interception T, runoff R, evapotranspiration ET_a, crop water demand I_b, and leakage L. Zn_{ini}, Zn_{max}, y stand for initial roots'depth, maximum roots' depth, and irrigation system respectively.

the actual evapotranspiration (ET_a) also known as crop water demand. P_{eff} is the precipitation P decreased firstly of the volumes of drizzle water intercepted by the canopy, T, and secondly of the runoff R.

The mentioned inputs and output fluxes entail the temporal fluctuations in the water stored in the soil, namely the so-called soil water content, WC. The water balance equation for the soil layer reads

$$\frac{\mathrm{d}WC(t)}{\mathrm{d}t} = P(t) - T(P(t)) - R(WC(t)) - ET_a(WC(t)) - L(WC(t)) + I_b(WC(t)) \tag{2.1}$$

where the soil water content is expressed in mm, time t in hours, and fluxes in mm/hour. It is important to note that, as will be further described later on, R, ET_a, T, L, and I_b are functions of the soil water content. WC can span from $WC = 0$ mm to the soil water content at saturation WC_{sat}, whose magnitude depends on the soil type and the roots length Zn. Specific WC values play a crucial role in regulating the input/output fluxes (Figure 2.2):

- WC_{wp}. It is the WC at wilting point and sets the minimum water content for plants to survive;
- WC_{*}. It is the WC at critical condition and it is the threshold that controls whether evapotranspiration is at maximum and whether it is necessary to resort to irrigation;
- WC_{fc}. It is the WC at field capacity and when WC goes below WC_{fc} the leakage process ends;
- WC_{sat}. It is the WC at saturation, which controls the surface runoff formation.

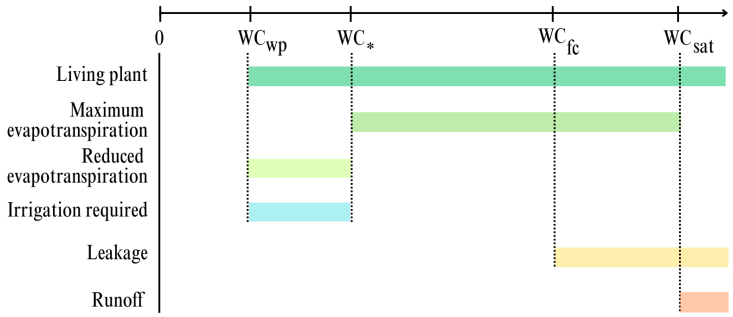

Fig. 2.2. Ranges of possible water content (WC) values for different processes. Note that the light-blue bar of irrigation requirements shows the case of irrigation up to the critical level (WC_{*}).

The previously defined WC thresholds are not fixed values but are proportional to the length of the plant roots, Zn, that elongate during the growing season: the further the roots grow into humid soil, the larger becomes the amount of water (corresponding to the thresholds) contained in the control volume.

The growing period is subdivided into four growing stages, namely initial phase (establishment, lgp_1), development stage (vegetative, lgp_2), mid-season (flowering, lgp_3), and late season (yield formation and ripening, lgp_4). Taking Zn_{ini} as initial roots length, Zn_{max} as maximum length, and d as the day along the growing period, Zn is computed as [128]

$$Zn_t = \begin{cases} Zn_{ini} & \text{if } d = 1 \\ Zn_{ini} + \frac{Zn_{max} - Zn_{ini}}{lgp_1 + lgp_2} d & \text{if } d \in [lgp_1, lgp_2] \\ Zn_{max} & \text{if } d \in [lgp_3, lgp_4] \end{cases} \tag{2.2}$$

Zn is assumed to always be in the vadose zone. It follows that there is no interaction between root zone and the water table. For a visualization of the elongation trend of Zn during the growing period, refer to Figure 2.4.

WaterCROPv2 is designed so that the continuous description of the water balance (Equation 2.1) in time t is discretized in hours that, every day, run from h=1 to h=24. This discretization implies that ET_a, L and P, which naturally occur during or throughout the whole day, are here hourly discretized. Every day, at the first hour, ($h = 1$ of the day d), the bucket stores the same volume of water as the last hour of the previous day, ($h = 24$ of day $d - 1$), plus I_b, computed as the amount of water needed to reach the chosen water content, i.e. $WC_d(h = 1) = WC_{d-1}(h = 24) + ET_{b,d-1}$.

Evapotranspiration. ET_a takes into account plant transpiration and water evaporation from the soil. Each hour h along the growing period, ET_a is evaluated as

$$ET_a(h,d) = \begin{cases} ET_0(h,d) k_c(d) k_s(h) & \text{if } P(h) = 0 \\ 0 & \text{if } P(h) > 0 \end{cases} \tag{2.3}$$

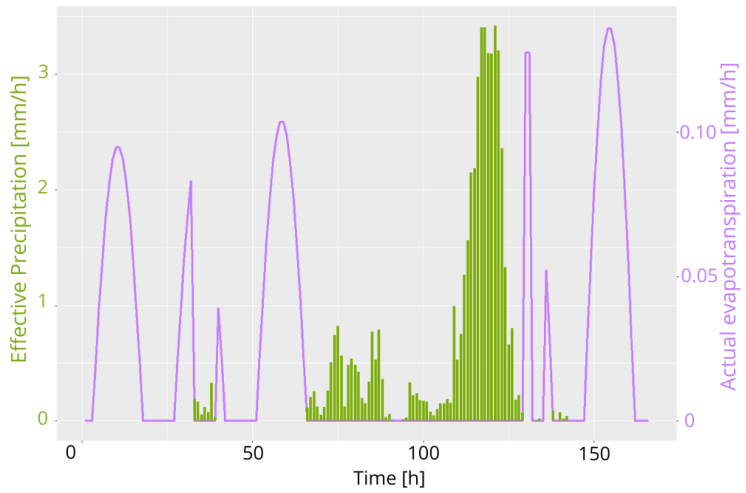

Fig. 2.3. It is here reported the case of two rain events that stop the daily evapotranspiration process. The evapotranspiration behavior is shown for 6 days (from 28^{th} to 35^{th} day) in May of the initial stage of maize growth ($k_c \in$ [0.3-0.4125]) during which the plant is not under stress (k_s=1).

where ET_0 is the reference evapotranspiration, k_c is the crop coefficient, and k_s is the water stress coefficient. As ET_a rate is strongly driven by the gradient in relative humidity, Δe, between stomata and atmosphere, in case of rain events ($\Delta e \simeq 0$), ET_a is assumed to shut down.

ET_0 is defined as the evapotranspiration of a hypothetical well-watered grass reference crop with fixed height, albedo, and surface resistance [128]. Databases usually provide daily ET_0 values in spite of transpiration being a diurnal process that shows a peak around mid-day. In order to account for daily plant physiology, in WaterCROPv2, ET_0 is modelled according to [138]:

$$\begin{cases} ET_0(h,d) = \frac{ET_{0,d}(d)\pi \sin(\frac{\pi H}{N})}{2N} \\ N = ss - sr \\ H = h - sr \end{cases} \tag{2.4}$$

where $ET_{0,d}(d)$ is the daily evapotranspiration value corresponding to the day d, N is the amount of hours spanning from sunrise sr to sunset ss, H is the time elapsed since sunrise. Sunrise and sunset timing were defined, cell by cell, according to location (latitude and longitude) and day of the year.

The crop coefficient, k_c, is the coefficient that distinguishes the evapotranspiration rate of a specific crop from the one of the reference grass. k_c varies during the growing season depending on the crop development in order to take into account changes of crop height and leaf areas.

In particular, k_c evolves in time as [128]

$$k_{c,t} = \begin{cases} k_{c,ini} & \text{if } d \in lgp_1 \\ \frac{k_{c,mid}-k_{c,ini}}{d-lgp_2} d & \text{if } d \in lgp_2 \\ k_{c,mid} & \text{if } d \in lgp_3 \\ \frac{k_{c,fin}-k_{c,mid}}{d-lgp_1-lgp_2-lgp_3} d & \text{if } d \in lgp_4 \end{cases} \tag{2.5}$$

where $k_{c,ini}$, $k_{c,mid}$, $k_{c,fin}$ are k_c at initial, mid, and final growing stages respectively, and d is the day along the growing period. Note that k_c values and lgps lengths depend on climate zone and crop [128].Figure 2.4 shows the trend of k_c during the growing season.

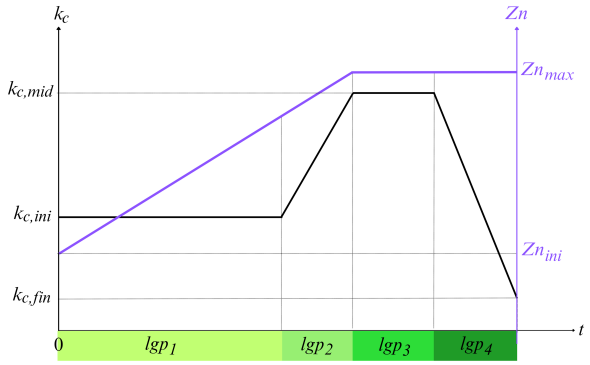

Fig. 2.4. Qualitative description of the crop coefficient k_c (in black) and the elongation of the roots Zn (in purple) during the growing stages lgps of the growing season.

The water stress coefficient, $k_s \in [0,1]$ is the coefficient that specifies whether the plant is watered enough to evapotranspire at its potential. Thus, it is regulated by

WC as [128]

$$k_s(h) = \begin{cases} 0 & \text{if } WC \leq WC_{wp} \\ \frac{WC(h)-WC_{wp}}{WC_*-WC_{wp}} & \text{if } WC \in [WC_{wp}, WC_*] \\ 1 & \text{if } WC \geq WC_* \end{cases} \tag{2.6}$$

Figure 2.5 shows k_s trend as function of WC.

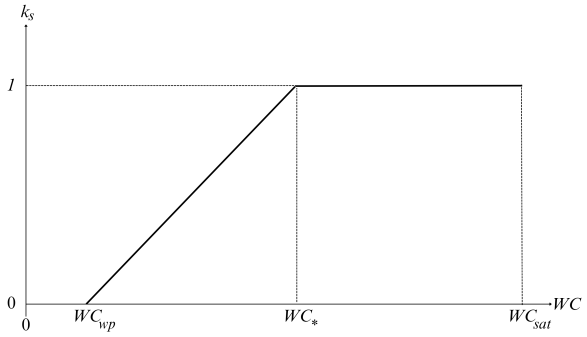

Fig. 2.5. Qualitative description of the crop coefficient, k_s, according to the soil water content.

If soil water content is above the critical value, WC_*, the plant is in stress-free conditions and it evapotranspires at its maximum potential, $ET_a = ET_c$. Instead, whenever the water content is below the critical value the plant is under stress and the evapotranspiration is lower than the potential one, $ET_a < ET_c$. This linear reduction is due to a gradual closure of the stomata that results in a progressive diminution in water uptake. If wilting point is reached, $WC = WC_{wp}$, water uptake stops and evapotranspiration ceases, $ET_a = 0$. Physical evaporation can take place below wilting point, independently from plant transpiration. However, this phenomenon is not modeled here as this study focuses on irrigated crops that unlikely reach such conditions. Figure 2.3 reports an example of ET_a evolution (purple line): the last hump shows the undisturbed daily trend, while the previous humps point out the effect of rain (green bins). Rain events cause the interruption of daily ET_a but if the rain-water has time to evaporate from the leaves, ET_a kicks in again (second hump).

Leakage. Leakage is modelled with the following exponential law [139]

$$L(s) = \begin{cases} \frac{K_s}{e^{\beta(1-s_{fc})}-1}[e^{\beta(s-s_{fc})}-1] & \text{if } s_{fc} < s \leq 1 \\ 0 & \text{if } s < s_{fc} \end{cases} \tag{2.7}$$

where K_s is the saturated hydraulic conductivity, β a soil-dependent coefficient, s the relative soil moisture defined as $s = WC/WC_{sat}$, and s_{fc} the relative soil moisture at field capacity. Coherently with the time discretization of water balance (Equation 2.1), L is evaluated with hourly steps.

Precipitation, interception, and runoff. To avoid very small precipitation values that do not affect the soil hydrological balance but, instead, can introduce spurious noise in the system dynamics, a filter was introduced: a rainfall is considered a rain event only if it accumulates at least 0.01 mm/h. Canopy interception, $T(h)$, is included by subtracting, from each rain event, 0.5 mm for grasses and 2 mm for trees [139]. Another key point is when rainfalls can be considered as two separate rain events. In this work, a reasonable break between two subsequent events was set at 5 hours.

Runoff, $R(h)$, is formed only if the effective precipitation, $P_{eff} = P(h) - T(h)$, brings in the control volume more water than the amount that can be stored. The overflowing water forms runoff as

$$\begin{cases} R(h) = P(h) - T(h) - WC_{av}(h) & \text{if } P_{eff} > WC_{av} \\ WC_{av}(h) = WC_{sat}(d) - WC(h) \end{cases} \tag{2.8}$$

Irrigation. WaterCROPv2 computes irrigation volumes I in two steps: first, it computes the crop blue water demand, I_b, and secondly the irrigation volumes I (called irrigation water demand). I_b corresponds to the theoretical amount of water needed to keep the soil at a chosen water content threshold, WC_{th}, taking into account soil dynamics (leakage) and plant physiology (evapotranspiration). Generally, WC_{th} is chosen so that the plant can evapotranspire at its potential: e.g. $WC_* < WC_{th} < WC_{FC}$. In WaterCROPv2 I_b is applied - conventionally at $h = 24$

(but other choices are easily implementable) - only if the soil water content is below the chosen water content, and only to reach such threshold. It follows:

$$I_b(d) = \frac{WC_{th}(d) - WC(h = 24)}{\Delta h} \tag{2.9}$$

Irrigation water demand I is the actual amount of water that the farmer has to provide to the field. Such value depends on the irrigation systems as it encloses the irrigation system inefficiency. There are several ways of defining the irrigation system inefficiency α according to the application [**?**]. In this work, we neglect the inefficiency of the conveyance system that transports water from the water body to the field, as we rather focus on the irrigation method present on the field (e.g. submersion, flow irrigation, sprinklers, micro-irrigation). Thus, in this work the irrigation inefficiency α ($\alpha > 1$) is defined, for each irrigation system, as the average ratio between the volumes of water provided to the field (I) and the one that has to infiltrate in the rootzone (I_b), namely

$$I(d) = \alpha I_b(d) \tag{2.10}$$

Flowchart. To aid the reader in grasping the logic of the model, the flowchart of the operations implemented by the model is reported in Figure 2.6.

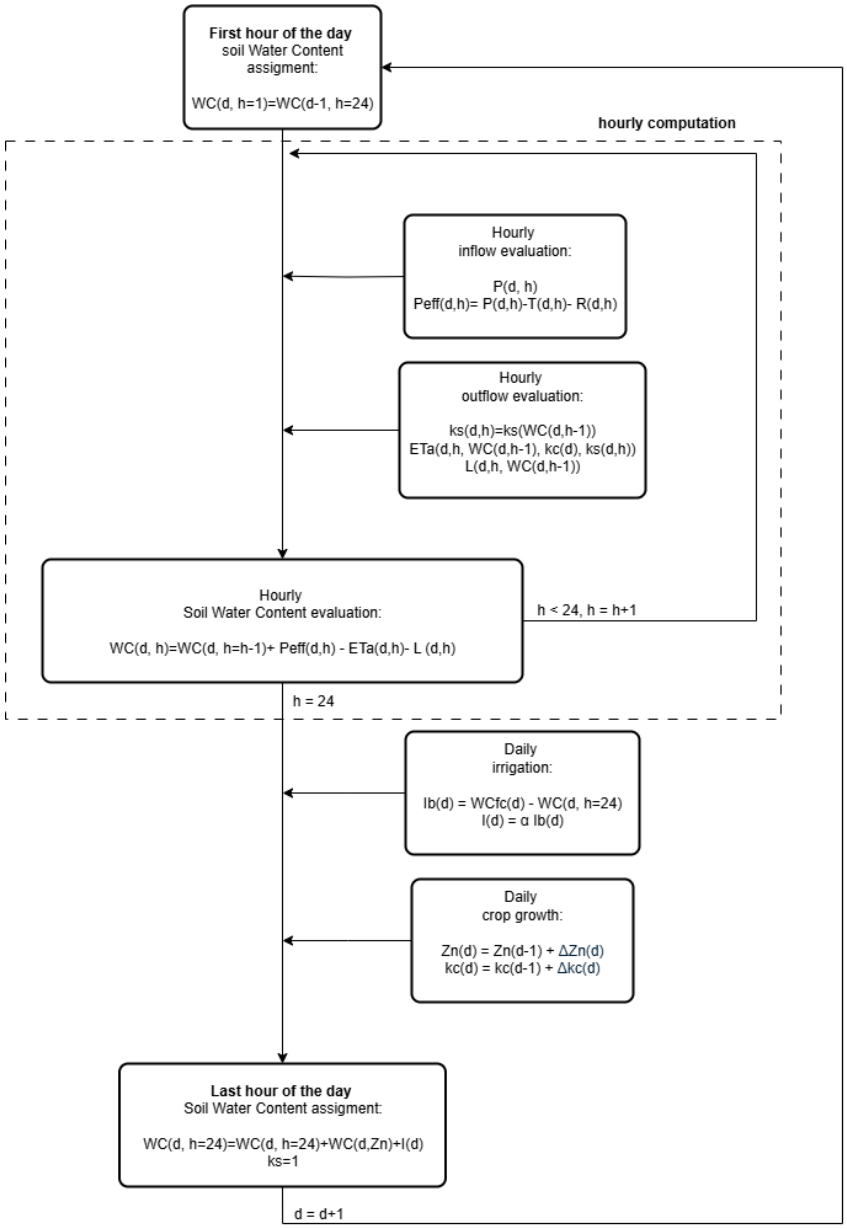

Fig. 2.6. Flowchart of the model functioning

Modifications of WaterCROPv2 with respect to version 1. Note that the improvements of water demand modelling of WaterCROPv2 with respect to WaterCROPv1 include: (i) the hourly timescale of the soil water balance, (ii) the use of hourly meteorological data instead of monthly precipitation, (iii) the inclusion the canopy interception of rainwater, (iv) the simulation of leakage dynamics in relation to soil water content and soil characteristics, (v) a detailed description of the diurnal trend

of evapotranspiration accounting also for location, day of the year and the presence or absence of rain, and (vi) the computation of I_b as the water that is required by the plant to be able to keep the field at a chosen water content. Finally, (vii) a key change is the introduction of the inefficiency factor of the irrigation system to take into account the additional water volume required to actually convey I_b to the plants.

2.1.2 Data

WaterCROPv2 works at hourly temporal resolution on grid cells whose size is determined by the input data resolution. All the required data must be homogenized at the same spatial and temporal resolution. The required input data fall into four categories: crop data, soil data, climate data, and irrigation data.

Crop data. Crop data characterize the crop in terms of growth and response to water stress. They are: (i) daily reference evapotranspiration (ET_0, d), (ii) crop-specific growth coefficients (kc_{ini}, kc_{mid}, kc_{fin}), (iii) length of the four growing period stages (lgp_1, lgp_2, lgp_3, lgp_4), (iv) critical soil moisture (WC_*), (v) initial and maximum roots depth (Zn_{ini}, Zn_{max}), (vi) sowing and harvesting dates, and (vii) extension of irrigated areas. Notice that sowing and harvesting dates, length of the growing stages, and root depth depend on cultural conditions and on the local climate zone.

It is noteworthy that, in literature, it is easier to retrieve values of critical depletion fraction, Dr_*, rather than WC_*. Dr_* is defined as the critical soil water shortage with respect to field capacity and it is related to WC_* as follows

$$Dr_* = WC_{fc} - WC_* \tag{2.11}$$

Soil data. The description of runoff and leakage processes requires: (i) saturated hydraulic conductivity (K_s), (ii) volumetric water content at field capacity (θ_{fc}), (iii) volumetric water content at saturation (θ_{sat}), and (iv) the fitting coefficient (β). Note that the volumetric water content θ is defined as the ratio of water volume WC to soil volume V_{soil} (e.g. $\theta_{fc} = WC_{fc}/V_{soil}$).

Climate data. Major players in plants phenology are local climate and precipitation. Thus, (i) climate zone, (ii) hourly precipitation time-series, and (iii) geographical coordinates have to be provided for the studied area.

Irrigation data. WaterCROPv2 determines the irrigation water demand, I, from the blue water demand, I_b (Equation 2.15). To do so the inefficiency factor α of the used irrigation systems has to be provided.

Case study: maize in Italy

To study the water demand of maize in Italy, accurate research was carried out among databases and literature data to build the best dataset combining availability, accuracy, handiness, and reliability (Table 2.1). According to the resolution of the selected datasets, the case study was run at 5x5 arc-min (pixel of $\sim$ 8x8 km^2 on average in Italy) cell spatial resolution for the year 2010. This reference year was selected due to data constraints: detailed information at the municipal scale was only provided by the 6th Agricultural Census carried out by the National Institute of Statistics, ISTAT [140], which refers to 2010.

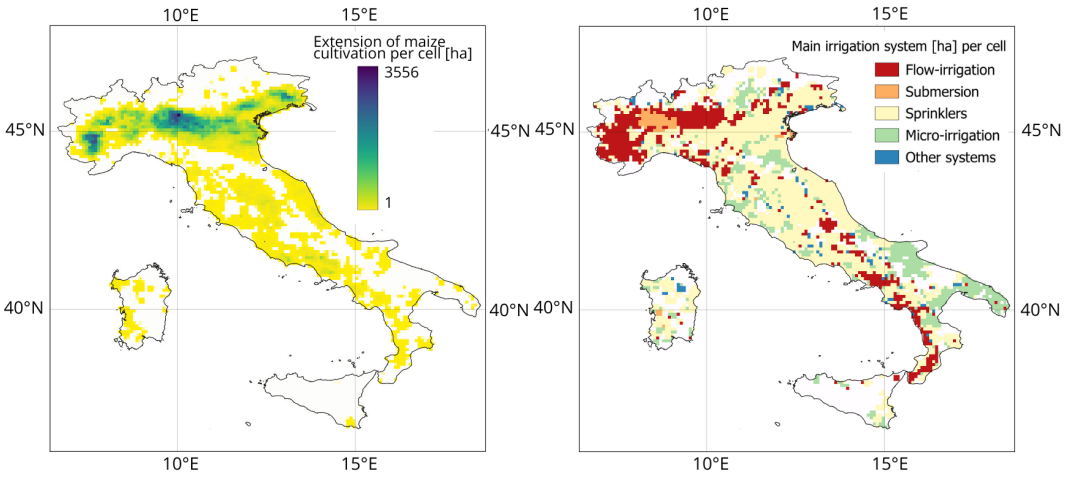

(a) (b)

Fig. 2.7. Maps of (a) the extension of maize cultivation in each cell, (b) the most extensively adopted irrigation system. Data refer to year 2010.

Crop data. The daily reference evapotranspiration values were defined as 1/30 of the monthly values provided in the CRU dataset [141]. Given the lack of localised

Table 2.1. Datasets adopted for the model application to maize in Italy. [1][141],[2][140], [3][142], [4][128], [5][143], [6][144], [7][?], [8], [9][93],[10][145].

Data type	Variable	Dataset	Temporal Resolution	Spatial Resolution
Crop	Potential evapotranspiration	CRU[1]	month	0.5°
	p fraction[3]	-	year	5 arc min
	$k_c, Dr, Zn_{ini}, Zn_{max}, d_s, d_h$	FAO-56[4]	-	-
Soil	Available water content	Harmonized World[5] Soil Database v1.2	year	5 arc min
	Pedologic characteristics[6]	-	-	-
	Soil type	LUCAS[7]	year	500 m
Climate	Climate zones	PAMDataset[8]	year	5 arc min
	Precipitation	ERA5[9]	hour	0.25°
Irrigation	Cultivated areas	CensimentoAgricoltura2010[2]	year	municipality
	Irrigated areas	CensimentoAgricoltura2010[2]	year	municipality
	Irrigation system	CensimentoAgricoltura2010[2]	year	municipality
	Irrigation system efficiency[10]	-	-	-
	Municipalities extensions	ConfiniAmministrativi2010[2]	year	municipality

characterisation of maize in terms of growth (k_c, Zn_{ini}, Z_{max}) and response to water stress (Dr_*), we referred to general values provided by [146] (Table 2.2).

Table 2.2. Crop parameters for maize [146]

$\mathbf{Zn}_{ini}$	$\mathbf{Zn}_{max}$	$\mathbf{Dr}_*$	$\mathbf{kc}_{ini}$	$\mathbf{kc}_{mid}$	$\mathbf{kc}_{end}$
0.3	1	0.55	0.3	1.2	0.5

Differently, the grid dataset of sowing and harvesting dates avaialble for cultivated areas in 2000 [147] allowed us to take into account the quite high climatic heterogeneity of the Italian territory. By employing a resampling process, we were able to define local sowing, d_S, and harvesting dates, d_H. Where cultivated areas existed in 2010 but not in 2000, and consequently lacked corresponding dates, we performed a linear spatial interpolation based on the nearest 24 neighboring cells. Through the evaluation of d_S and d_H, we defined lgp: the length of each g-th growing stage. The length of each stage varies according to the climate zone and was computed as a fraction, p, of the total growing period length [142] as

$$lgp_g = p_g \dot{(} d_S - d_H) \tag{2.12}$$

Soil data. To categorize the Italian soil in soil classes we relied on the 500 X 500 m resolution dataset LUCAS [**?**]. As this resolution is higher than 5 arc-min, an upscale was run. The type of soil attributed to the 5 arc-min cell was the most recurring one among the 500 X 500 m cells falling inside the larger cell. To obtain a consistent result, the behavior of the different classes of soil to leakage was compared. The aim was to check whether some classes could be merged into one and, thus, correctly assign a soil type to each 5 arc-min cell. The classes that showed similar trends have pedological differences that can be considered negligible for the aim of this study. Figure 2.8 shows the different behaviors of the eight soil classes. It is evident how the eight classes group into are four clusters. For the sake of simplicity, even though the sandy-loam class is a cluster on its own, it was associated with loamy sand as very few cells fell in this class, and the remaining classes were traced back to three classes: silt-clay-loam, loam, and loamy-sand.

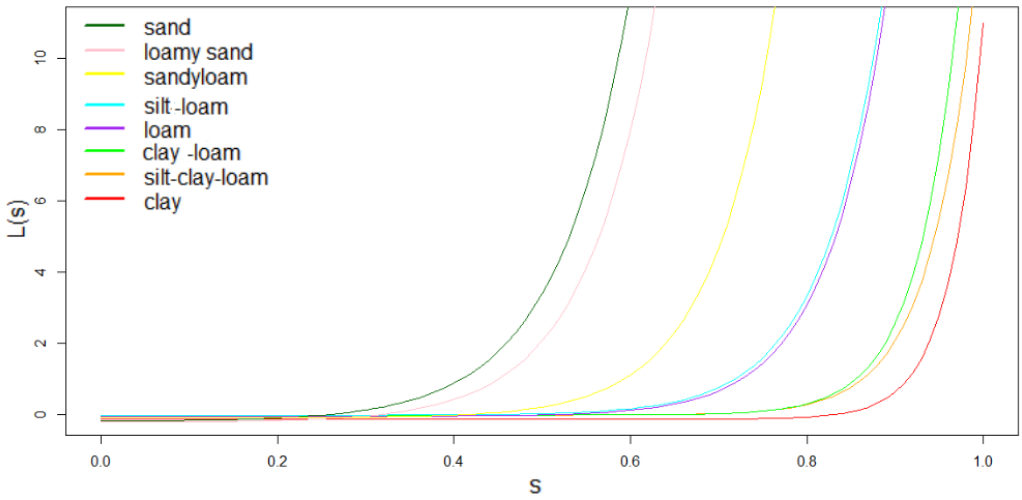

Fig. 2.8. Leakage L according to the type of soil as a function of s, the relative soil moisture: sand in black, loamy sand in pink, sandy loam in yellow, silt-loam in light blue, loam in purple, clay-loam in green, silt-clay-loam in orange, and clay in red.

Typical values of hydraulic soil characteristics, for each class, are reported in Table 2.3.

Table 2.3. Soil characteristics [144].

Soil Class	K_s **[mm/h]**	**b**	θ_{sat}	θ_{fc}
Silty-Clay-Loam	0,0612	7,75	0,477	0,275
Loam	0,2502	5,39	0,451	0,225
Loamy sand	5,628	4,38	0,401	0,125

Climate data. Local climate conditions were defined by the climate zones provided in the PAMDataset [143] and the hourly precipitation data were taken from the reanalysis ERA5 dataset [93]. Geographical coordinates correspond to the location of the centroid of each grid cell.

Irrigation data. Data on the extension of irrigated areas were available for 2010, only in listed form and by municipality thanks to the agriculture census ran by the National Institute of Statistics (ISTAT) [140]. To retrieve spatial information (with 5 arc-min resolution) on maize, the listed data were firstly combined with the spatial location of each municipality and, then, rasterized in grid cells (Figure 2.9). The

rasterization was necessary because more than one municipality fell within the same grid cell and each municipality fell within multiple grid cells.

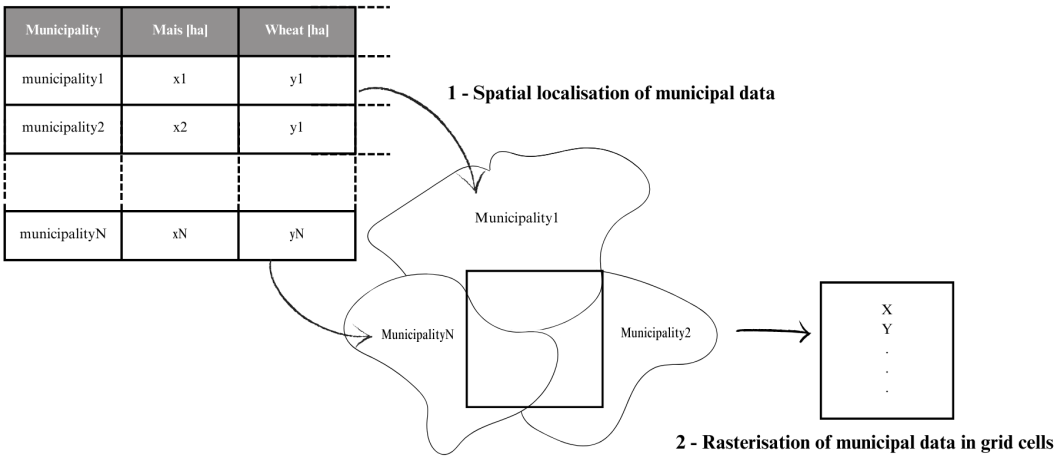

Fig. 2.9. Pre-processing steps to obtain the spatial distribution of irrigated areas. The first step requires to attribute to each municipality, spatially located across Italy, its value of irrigated areas. The second step rasterizes into grid cells the information according to Equation 2.13.

Lacking details at the sub-municipal scale, we assumed the maize irrigated area of each municipality ha_m to be homogeneously distributed within each municipality m. Hence, for each grid cell, c, the maize irrigated area ha_c [ha] was computed assuming that (i) the percentage of the municipality extension within the grid cell could be directly applied to the irrigated area, (ii) ha_c to be homogeneously distributed within the grid cell, and (iii) ha_c to be defined as the sum of the percentages of irrigated areas of the *m-tot* municipalities that fell within the grid cell. It follows:

$$ha_c = \sum_{m=1}^{m-tot} ha_m \frac{A_{m,c}}{A_m} \tag{2.13}$$

where ha_m stands for the maize irrigated area within the m-th municipality, A_m for the municipality area, $A_{m,c}$ for the municipality extent within the grid cell.

Unfortunately, the CensimentoAgricoltura2010 database provides, for each crop and municipality, data on the amount of irrigated hectares but not the specific irrigation system used for each crop. This did not allow us to define a local maize-specific value for the inefficiency factor α.

To overcome this gap, information about the typical irrigation systems used for maize in each cell was intersected with information on the available irrigation systems in each municipality. It was thus possible to define, for each cell, a plausible mix of used irrigation systems. Typically, in Italy, maize is irrigated with flow and lateral infiltration, sprinklers, and micro-irrigation systems and for their efficiencies we referred to data published by the Italian Ministry of Agriculture Food Sovereignty and Forestry [145] reported in table 2.4.

Hence, for each cell, c, the inefficiency factor α was computed as

$$\alpha_c = \sum_y \left(\frac{1}{\eta_y} \frac{ha_y}{ha_{tot}}\right) \tag{2.14}$$

where y stands for each irrigation system used in the cell, η_y for the corresponding efficiency, ha_y for the hectares irrigated with the irrigation system y, and ha_{tot} for the total amount of irrigated hectares within the cell.

2.2 Results

WaterCROPv2 was developed to evaluate in a reliable and functional way irrigation water demand at seasonal and regional scale. As an example case we here report and analyse the outputs of the employment of WaterCROPv2 at the Italian national scale. In Section 2.2.1, firstly, the mean maize irrigation demand for the years 2005-2015 obtained by WaterCROPv2 is compared to the evaluation obtained from the previous version WaterCROPv1 to show the effect of modelling improvements; secondly, the model reliability is assessed using independent data of irrigation water provided by the Italian national institute of statistics, ISTAT [140] for 2010. Lastly, Section 2.2.2 shows some possible applications of WaterCROPv2 model as decision-making tool using country-scale mean results for maize cultivation in Italy: maize is, in fact, one of the most water-demanding crops and, in Italy, it is so widely spread that alone accounts for more than 20% of the irrigated cropland [140].

2.2.1 Evaluation

Comparison with previous version WaterCROPv1

To analyze the impact of the updates introduced in version 2 both WaterCROPv1 and WaterCROPv2 were run with the same crop and irrigation data (Table 2.1).

The comparison was run analyzing the maize irrigation water demand (I_{mz}), defined as the cumulative sum of the daily volume required to keep the soil above a chosen water content, WC_{th}, over the growing period. In this case, WC_{th} was set to critical level WC_*. In Figure 2.10a, the scatterplot compares WaterCROPv1 and WaterCROPv2 cell by cell. The two versions display general consistency, as the points tend to align along the bisector. However, relevant differences due to the modelling improvements emerge clearly. In particular, it is visible how the relative importance of the newly added processes (leakage and the shutting down of the evapotranspiration process), and the use of hourly precipitation time series play a major role in the differences of the versions. In fact, the dots' distribution exhibits a smaller dispersion for higher irrigation water values, a condition corresponding to a reduced relevance of the added physical processes: high irrigation demands are due to low precipitations, that only rarely trigger leakage and evapotranspiration shutting down. On the contrary, v1 and v2 show weaker correlations for lower water demand values, which correspond to high precipitation levels, when leakage and shutting down play a relevant role. Finally, notice the significantly lower number of zero irrigation water demands according to the improved model. This result demonstrates the importance of describing precipitation on an hourly scale rather than distributing monthly values uniformly. This allows capturing periods of water shortage even in regions characterized by high mean monthly precipitation.

Comparison with independent data

In Figure 2.10b we tested WaterCROPv2 consistency with irrigation values provided by the Italian National Institute of Statistics, ISTAT [140]. In this case, I_{mz} values given by WaterCROPv2 correspond to the case of irrigation up to field capacity (WC_{th}=WC_{fc}), rather than to critical point: it is indeed of common practice, among the farmers, to irrigate up to field capacity. ISTAT values, instead, provided for each municipality, correspond to the output of the MARSALa model [148]: a

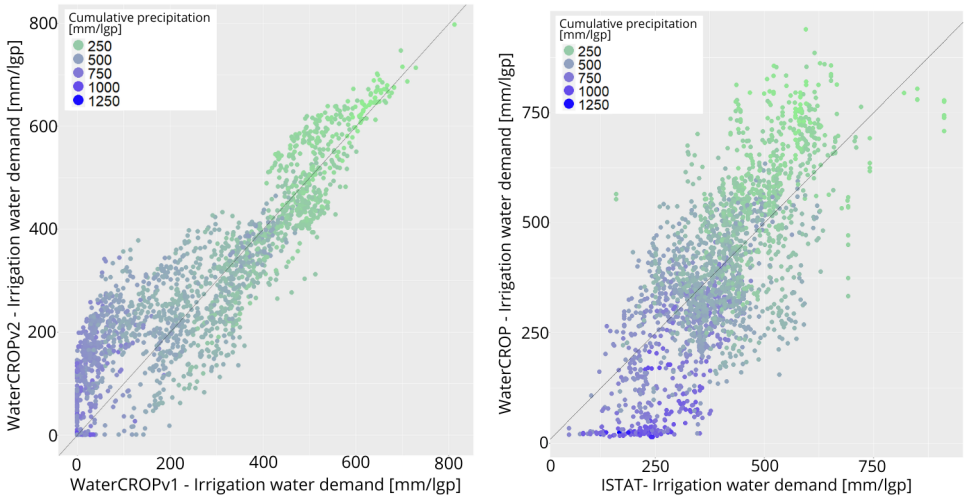

(a) (b)

Fig. 2.10. Scatter plots comparing, cell by cell, the irrigation water demand, [mm], of maize during the 2010 growing period, [lgp], in Italy computed by (a) WaterCROPv2 and WaterCROPv1 and (b) WaterCROPv2 and ISTAT database. The black line corresponds to the bisector. The color of the dots varies gradually from green (scarce precipitation) to blue (abundant precipitation) according to the values of cumulative precipitation over the growing season in the cell.

model calibrated over 300 farms assumed to be representative of Italian agriculture. MARSALa is a more detailed and computationally demanding model with respect to WaterCROPv2 as it includes a section of irrigation method scheduling that requires additional input data. Furthermore, the model relayed on farm-level input data on sowing and harvesting dates, as well as on locally employed irrigation systems: none of which available in the "Agricultural Census" [140] database used to run WaterCROPv2. Due to the robustness of the source of the input data used to run MARSALa, we assume the output values as the benchmark for the evaluation of WaterCROPv2 reliability. Due to the different complexity of the irrigation models and the accuracy of input data, WaterCROPv2 values are not expected to precisely match ISTAT values but rather to exhibit a similar trend. Figure 2.10b confirms this expectation as dots align along the bisector. The observed relation between estimation errors and precipitation suggests a spatial distribution of the differences, which is confirmed in Figure 2.12a-2.12b. Northern Italy, generally wetter (most of blue dots in Figure 2.10b, shows a mean underestimation of 23% while, on the contrary, Southern Italy, generally drier (generally green dots in 2.10b), experiences a mean overestimation of 14%. Central Italy, with locally variable differences, shows

a more consistent mean and distribution with a mean underestimation of 2%. The overestimation of WaterCROP2 can find a possible explanation in the fact that, especially in dry areas, it might be hard for the farmers to always irrigate up to field capacity meeting the model assumption. Lastly, note the dots in the bottom left of Figure 2.10b, where WaterCROPv2 and ISTAT dataset show strong disagreement: they correspond to cells with high precipitation, mainly clustered in two specific pre-alpine areas in the North-West and North-East of the Italy. The real ground slope in those areas might explain the disagreement. In fact, runoff in sloped fields is generally larger than the one for flat areas: as WaterCROPv2 does not include a terrain model, the underestimation of the runoff in those areas, and the consequent infiltration overestimation, might result in smaller I_{mz} values.

Comparison with previous local-scale studies

Mean maize irrigation water demand estimated with WaterCROPv2 was evaluated against values reported in field or local scale studies. For instance, Katerji et al. (2013) assessed maize irrigation demand in southern Italy (Rutigliano) for the 1996–1997 growing seasons using the AquaCrop model on a private farm. Bocchiola et al. (2013) investigated irrigation requirements in the Po Plain (Persico Domico) between 2001 and 2010 using CropSyst. Casa et al. (2009) applied remote sensing data combined with the FAO method [128] to evaluate mean irrigation needs in the Pontina Plain in the 1996–2001 period. Similarly, Todisco and Vergni (2008) analyzed average maize water requirements in several locations in Umbria (central Italy) over 1951–2004 period using CropSyst. In Figure 2.11, the comparison between the values reported in the above-mentioned studies (I-comp) and those obtained with WaterCROPv2 (I-WC) is presented. In the insets, the black-outlined rectangles mark the WaterCROPv2 pixels that overlap with the areas analyzed in the previous studies, with the corresponding I_{mz} values shown directly within the pixels. The I-WC value shown next to each inset represents the average of the pixel-scale I_{mz} values. All the comparisons considered highlight the good performance of our model, despite the smaller number of parameters used and the national scale of our analysis. Only the case of the Persico Domico area (see panel 2.11a) shows a significant difference: 120 mm/lgp estimated by WaterCROPv2 versus about 200 mm/lgp reported in [150]. However, it should be noted that the I-comp value refers to a single farm (shown in red in the panel), whereas the WaterCROPv2 estimate integrates contributions from

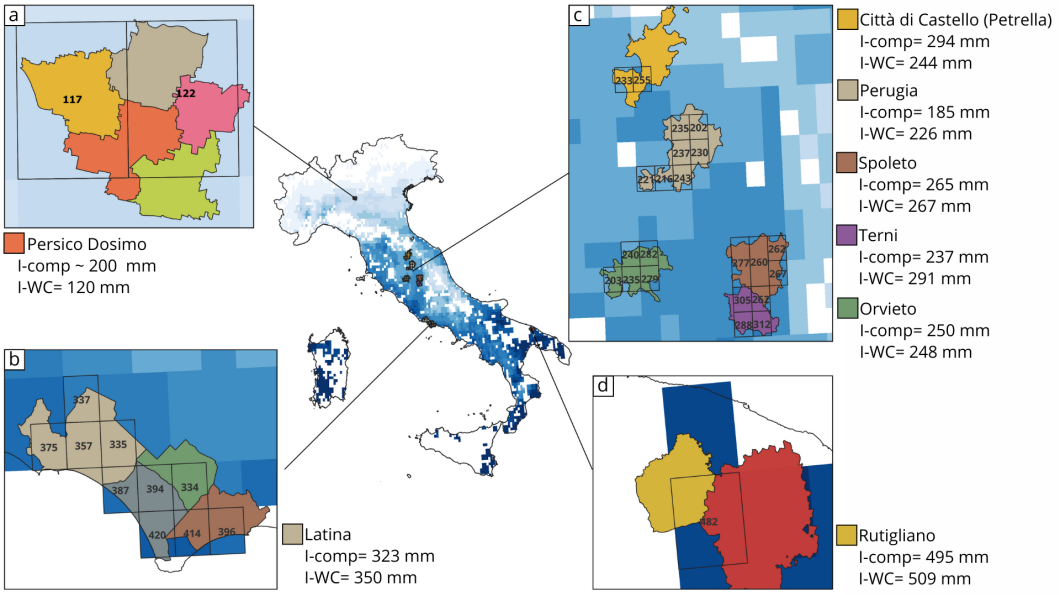

Fig. 2.11. Comparisons between irrigation requirements estimated at the national scale with WaterCROPv2 (I-WC) and irrigation requirements evaluated in previous studies at field or local scale (I-comp).

several municipalities and fields. Finally, in panel 2.11b all areas falling within the Pontine Plain are colored, but the crop distribution reported by Casa et al. (2009) shows that corn is mainly located in the municipality of Latina (shown in light brown in the panel). For this reason, the numerical comparison with our model refers to this specific area.

2.2.2 Examples of model application

Water demand assessment

In this section, we present some possible applications of WaterCROPv2 as a tool to evaluate the irrigation water demand both in current state and scenarios of interest.

We used WaterCROPv2 to assess the mean present state of maize irrigation water demand (I_{mz}) in Italy. To do so, we forced the model with crop, soil, climate and irrigation data as specified in Section 2.1.2 and assumed an irrigation threshold up to critical level (WC_{th}=WC_*). The used precipitation record covers the period from 2005 to 2015 as this timespan is considered representative of the Italian climate. In fact, Italy in those years experienced fairly large oscillations in cumulative precipitation

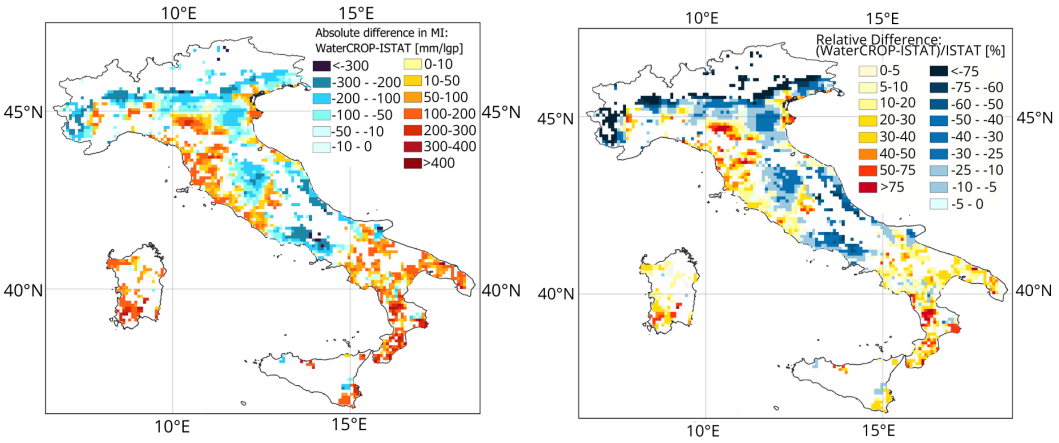

(a) (b)

Fig. 2.12. (a) Absolute and (b) relative differences in irrigation water demand of maize in 2010 computed by WaterCROPv2 and ISTAT.

with dry (e.g. 2010-2011) and wet seasons (e.g. 2006-2007) [153]. The mean present state was evaluated by averaging the I_{mz} values for each simulated year. As defined in Equation 2.14, the mean I_{mz} is defined as maize blue water demand (I_b) divided by weighted irrigation systems efficiencies. For each cell, the weight of each irrigation system is based on the relative number of hectares irrigated with that system with respect to the total amount of irrigated hectares. Figure 2.13a and Figure 2.13b show I_{mz} in cubic meters and millimeters, respectively, presenting two different perspectives. The cubic meters perspective reveals the total, actual amount of water used for maize in a specific cell. However, it does not provide information on the areal density of such amount of water. The millimeters, instead, corresponding to the normalization of the m^3 over the cultivated areas, provide this detail. Millimeters highlight which areas are more suitable for maize cultivation due to the local climate. The evident gradient in mm-demand from the wetter north to the drier south points out how the local climate strongly influences the water demand. Two good examples are Pianura Padana (red rectangle) and Salentino (green rectangle). In Pianura Padana, climate and soil are suitable for maize growth, with I_{mz} generally below 120 mm/lgp, leading to a large maize cultivation and high volumetric water demand (above 200,000 m^3/lgp). In contrast, Salentino area has a much drier climate, resulting in high mm-demand and less extensive maize cultivation, thus leading to a lower m^3 demand. It is noteworthy that most areas with the highest I_{mz} correspond to regions where maize is the primary crop (Figure 2.7a)

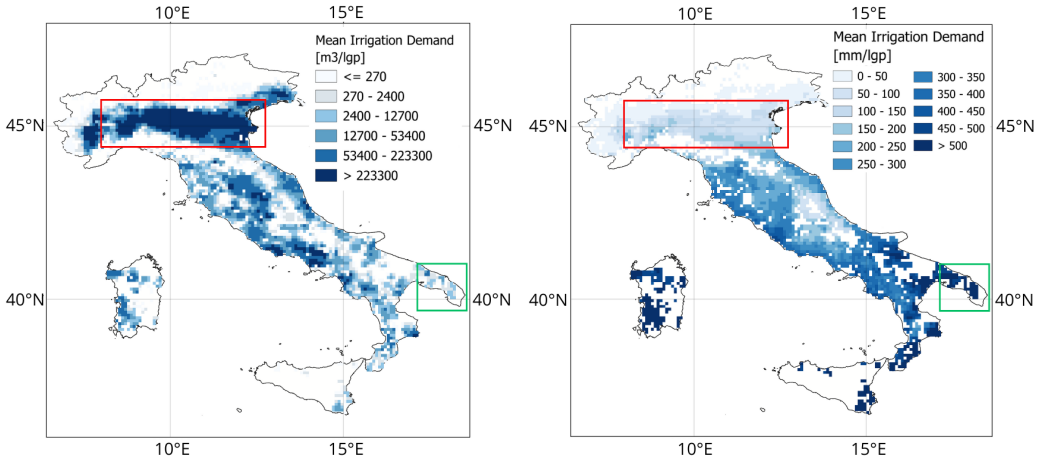

(a) (b)

Fig. 2.13. Map of modeled mean irrigation demand by maize in Italy expressed in (a) cubic meters, (b) millimeters. The red rectangle spotlights the Pianura Padana region while the green one encloses the Salentino region.

making maize the pivotal crop in those areas. The areas showing high or small water demand in both maps are areas the attention of decision-makers should be driven to. In fact, dark-blue cells in both maps are regions where the present extensive cultivation is actually located in areas poor in rainwater, and thus crop shifts should be put in place, light-grey cells, instead, spotlight zones where maize cultivation should be developed (focusing only on the maize perspective) as is not yet largely present despite favorable climate.

The key sources of uncertainty, cell by cell, in the I_{mz} evaluation are the irrigation system heterogeneity and their efficiencies. While it is not possible to assess a range of local efficiencies in the absence of more information, instead a reasonable computation of the uncertainty in I_{mz} due to the heterogeneity and the relative relevance of the irrigation systems can be carried out. To the purpose, other two possible values of α were considered: respectively they correspond to the scenarios of upper (lower efficiency) and lower (higher efficiency) boundaries of I_{mz}. They can be defined based on whether maize was assumed to be irrigated primarily using less or more efficient irrigation systems: the upper α value was computed covering the irrigated area from the least efficient irrigation system to the most efficient one until exhaustion. For the lower α value, the irrigation systems were applied from the most efficient to the least efficient. Figures 2.14a and 2.14b display the offsets of the highest and lowest I_{mz} values, respectively as percentage deviations with respect to

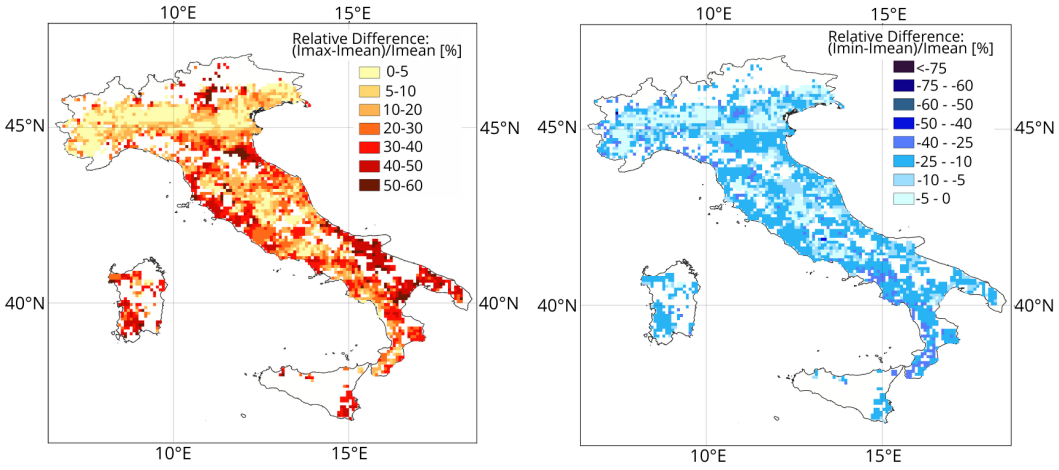

(a) (b)

Fig. 2.14. Relative difference of modeled (a) maximum and (b) minimum irrigation water demand with respect to the mean irrigation requirement.

mean values. The correspondence of zones with the smallest deviations - [0-5%]: light yellow for the upper limit and light blue for the lower limit - among the figures indicate higher reliability of I_{mz} values, due to a smaller heterogeneity of irrigation systems in those areas. These cells account for almost 15% of the cells. In the majority of the cells (92%), the lower I_{mz} deviates less than 25% from the mean, while in 67% of cells the higher I_{mz} is at most 30% larger than the mean. This skewness of distribution around the mean is due to the fact that micro-irrigation, the most efficient system, covers less than 18% of the irrigated areas while flow irrigation, one of the least efficient methods, is used on over 30% (Table 2.4). If local information on the applied irrigation system were available, the uncertainty would be limited to the irrigation efficiency values, whose uncertainty has a smaller impact on I_{mz} computation at the national level.

Scenarios analysis

A key use of agro-hydrological models, such as WaterCROPv2, is to evaluate irrigation water demand. However, even though they are generally used as assessment tools, they can also be applied as modelling tools. In this sense, they are key instrument to analyze scenarios and propose alternatives to the current state. For instance, it is possible to analyze the effect of changing irrigation thresholds (e.g. irrigation

up to fractions of field capacity) or timing (e.g. biweekly, weekly), to study the impact of different irrigation systems and to investigate the effects of climate change. These scenarios are fundamental to take the right decisions on the management and planning of water resources. As an example, we report here (Figure 2.15) the hypothetical scenario where maize is irrigated solely by micro-irrigation. It can be useful for critical analysis, localization, and quantitative evaluation of the water savings of potential investments in new micro-irrigation systems. Figure 2.15 shows that at national level the mean water saving is 21% and in 75% of the cells it goes up to 28% (59 mm/lgp) In some areas it can have even larger effects: it is evident how the strongest potential water-use reduction of 30-40% is mostly located close to the Alps and the southern Apennines where flow irrigation is now predominant due to the abundance of water (Figure 2.7b). This information becomes particularly valuable when considering future temperature and precipitation projections. Studies on climate change impacts foresee in the areas close to the mountains an increase in mean temperature of 4°C and a shift of precipitation distribution towards winter periods causing an increase in drought spells in summer [154]. Thus, the increased evapotranspirative water demand caused by the higher temperatures will find even less support in the precipitation water, increasing the stress on the irrigation water.

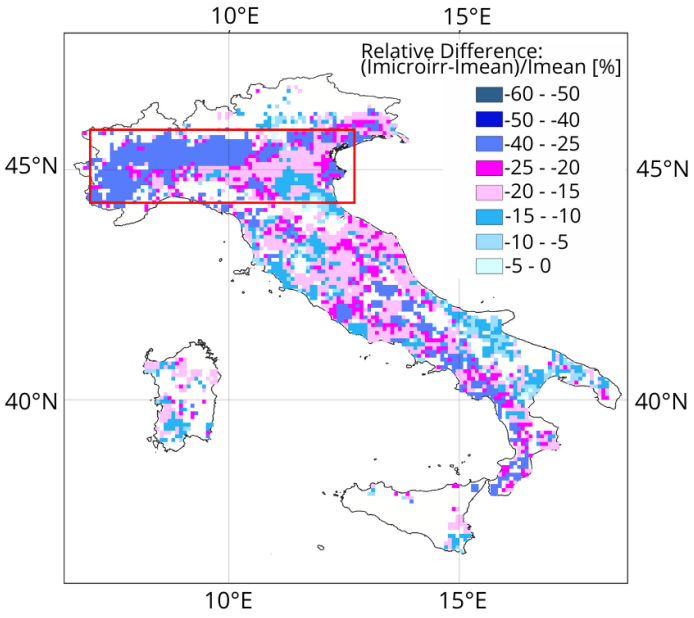

Fig. 2.15. Percentage difference in modeled irrigation water demand when only micro-irrigation is used, compared to the mean irrigation requirement under current mixed irrigation systems.

It is also possible to evaluate how incentives on the increase of micro-irrigation use (where it is already present) can still bring a 5-10% saving. This 5-10% saving becomes of high interest in regions, such as Salentino region (recall the green rectangle in Figure 2.13a), very scarce in rain water. Figure 2.16 shows both the preferred irrigation system (indicated by color) and the amount of water (indicated by shades) currently used in each cell where maize is cultivated. This pair of information allows one to better understand where potential investments would have the greatest impact as it spotlights where large amounts of water are conveyed on the field with inefficient systems. For example, the dark-blue and dark-green areas, corresponding to central regions of Pianura Padana (recall the red rectangle in Figure 2.13a), can be identified as key target areas for implementing the most effective changes in irrigation systems: they result the most water-demanding zones and with the most inefficient irrigation systems on ground. At the same time, it is possible to evaluate the feasibility of changing irrigation systems: investments in micro-irrigation are more likely to be done on fields without existing equipment rather than on areas already equipped with sprinklers.

Table 2.4. Extension of the areas irrigated with a specific irrigation system in Italy, their efficiencies in Italy [145], and their relative relevance at national scale.

Irrigation system	**Coverage** $[10^3 \cdot$ **ha]**	**%**	**Efficiency** η
Submersion	221.0	9	0.25
Micro-irrigation	423.0	17	0.9
Flow and Lateral infiltration	748.4	31	0.55
Sprinklers	958.5	40	0.75
Other	68.4	3	0.7

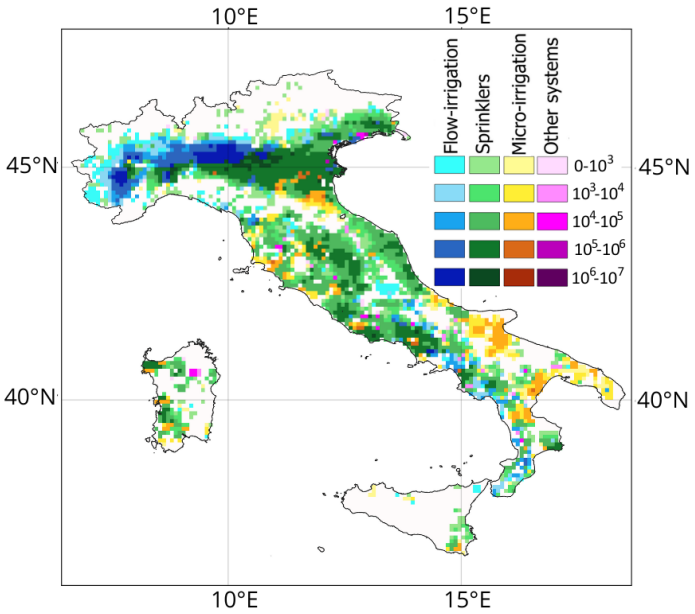

Fig. 2.16. Classification of I_{mz} according to irrigation system (flow irrigation in blue, sprinklers in green, micro irrigation in yellow) and volumetry class (reported to the right of the color legend, in m^3).

2.3 Sensitivity analysis

A sensitivity analysis was carried out to evaluate the impact of data uncertainty on the estimation of water demand, ET_b. To this aim, selected quantities were perturbed one at a time to assess their individual impact on the model. To compare the sensitivity of ET_b to the different quantities, q, the normalized sensitivity index, SI_q, was applied [137]:

$$SI_q = \frac{\Delta ET_{b,q}}{ET_{b,q}} / \frac{\Delta q}{q} \tag{2.15}$$

where $\Delta ET_{b,q}$ is the variation that ET_b undergoes due to the quantity perturbation, Δq. We focused on the sensitivity with respect to four key input parameters: maximum rooting depth, Zn_{max}, relative soil water content at field capacity, θ_{fc}, interception, T, and precipitation P. Rooting depth and interception were considered to test the impact of simplifying assumptions in the model; in fact, WaterCROPv2 root growth

throughout the entire season does not depend on environmental conditions that may alter the potential growth —whereas in reality, growth rates vary depending on external factors such as soil compaction, water availability and microbial activity-, and an interception independent of canopy extension. Variations in θ_{fc} reflect the challenges of characterizing soil properties at the cell scale, as they vary within fields and across soil profiles due to agricultural practices (e.g., compaction). Finally, precipitation can display highly localized patterns (particularly in spring and summer) that may not be captured by spatially distributed datasets. Positive and negative variations of 5% were applied to analyze the model's response in terms of both the magnitude and direction of change (Table 2.5).

Table 2.5. sensitivity analysis: tested quantities and their associated variations in water demand.

Variable	Description	Initial value	Variation	Final value	National Water demand variation	National SI_v
Zn_{fin}	Maximum rooting depth	1 m	±5%	1.05 / 0.95	-0.83% / +0.84 %	-0.166 / +0.168
θ_{fc}	Relative soil water content at field capacity	0.275 (silty-clay-loam)	±5%	0.28875 / 0.26125	+ 4.44% / - 4.13%	+ 0.88 / -0.826
		0.225 (loam)	±5%	0.23625 / 0.21375		
		0.125 (loamy-sand)	±5%	0.13125 / 0.118		
T	Interception	0.5 mm	±5%	0.525 / 0.475	+ 1.03% / -1.00%	+0.206 / - 0.2
P	Precipitation	site and hourly specific	±5%	site and hourly specific	- 5.10% / +5.53 %	-1.02 / + 1.106

Figure 2.17 illustrates the variability of SIq for each perturbed quantity. Lighter and darker shades correspond to negative and positive 5% variations of the quantities, respectively. The extent of the boxplots reflects the spatial variability of SI across Italy. It is evident that soil properties, θfc, and precipitation, P, have the greatest influence, while rooting depth, Zn_{fin}, and the interception threshold, T, exhibit smaller effects. Additionally, negative and positive perturbations produce effects that are similar in magnitude but opposite in direction: on average, soil properties and precipitation and have a SI equal to ±0.86 (-0.79/+0.93) and ±0.8 (+0.84/-0.75), respectively, while Zn_{fin} and T ±0.20 and ±0.17 respectively. The magnitude of the variations at the local scale is consistent across scales, being comparable to the national-level evaluations (Table 2.5). Overall, the stability analysis indicates that the model is robust, as changes in the input quantities produce output variations smaller than the perturbations themselves (i.e., $SI < 1$).

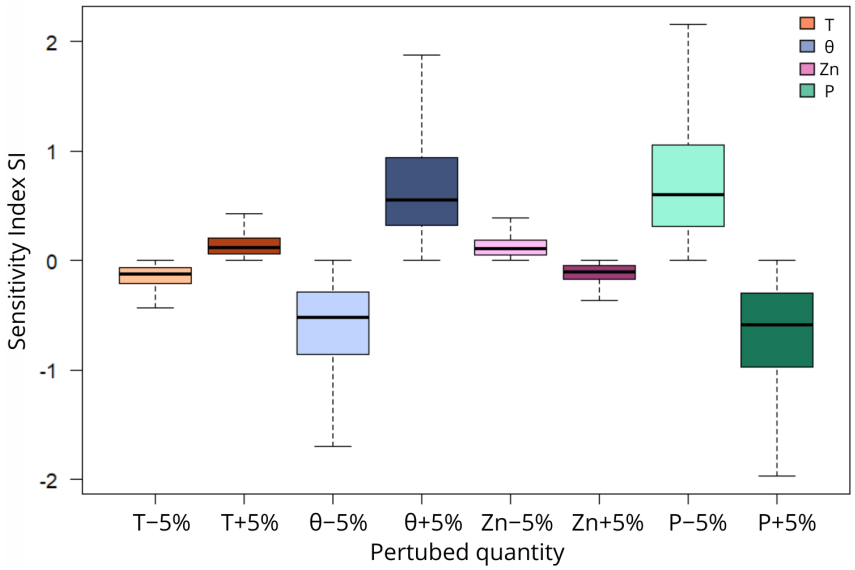

Fig. 2.17. Boxplots of the sensitivity index, *SI*, of the water demand evaluated with WaterCROP model. The x-axis shows the perturbed quantities (both positive and negative): interception threshold, T, relative water content at field capacity, θ_{fc}, maximum rooting depth, Zn_{fin}, and precipitation, P.

2.4 Conclusions and recommendations

The aim of this work was to provide a physically-based agro-hydrological model that could balance the reliability of the evaluation of irrigation water demands at regional scales with the simplicity of required inputs and short computational time demand. WaterCROPv2 encloses these characteristics. By building on the original WaterCROPv1 model, it maintains the use of readily accessible data but enhances the precision of evapotranspiration calculations through the inclusion of hourly resolution, daily plant physiology, rainwater interception and leakage dynamics, all factors critical for regions with diverse climates and irrigation practices. However, the authors acknowledge that the model has some limitations under extreme conditions, as it does not account for processes such as the reduced root and canopy growth under severe stress, soil hysteresis, or water stress caused by excess water. In addition, it was specifically developed for herbaceous and seasonal crops and is not directly applicable to trees or perennials. Nevertheless, WaterCROPv2 provides improved irrigation demand estimates compared to the previous version and shows good to excellent agreement with reference data and previous studies at the local scale. This consistency demonstrates that, despite its lower complexity and non-site-specific

input data, the model is able to reliably estimate crop water needs. Furthermore, sensitivity analysis with respect to key quantities demonstrated the robustness of the proposed model's outputs."

The application of WaterCROPv2 to maize cultivation in Italy was used to show the potential of the model to be applied as a valuable decision-making tool for water managers and policymakers. Specifically, the model offers an efficient approach to assess current irrigation needs as well as to develop future sustainable water management practices. The evaluation of the mean irrigation water demand of maize (2005-2015) allowed us to identify areas where maize production is either suitable or unsustainable due to the climatic conditions and to spotlight the most water-demanding zones. The possibility to include different precipitation patterns and simulate irrigation scenarios (e.g. irrigation systems and timings) allowed us to evaluate the effects of these variables on water demand and decide for investments accordingly. The presented example scenario showed the impact of switching maize irrigation entirely to micro-irrigation, reckoning a mean national reduction of 21% in water use with potential savings of up to 30–40% in areas characterized by high water availability. Furthermore, by intersecting water demand maps with irrigation system maps, it was possible to gain critical insight into the areas that would benefit the most from investments in upgrading irrigation systems.

In conclusion, in the perspective of increasing water scarcity and the growing need for efficiency, WaterCROPv2 provides a practical way to assess the sustainability of agriculture in a given area and identify where adjustments are most urgent and effective. The simplicity of the model allows evaluations to be carried out without the need for specialized expertise, while preserving process transparency and mitigating the 'black-box' effect characteristic of more complex approaches.

Chapter 3

Hydroclimatic link between the Alps and agriculture in the Pianura Padana region

The Alps have been recognised as hotspot areas for European climate change impacts [6, 155]. The ongoing and future changes in the alpine hydrological cycle concern not only snowmelt magnitude and timing but also incoming precipitation and outgoing evapotranspiration fluxes [155, 156]. Evapotranspiration plays a major role in the water balance of alpine catchments as, on average, it pumps back to the atmosphere a third of the incoming precipitation, with values reaching up to 60%, and thus strongly regulating precipitation recycling [157, 158]. However, its importance is not limited to the alpine region but goes far beyond the Alps, influencing the water availability in downwind areas supplying precipitation water across Europe. One of the main affected sectors is agriculture. In fact, lowland agriculture is connected to the Alps not only in terms of riverine water but also through these atmospheric moisture fluxes. Thus, it becomes clear how the moisture recycling and downstream effects of changes in alpine ET are not only hydrological but also extend to economic aspects and socio-political dimensions. Understanding these dynamics is crucial to addressing challenges in water resource management, land use, agricultural sustainability, and energy production. While the study on the regions supplying precipitation water to mountain regions have been historically carried out through the analysis of the isotopic composition of collected rain, snow or ice samples [81], only recently the topic has been addressed through moisture tracking analysis. This complementary

approach allows analyses without the need for field sampling or laboratory knowledge and analyses, while allowing the investigation of large spatial domains and arbitrary time periods, including climatological mean behaviours, without waiting for years of observations or large ice core sampling. While some studies have addressed the sources of precipitation over the Himalayas [159–161], only very few studied the Alps as sink of moisture: in 2004 Berto et al. applied Lagrangian tracking to back-track water vapour contributing to a specific precipitation event, in 2009, Sodemann and Zubler studied the mean (1995–2002) origin of precipitation on the Alps. Furthermore, to the best of the author's knowledge, no other study has been conducted on the destiny of outgoing evaporative fluxes from the Alps, and especially not on the bilateral connection between the Alps and lowland agriculture. Consequently, despite increasing recognition of the Alps as a key component of the European hydroclimate system, their role as a source of atmospheric moisture and their coupling with downwind areas remain poorly quantified.

Thus, to address this knowledge gap, in this study we apply a moisture tracking approach to investigate (i) the geographic origin of the water that precipitates over the Alps, (ii) the fate of evapotranspired alpine moisture, and (iii) the bidirectional atmospheric linkage between the Alps and the Pianura Padana agricultural region. By quantifying these moisture pathways, this work moves beyond the traditional view of the Alps and the agricultural land as solely linked by riverine water.

3.1 Data and Methods

This study utilizes the openly accessible RECON dataset. This dataset offers mean annual global moisture tracking trajectories derived by a Lagrangian moisture tracking model (refer to Section 1.3 for a description), along with climate model data, specifically precipitation and evapotranspiration from ERA5-Land.

RECON: To track moisture through the atmosphere from evaporative sources to precipitation sinks has become common to apply Lagrangian models [69, 90]. A widely used model is the UTrack model [90], which follows the trajectories of moisture parcels while updating their budget according to local wind fields, additional evaporation, and releases of precipitation. For every mm of evaporation, the model tracks 100 parcels of moisture and the original water is traced up to 30 days or until 99% of the moisture has not rained out. The model is forced with ERA5

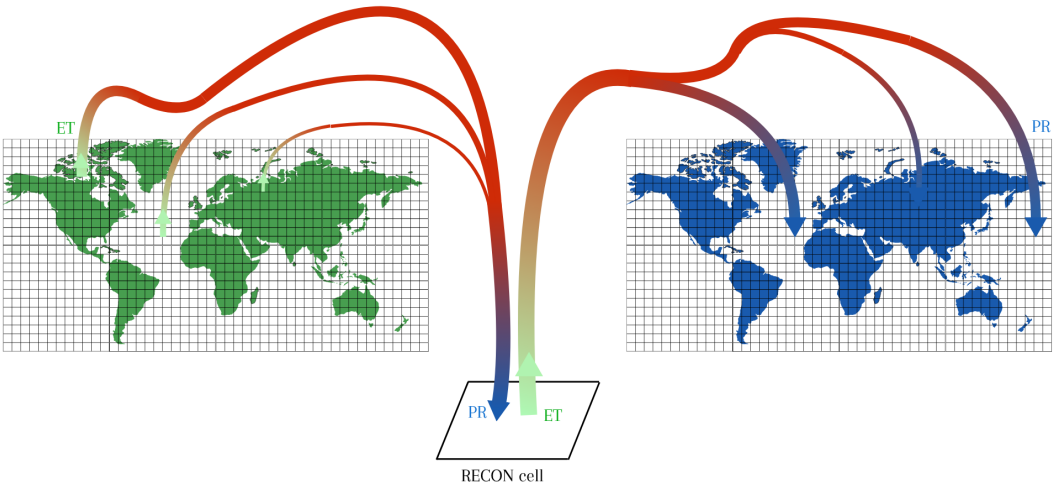

Fig. 3.1. Graphical representation of RECON database: upwind and downwind plumes

hourly atmospheric reanalysis data at 0.25×0.25° spatial resolution but the output is provided as monthly averages at 0.5°.

Given the analysis in terms of annual average values carried out in this study, it was preferred to use the RECON database [164], which is based on UTrack output data. RECON database provides the yearly reconciled output of UTrack, ensuring the closure of the global hydrological cycle at the yearly scale (yearly global precipitation = yearly global evapotranspiration) thanks to the Iterative Proportional Fitting (IPF) procedure.

This dataset provides values for the mean year between 2008 and 2017. The dataset, as the former UTrack available output, does not provide spatial trajectories but rather a multidimensional dataset that allows for the extraction of the upwind and downwind plumes for every analyzed cell c (Figure 3.1).

The plumes are provided as global gridded matrices containing cumulative annual moisture values for each grid cell. For the upwind plume, the values represent the total amount of moisture that evaporated throughout the year and eventually precipitated over the target cell c. Conversely, the downwind plume reflects the cumulative moisture that precipitated over the year and was originally evapotranspired from cell c.

ERA5-Land: The complex orography of the Alps implies highly localized and variable meteo-climatic zones which can be poorly represented by the coarse resolution of the RECON dataset. Thus, RECON was coupled with ERA5-Land evapotranspiration and precipitation data. The choice was driven by the need for high-quality but also spatially distributed inputs, making local measurements unsuitable due to limited coverage. ERA5-Land was selected for its finer spatial resolution (0.1°) with respect to RECON, its consistency with the original ERA5 forcing dataset as part of the Copernicus Climate Change Service products, and its widespread use as a reference in environmental research.

To define the precipitation, P_{AB}, occurring in a cell sink B due to evaporation in a source cell A, ERA5-Land and RECON were coupled as:

$$P_{AB} = P_B \frac{P_{A_R B_R}}{P_{B_R}} \tag{3.1}$$

where A_R and B_R refer to the corresponding RECON source and sink cells that contain the ERA5-Land cells A and B, respectively. P_B and P_{B_R} represent the total precipitation over B (from ERA5-Land) and over B_R (from RECON), respectively, and $P_{A_R B_R}$ represents the precipitation that occurred over B_R due to moisture that, according to RECON, previously evaporated from A_R.

Note that, as moisture fluxes are bilateral, P_{AB} corresponds to ET_{AB}, the evapotranspiration from A_R that will eventually fall as rain over B:

$$ET_{AB} = ET_A \frac{ET_{A_R B_R}}{ET_{A_R}} \tag{3.2}$$

where ET_A and ET_{A_R} represent the total evaporation from A (from ERA5-Land) and from A_R (from RECON), respectively, while $ET_{A_R B_R}$ represents the moisture budget that evaporated from A_R and, according to the moisture tracking model, ultimately precipitated on B_R.

Equations (3.1) and (3.2) implicitly embed the connections among grid cells evaluated by the moisture tracking model UTrack through the use of the relative moisture fluxes provided by RECON, but correct the absolute magnitude according to ERA5-

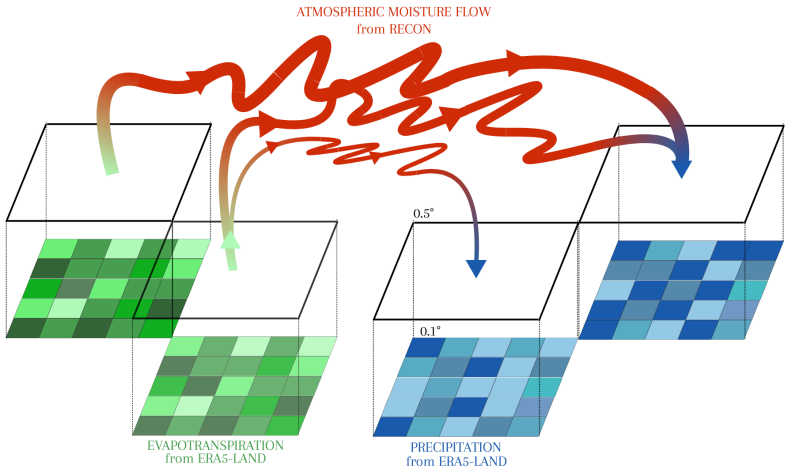

Fig. 3.2. Graphical representation of ERA5-Land and RECON coupling: larger cells represent the spatial resolution of RECON, while smaller cells depict the finer grid of ERA5-Land. Evapotranspiration and precipitation fluxes from the ERA5-Land dataset at 0.1° resolution are coupled with atmospheric trajectories from RECON at 0.5°.

Land values. It is important to note that RECON's and ERA5-Land's lattices align and, thus, every RECON's grid cell contains 25 ERA5-Land's cells. This implies that all 25 cells share the same connections with the other cells around the world (Figure 3.2).

3.1.1 RECON and ERA5-Land consistency

Before applying and analyzing the coupled ERA5-Land - RECON setup, a consistency check was performed to ensure the datasets were sufficiently aligned for meaningful and reliable coupling. This involved comparing precipitation and evapotranspiration values using their relative cumulative distribution functions (CDFs), with ERA5-Land assessed both at its native resolution and after being upscaled to match the coarser resolution of RECON (Figure 3.3). Precipitation values (Figure 3.3a) show strong agreement at both scales while evapotranspiration (Figure 3.3b), besides a general good consistency, shows a larger variability among the two datasets and across scales. When upscaled (ERA5-Land regridded), ERA5-Land displays increased deviation from its original high-resolution values, indicating a higher spatial heterogeneity, especially in comparison to the precipitation field, which shows stronger homogeneity. Generally, ERA5-Land exhibits lower evapotranspiration values ($\overline{ET}$ = 463 mm) compared to RECON ($\overline{ET}$ = 483 mm), highlighting the value

of using a higher-resolution dataset. The discrepancies in the lower values of ET are mainly attributable to high-altitude areas, where lower evapotranspiration rates are captured by ERA5-Land but not by RECON due to the different spatial resolution. Since evapotranspiration is known to vary with elevation, these results suggest that finer-resolution datasets, like ERA5-Land, are better suited to represent the spatial heterogeneity of complex terrains such as those of mountainous regions.

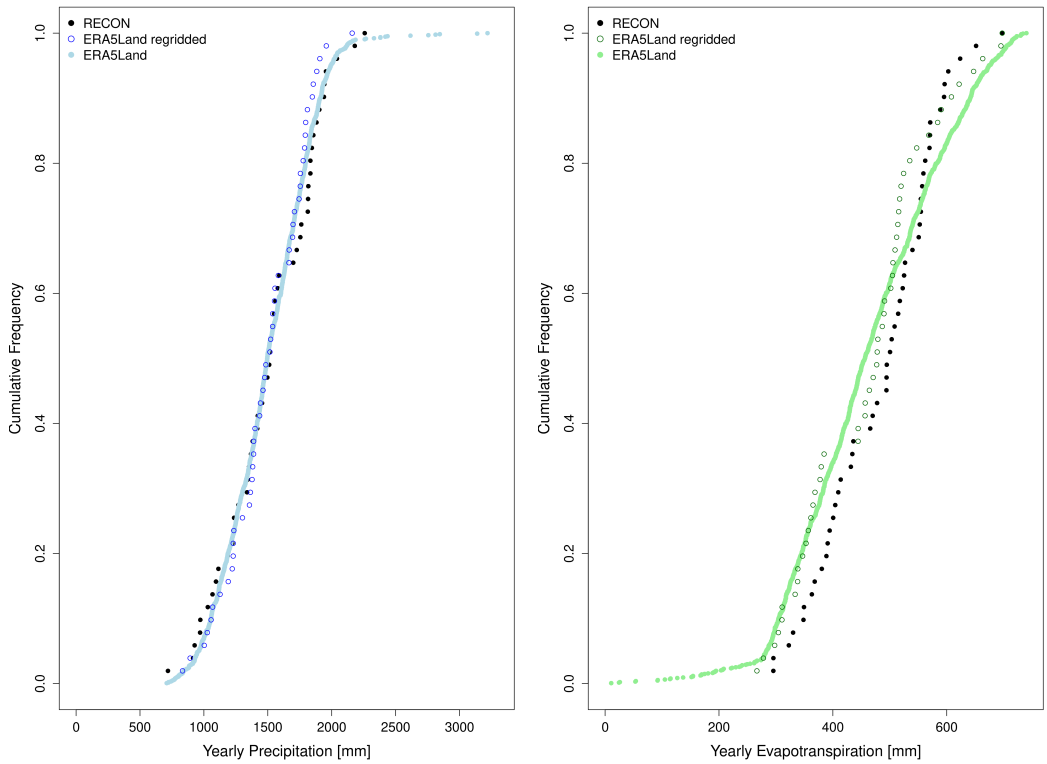

(a) (b)

Fig. 3.3. Cumulative density function of yearly (a) precipitation, (b) evapotranspiration according to RECON, ERA5-Land, and the regridded ERA5-Land. RECON is shown in black, ERA5-Land at original scale in light-blue (left) and light-green (right), ERA5-Land regridded at RECON scale in blue (left) and dark-green (right). Each point represents a cell inside the Alps border.

The reliability of ERA5 and ERA5-Land in providing accurate precipitation and evapotranspiration estimates in complex terrain such as the Alps has been and still is an open research question. In fact, modeling such variables in mountainous regions is intrinsically challenging due to strong spatial variability in elevation,

localized phenomena, and the presence of microclimates. Even the validation remains challenging and, most often, its evaluation accuracy differs between different variables: precipitation biases are better documented than evapotranspiration ones, as there are more pluviometers than eddy-covariance towers in the Alps.

Although ERA5-Land generally shows reasonably good overall performance and higher accuracy if compared to ERA5, several studies have highlighted highly spatially variable accuracy in complex terrains [165, 166]. In particular, evaluations over the Alps and other mountainous regions report a tendency in precipitation overestimation of 10-20% [166, 167]. This bias can be related to the challenges in representing orographic processes and cloud dynamics. Thus, for more localized studies, alternatives can be found in localised datasets (e.g. MERIDA for the Italian Alps) and bias-corrections commonly applied in climatological studies [168].

Unlike precipitation, evapotranspiration does not show a general bias trend. Different models are reported to both overestimate and underestimate fluxes in different areas [156]. In ERA5-Land, evapotranspiration corresponds to potential evapotranspiration (PET). PET is computed through the surface energy balance assuming a reference vegetation type (crops) and no soil moisture stress [165]. While this assumption can lead to unrealistic evaporation estimates in water-limited or arid environments, its implications in alpine regions are likely less critical. Importantly, Muñoz-Sabater et al.(2021) assessed the performance of ERA5-Land against in situ observations for several key variables related to PET estimation, including soil moisture and surface energy fluxes (latent and sensible heat fluxes). The results indicate that ERA5-Land compares fairly well with the measurements and improves the representation of the terrestrial water cycle compared to ERA5, particularly for soil moisture. These findings support the added value of ERA5-Land, especially for hydrological applications.

In addition to these considerations, it is important to note that reanalysis datasets are often the only reasonable option for regional to large-scale studies, such as the present study, as they provide spatially and temporally consistent data, ensuring reasonable overall accuracy. In fact, local measurements offer high accuracy at specific locations but are inherently point-based and therefore not directly representative at larger spatial scales and would require krigging processes to become spatially distributed. Moreover, observational datasets are often fragmented, difficult to access, particularly in studies that cross national borders, where data policies can increase

the retrieval challenges. In principle, ERA5-Land data could be further improved through bias correction using local observations; however, while it would enhance regional accuracy, it would require high computational resources and considerable time, which may not always be feasible.

In conclusion, despite the reliability of ERA5-Land in complex mountainous terrain remaining an active area of research, multiple studies demonstrated the improvements with respect to previous reanalysis products, highlighting both its strengths and limitations, making it an easily employable dataset for the present study.

3.1.2 Major players: RECON, Pianura Padana and the Alps

The Pianura Padana was selected as the focus of Italian agriculture in this study, as preliminary analyses indicated that this region exhibits the strongest atmospheric connectivity with the Alpine domain. To identify agricultural land within the region, the FAO GLC-SHARE dataset [16] was employed. This dataset provides the fractional coverage of agricultural land at a spatial resolution of 1 km. Pixels were classified as agricultural land if at least 90% of their area was covered by agricultural land use. The resulting spatial distribution of agricultural areas across the study domain is shown in Figure 1.1. Thus, it is important to note that the terms *Pianura Padana* and *Pianura Padana agriculture* refers to two different spatial extents, with the latter covering roughly a little more than half of the former.

To define the Alpine region, this study adopts the geographical delineation provided by the Alpine Convention [169]. The Alps constitute a complex mountainous system that supplies a substantial portion of Europe's freshwater resources through several major river networks. Four primary drainage basins can be identified: the Mediterranean basin, mainly drained by the Rhône; the North Sea basin, dominated by the Rhine; the Black Sea basin, associated with the Danube; and the Adriatic basin, largely supplied by the Po River. These major watersheds provide a natural framework for distinguishing the northern and southern sides of the Alpine range. In particular, the hydrological divide separating the Adriatic basin from the remaining basins marks the transition between the southern and northern Alps.

Figure 3.4 illustrates the adopted subdivision: the Alpine region boundary is shown in red, while the northern and southern Alps are highlighted in light blue and dark

blue, respectively. Throughout this study, references to the northern and southern sides of the Alps are based on this hydrological classification.

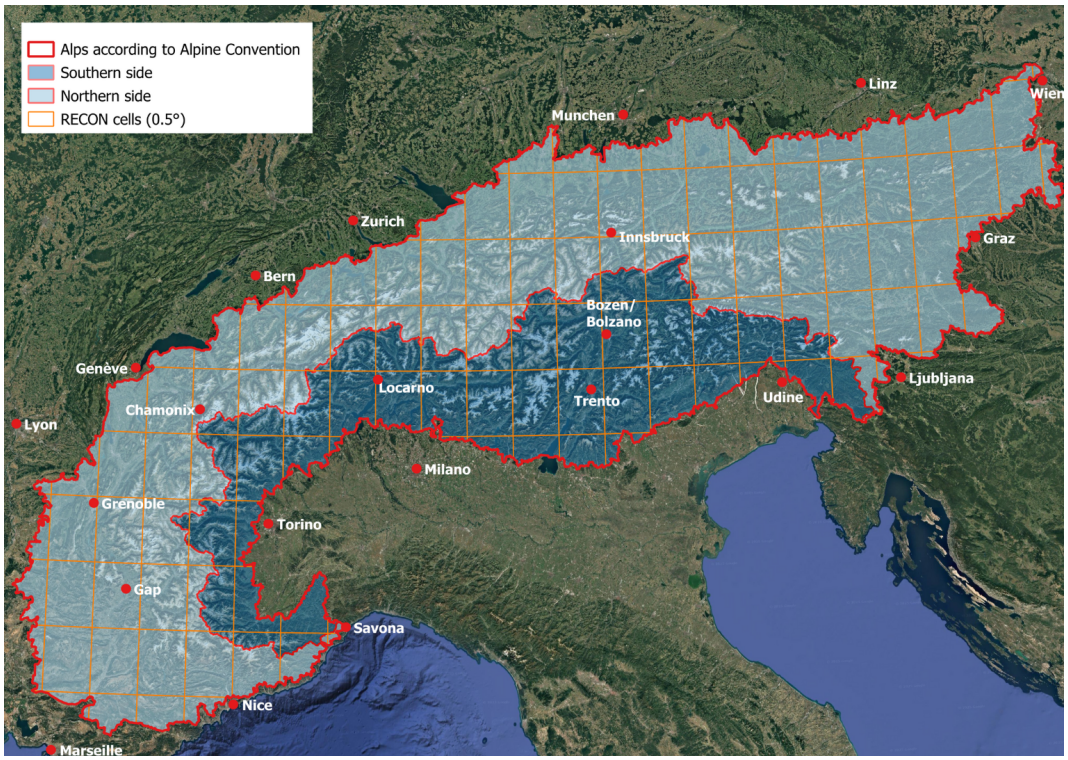

Fig. 3.4. Subdivision of the Alps into northern (light blue) and southern (dark blue) regions based on the main hydrological divide. The RECON grid is shown in yellow.

The yellow grid in Figure 3.4 represents the spatial distribution of RECON cells over the Alpine arc. Not all grid cells are entirely contained within the Alpine boundaries, nor can all of them be unambiguously assigned to either the northern or southern Alps. In cases where grid cells partially overlap the Alpine region, incoming and outgoing fluxes were proportionally scaled to account only for the fraction of the cell area lying within the Alpine domain.

Similarly, when a grid cell intersects both the northern and southern Alpine regions, the associated flux F (e.g. precipitation or evapotranspiration) was partitioned proportionally according to the area of overlap, as expressed by:

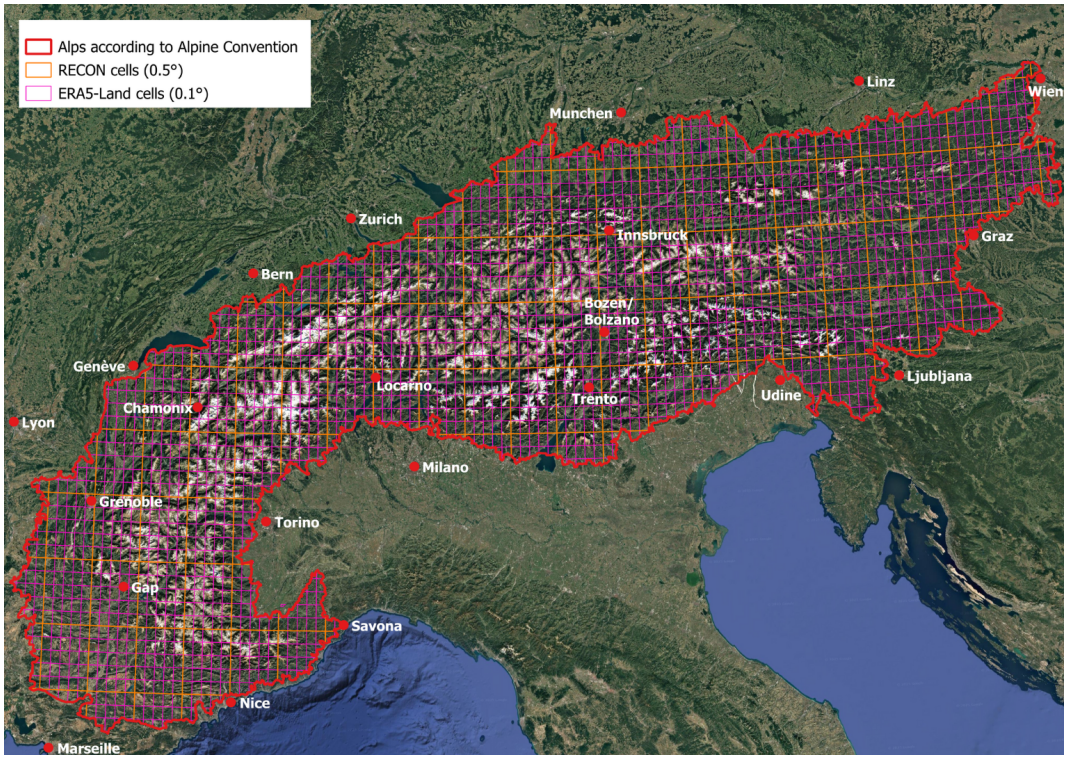

Fig. 3.5. Spatial intersection between RECON (yellow), ERA5-Land (magenta), and the Alpine region.

$$\begin{cases} F_{A_{Rnorth}} = F_{A_R} \dfrac{Area_{A_{Rnorth}}}{Area_{A_R}} \\ F_{A_{Rsouth}} = F_{A_R} \dfrac{Area_{A_{Rsouth}}}{Area_{A_R}} \\ Area_{A_R} = Area_{A_{Rnorth}} + Area_{A_{Rsouth}} \end{cases} \tag{3.3}$$

An analogous procedure was applied to ERA5-Land grid cells. Figures 3.5 and 3.6 show the spatial intersections between the RECON grid (yellow), the ERA5-Land grid (magenta), and the Alpine region and Pianura Padana agricultural areas, respectively.

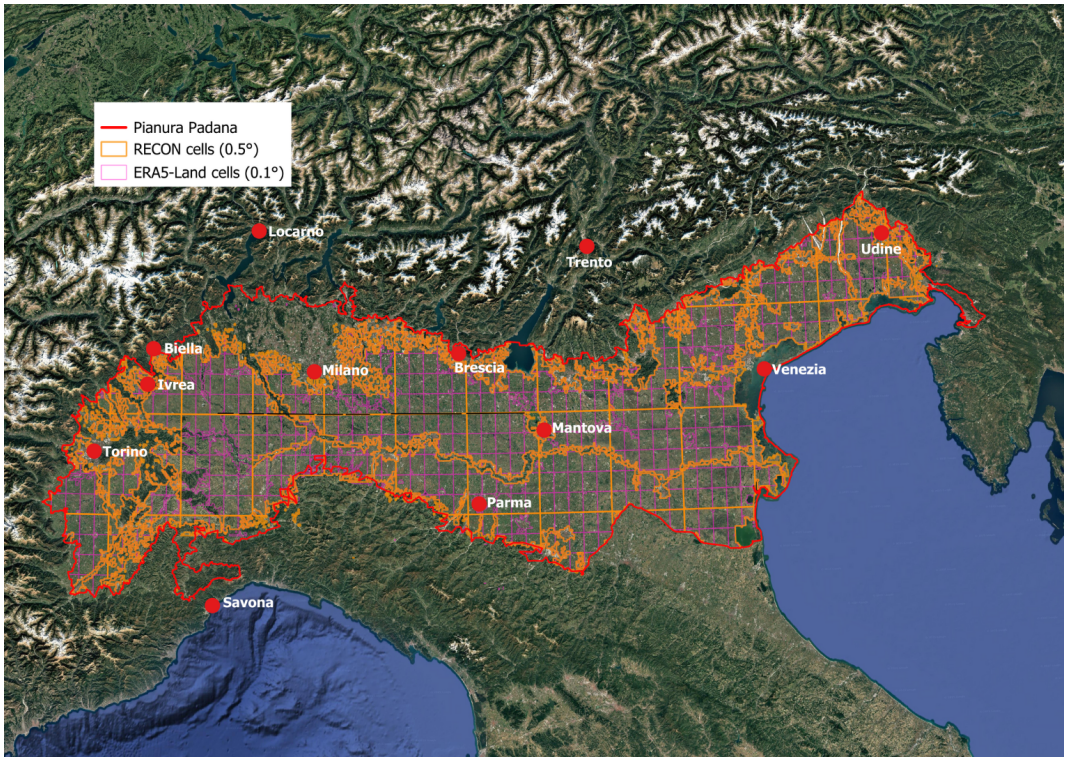

Fig. 3.6. Spatial intersection between RECON (yellow), ERA5-Land (magenta), and agricultural land in the Pianura Padana.

3.2 Results and Discussion

3.2.1 The Alps as sink and source of moisture

The Alps play the role of both water towers and precipitation source for the European lowland. The incoming precipitation plays the important role of replenishing the Alps with water that is then redistributed in the hydrological cycle through the seasonal river runoff, the mass balance of glaciers, and the interconnection with the atmosphere via evapotranspiration. This highlights the importance of understanding the mechanisms that bring water vapor from evapotranspiration sources to the Alps, one of the nodes of the European water supply.

Incoming precipitation

Thanks to the coupling of RECON and ERA5-Land, it was possible to define the mean yearly upwind basin contributing to precipitation on the Alps (Figure 3.7). The colored area represents the mean annual Alpine precipitation projected backward to the respective source of evapotranspiration, while the shading shows the contribution of the local evapotranspiration sources to the precipitation on the Alps.

Most of the sources are located in the northern hemisphere, and the Mediterranean Sea, the north Atlantic Ocean, and Europe stand out as the main contributors to Alpine precipitation. In fact, these areas fall in the main basin, from dark green to orange, that accounts for 99% of the moisture that eventually falls on the Alps and finds its moisture source maximum on the Mediterranean Sea. It is important to note that a quantitative interpretation of the different zonal sources (e.g., Oceanic, continental, Mediterranean) is not possible from Figure 3.7 as it does not take into account the areal extent of the moisture zonal sources and the contribution as cell specific.

The shape of the moisture plume and the magnitude of local contributions reflects the fact that it is the superposition of mean daily inputs during different seasons. This spatial pattern depends on the interplay between larger-scale atmospheric circulation and more regional climatic processes throughout the year. The elongated shape of the plume can be attributed to winter conditions, when the strong geostrophic winds dominate the transport of moisture. These winds blow from west to east, transporting moisture from the north Atlantic to Europe. In summer, instead, the influence of these westerly winds diminishes, reducing the dominance of Atlantic

moisture transport and allowing for more localized, convective moisture transport. This results in stronger contributions from the Mediterranean Sea and Europe.

To quantify the contribution of different moisture sources to Alpine precipitation, the evapotranspiration area was divided into three major macro-regions: the Atlantic Ocean (north and south), the Mediterranean Sea, and Land, as shown in Figure 3.8a. To minimize the influence of minor or noisy sources and focus on the dominant contributors, only the regions responsible for 99% of total Alpine precipitation were considered. The resulting main contributing areas, highlighted in Figure 3.8b, are the north Atlantic Ocean, the Mediterranean Sea, north-east America, north-west Africa and Europe.

Over the period 2008–2017, the mean annual volume of moisture contributing to precipitation over the Alps amounts to approximately 286 km^3 per year. This value is sum of all atmospheric moisture fluxes that ultimately result in precipitation over the Alpine region. When distributed spatially over the entire Alpine arc, the flux corresponds to an average of 1505 mm of precipitation per year. Table 3.1 lists the mean annual moisture source contributions highlighting the prevalence of the marine source. In fact, the north Atlantic Ocean and the Mediterranean Sea contributions account for 61.6% of the total Alpine precipitation while evapotranspiration processes occurring on land account only for 37.5%. The strongest single contributor is the north Atlantic Ocean (40.6%), followed by Europe (31.6%) and the Mediterranean Sea (21%). Even though the north Atlantic Ocean brings in the largest amount of water (116 km^3), when normalized by the relative contributing oceanic extension, the local conditions on temperature and pressure produce an effective evaporation rate of 2.8 mm/yr which results to be much smaller than the one on the Mediterranean Sea where effective evaporation sums up to 20 mm/yr. These normalized values are introduced primarily to facilitate a comparison between the two marine source regions. We acknowledge that they should not be interpreted as physically meaningful evaporation rates, since the actual moisture supply to the atmosphere is strongly controlled by episodic processes. In particular, large evaporative fluxes are often associated with strong large-scale ocean evaporation events (SLOEs), which typically occur in regions experiencing cold-air advection upstream of cyclone tracks [170]. Such events can produce intense but spatially and temporally localized evaporation bursts that are not fully captured by the simple normalization approach adopted here.

The majority of continental moisture originates from Europe, accounting for approximately 83.8% of the total land-based input. However, notable contributions also arrive from other continental regions, with north-west Africa supplying around 12.4% and north-east America contributing with a 3% share. Notably, a strong spatial inhomogeneity is again evident when moisture contributions are normalized over the respective source areas. Europe clearly dominates the continental sources, contributing 12 mm/yr, while Africa and north America follow with significantly lower values of 1.38 mm/yr and 0.48 mm/yr, respectively.

The assessed marine shares (oceanic and mediterranean) are in good accordance with the ones reported in the study by Sodemann and Zubler (2009). This study focused on the diagnoses of seasonal moisture sources for Alpine precipitation during 1995-2002 using the method of Sodemann and Zubler (2009) together with the Lagrangian tracing trajectory model of Wernli and Davies (1997). In contrast, some discrepancies arise in the estimates of continental contributions: while the current study attributes 37% of the precipitation to continental sources, Sodemann et al. (2008) states that only 20% derives from terrestrial evapotranspiration. Consequently, European shares are far from being similar as this study assessed a 31.6% share in contrast with the 16.2% by Sodemann and Zubler (2009). However, it is important to note that the relative importance of Europe on the land contribution stays constant between the two studies.

These differences can be attributed to several factors: (i) the two studies use different definitions of land, with the present work considering the entire globe, whereas Sodemann and Zubler (2009) focuses on a smaller region, (ii) continental evapotranspiration is known to vary significantly depending on time period analyzed and Sodemann and Zubler (2009) analyzed the shorter interval 1995–2001, while the current study examines 2008–2017, (iii) continental share consistency is a well-documented source of divergence across different moisture tracking models [90, 171]. Finally, (iv) the input data play a major role: the present study utilizes ERA5-Land, which includes a more advanced land surface model [165], providing a strong improvement over the ERA-Interim dataset used in the earlier study. In fact, our findings are in agreement with the refined Lagrangian moisture source diagnostics reported by Aemisegger et al. (2014), based on the high-resolution regional model COSMO (7 km grid spacing).

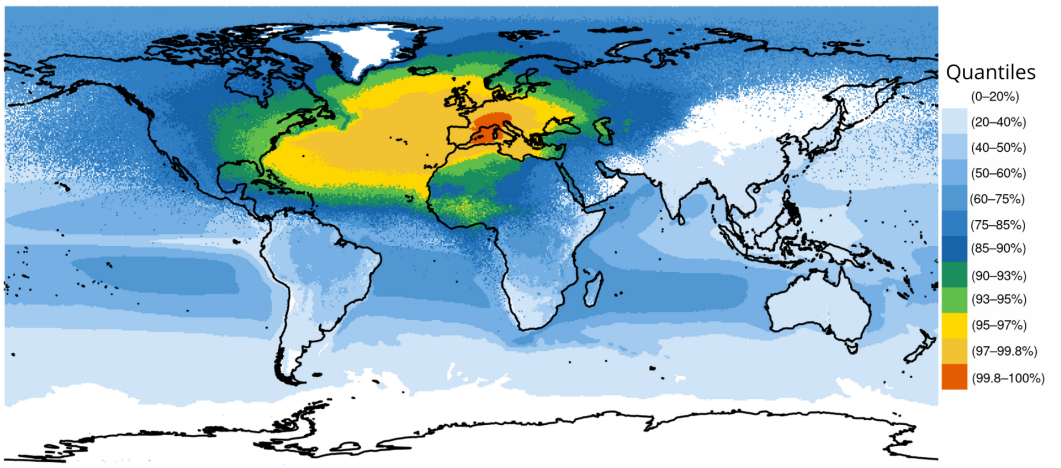

Fig. 3.7. Mean yearly evapotranspiration shed of precipitation on the Alps

Table 3.1. Mean yearly contributions to precipitation over the Alps

Contribution Source	[km^3]	[mm]	Relative Contribution [%]
Marine	180	-	62
North Atlantic Ocean	116	2.8	40.6
Mediterranean Sea	60	20	21.0
Continental	107	4.2	37.5
Europe	90.4	12	31.6 (83.8 of land)
Alps	28	y	8
North-West Africa	13.3	1.38	4.6 (12.4 of land)
North-East America	3.23	0.48	1.15 (3 of land)
Total	286	1505	100.0

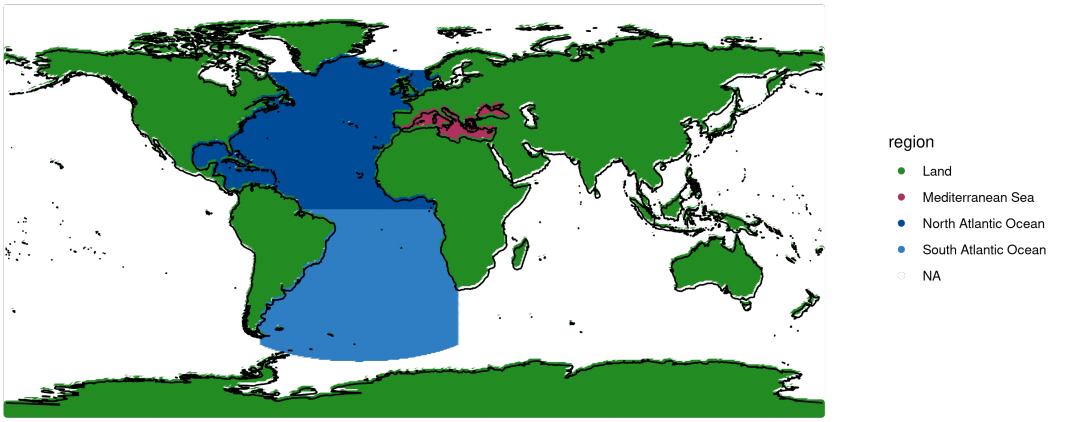

(a)

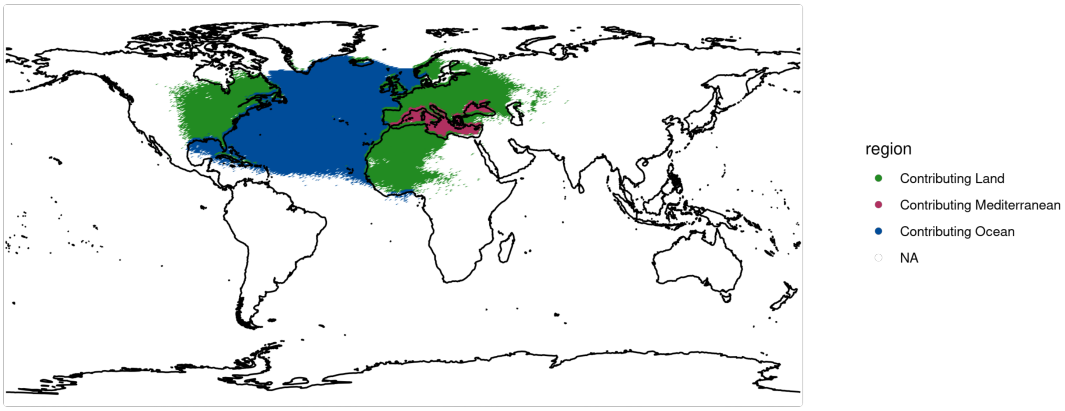

(b)

Fig. 3.8. (a) Definition of moisture source areas, (b) Areas contributing to 99% of Alpine precipitation

The Alps are well known for acting as a significant orographic barrier to atmospheric flow, deflecting wind trajectories and giving rise to distinct windward and leeward sides. These, typically, correspond to the northern (NA) and southern side (SA) of the mountain range, defined as described in Figure 3.4. This topographic effect is likely to influence the spatial distribution of moisture source contributions to precipitation on each side of the Alps. Figure 3.9 shows the upwind evapotranspiration sources of the northern (top pannel) and differences with respect to the southern side (bottom pannel) of the Alps. On an annual basis, NA receives a total of approximately 190 km^3 of atmospheric moisture in the form of precipitation, which represents a substantially larger absolute volume compared to the 92.4 km^3 received by SA. However, this asymmetry in total precipitation is due to the differing spatial extents

of the two regions. In fact, when normalized by are the relative extensions ($13.4 \cdot 10^5$ km^2 for NA and $5.6 \cdot 10^5$ km^2 for SA), the pattern reverses: the SA exhibits a higher average annual precipitation intensity of 1644 mm, while the NA receives a lower spatially averaged value of 1418 mm. Despite drawing moisture from broadly similar upwind source regions, the relative contributions for each source vary between the two sides. Figures 3.9a depicts the upwind moisture plume associated with the northern side of the Alps, shown at the global scale and restricted to the western Mediterranean Sea, respectively. Figures 3.9b illustrates the difference between the normalised plumes associated with the southern and northern sides. Blue pixels indicate grid cells that, in relative terms, contribute more moisture to the NA than to the SA, while red pixels indicate the opposite. Thus, it is visible how the NA plume extends over slightly higher latitudes than SA. As reported in Table 3.2, both sides align with the whole-arc-mean dependence on evaporation from marine contributions, receiving about 60% of the incoming precipitation from free water surface evaporation. However, the NA has a stronger incoming flux from the north Atlantic Ocean (42.5%) compared to the SA (36.6%). In contrast, the southern side is more strongly influenced by the Mediterranean Sea, which contributes for 26.7% of the moisture input versus 18.3% for the north. These different contributions align well with findings reported by [163] underscoring the role of the Alps not only as a climatic but also as a moisture source divide. It is also important to note that previous studies pointed out how this stronger dependence of the SA from Mediterranean moisture make it more prone to extreme events [163, 172, 173]. Moisture supply from the Mediterranean Sea is, in fact, less stable than the one coming from the Atlantic Ocean as its variability is highly seasonally dependent. The contribution from terrestrial evapotranspiration is more balanced between the two sides with 38.2% for the northern and 36.1% for the southern. However, it is evident from Figure 3.9b, that differences emerge in the specific local sources. For example, evapotranspiration from lowland areas north of the Alps and the Pyrenees mountain range influences the NA but has a smaller effect on the SA. In contrast, moisture from the Padana Plain provides tends to precipitate more on the southern side rather than on the northern one.

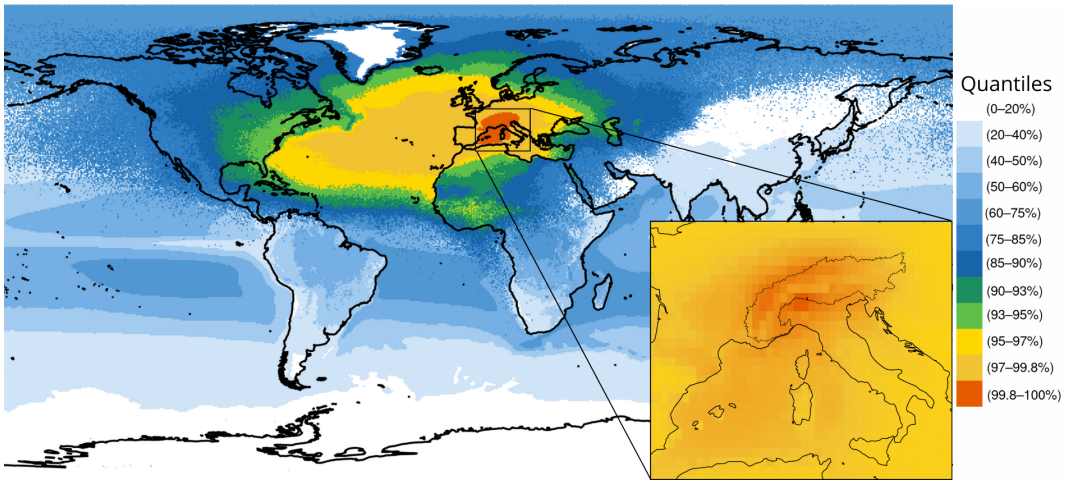

(a)

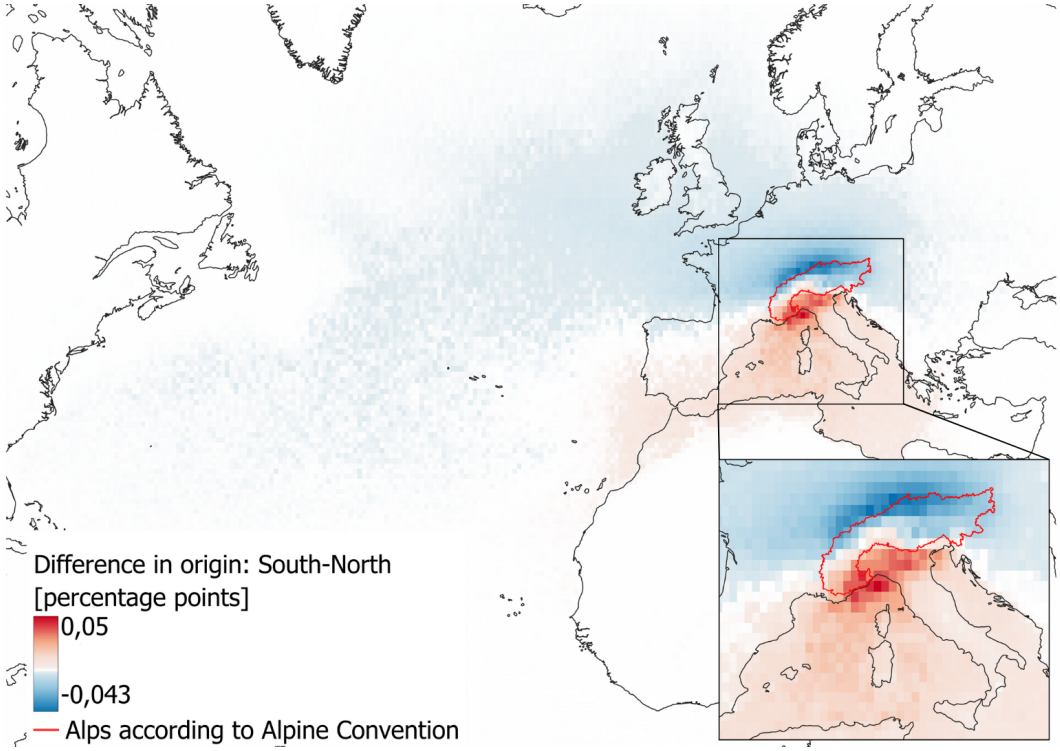

(b)

Fig. 3.9. (a) Precipitation shed for northern Alps, (b) difference of precipitation shed origin between southern and northern Alps expressed in percentual points. Blue cells contribute more, in relative terms, to the northern than to the southern side, red cells the opposite.

Table 3.2. Mean yearly contributions to precipitation over the northern and southern side of the Alps

Contribution Source	**North**	**South**
	[km^3] [%]	[km^3] [%]
North Atlantic Ocean	81.8 (42.5)	34.0 (36.6)
Mediterranean Sea	35.2 (18.3)	24.8 (26.7)
Land	73.5 (38.2)	33.6 (36.1)
Total	190.5 (100)	92.4 (100)

The complex topography of the region not only affects the wind flow trajectories and the moisture source contributions but highly affects the local climate. The orographic effect, in fact, induces variability in the precipitation of the transported moisture, causing highly local precipitation patterns.

Mean yearly precipitation maps of the Alps (Figure 3.10a) show strongly heterogenous spatial distribution characterised by steep gradients over relatively short distances. A comparison between the precipitation map (Figure 3.10a) and the corresponding topographic elevation map (Figure 3.10b) highlights a correlation between precipitation patterns and altitude but especially with orography. It is possible to see a correlation between precipitation and altitude (R^2=0.04), yet strong deviations from such pattern can be spotted: the most visible one is the strong precipitation sink over the area of Ticino and Lago Maggiore in the south-west. On the other hand, a clearer pattern is the one related to orography. In fact, higher precipitation levels are generally concentrated where the incoming humid air flows encounter ridges sufficiently high to force their uplift. When humid air is forced to uplift, it cools, causing moisture to condense and precipitate on the windward side. On the contrary, leeward regions, typically the inner-Alpine valleys, receive less precipitation due to rain shadow effects.

The spatial distribution of precipitation clearly reflects the influence of prevailing wind directions and orographic features. Most precipitation is concentrated on the windward slopes, in alignment with the two dominant wind patterns. Moist air masses from the north Atlantic are carried by the westerlies toward the northern outer arc of the Alps, delivering significant rainfall to regions such as the north-east Valais, the Bernese Oberland, and the Engadine in the Swiss Alps (for geographical references, refer to Figure 1.2). Similarly, southwesterly winds transport humid air from

the Mediterranean Sea, resulting in high precipitation levels over the Dolomites and the highest sections of the western Italian Alps, including the Gran Paradiso National Park and the Monte Rosa range. These preferential patterns also explain the markedly drier conditions found in the interior Alpine basins, which are shielded by surrounding high terrain, such as the Val d'Aosta in the Italian west Alps, Graubünden in central Switzerland, and Tirol in western Austria.

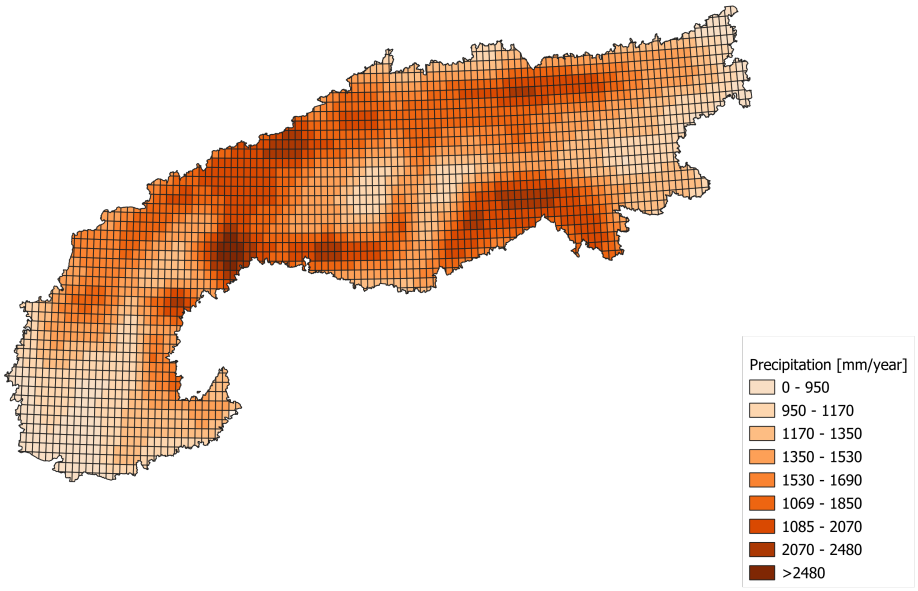

(a)

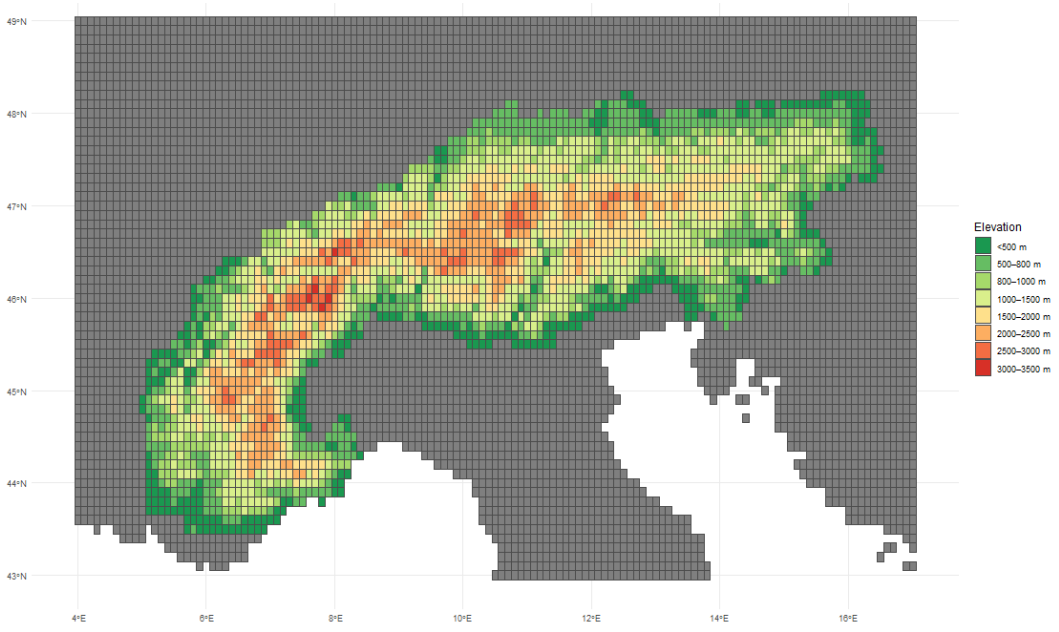

(b)

Fig. 3.10. (a) Mean yearly precipitation over the Alps in mm/yr, (b) Elevation pattern of the Alps. Both panels are at the ERA5-Land grid cell resolution of 0.1°

Outgoing evapotranspiration

The Alps not only receive water as precipitation and release it as stream flow, but also pump back to the atmosphere a large amount of the precipitation as moisture that is subsequently transported by winds and eventually precipitates. Evapotranspiration rate depends on the tradeoff between the effects of temperature, wind, air pressure, and solar radiation. Decreasing temperature results in a decrease in ET, while an increase in wind, a reduction in air pressure, and an increase in solar radiation increase evapotranspiration. However, depending on the environment, the relative importance of several factors and plant characteristics, ET response can vary from strongly decreasing to increasing, highlighting the diversity of plant water regulation strategies and the complexity of the phenomenon. Although a visual comparison between the mean annual evapotranspiration map of the Alps (Figure 3.11a) and the elevation map (Figure 3.10b) suggests a good ET–elevation correlation, the interplay between ET and surrounding environmental conditions leads to a non perfectly linear correlation. Nonetheless, Figure 3.11b shows a clear strong tendency for evapotranspiration to decrease with increasing elevation such that the correlation coefficient amounts to r= -0.84 (R^2=0.7). The locally weighted regression line blue in Figure 3.11b indicates that evapotranspiration decreases almost linearly from 700 mm/yr to 600 mm/yr within the 200–100 masl elevation band, typically found at the edges of the Alps where vegetation is dense. From 1000 to above 3000 masl, evapotranspiration declines more steeply from 600 mm/yr to less than 150 mm/yr. The passage between the two distinct patterns corresponds to the shift between two fundamental ecological zones in the Alps: broadleave forests and coniferous forests. On the Alps, 1000 masl corresponds to the line where conifers start to overtake broadleaved trees. Hereinafter, we use “evaporation” broadly to refer to all processes that transfer moisture to the atmosphere, including sublimation. Evaporation fluxes drop to few mm/yr only for very high altitudes where perennial snow and ice are found. In fact, the white spots in Figure 3.11a) correspond to the highest ranges on the Alps as, from left to right, Gran Paradiso, Mont Blanc, Monte Rosa, Piz Bernina, Otztal massive where only sublimation of snow and ice occurs. It is important to recall that these values are the result of interpolations and upscales at the ERA5-Land resolution (9 km) which is quite coarse given the complex alpine terrain.

Over the period 2008–2017, the mean annual volume of moisture evapotranspired from the Alps amounts to approximately 101 km^3 per year. This value is the sum of all evapotranspiration sources over the Alpine region. When distributed spatially over

the entire Alpine arc, the flux corresponds to an average of 540 mm of evaporation per year.

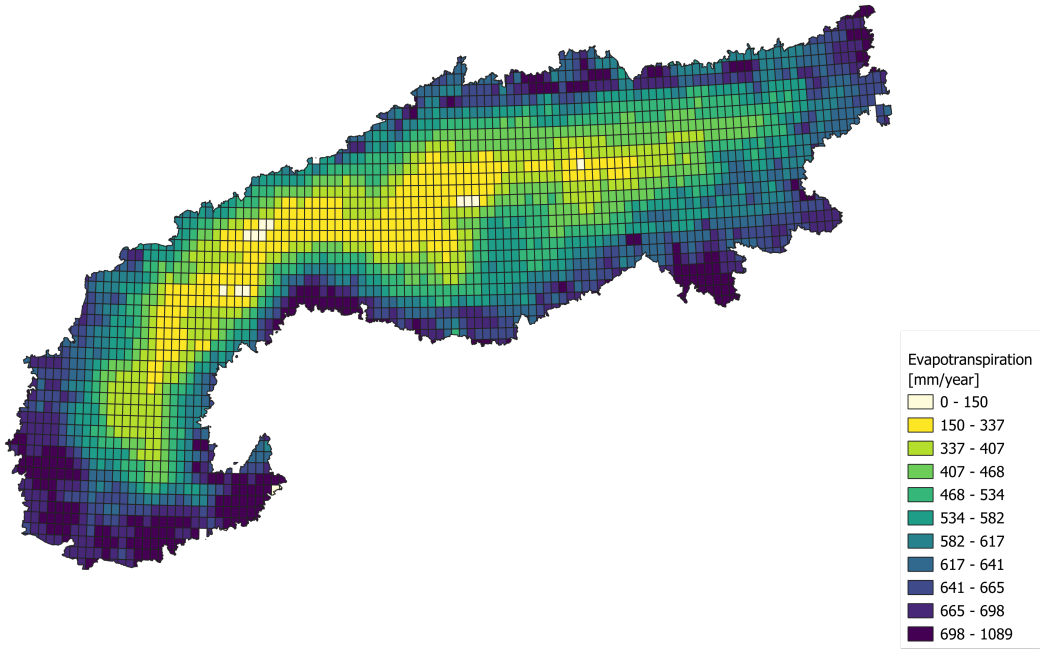

(a)

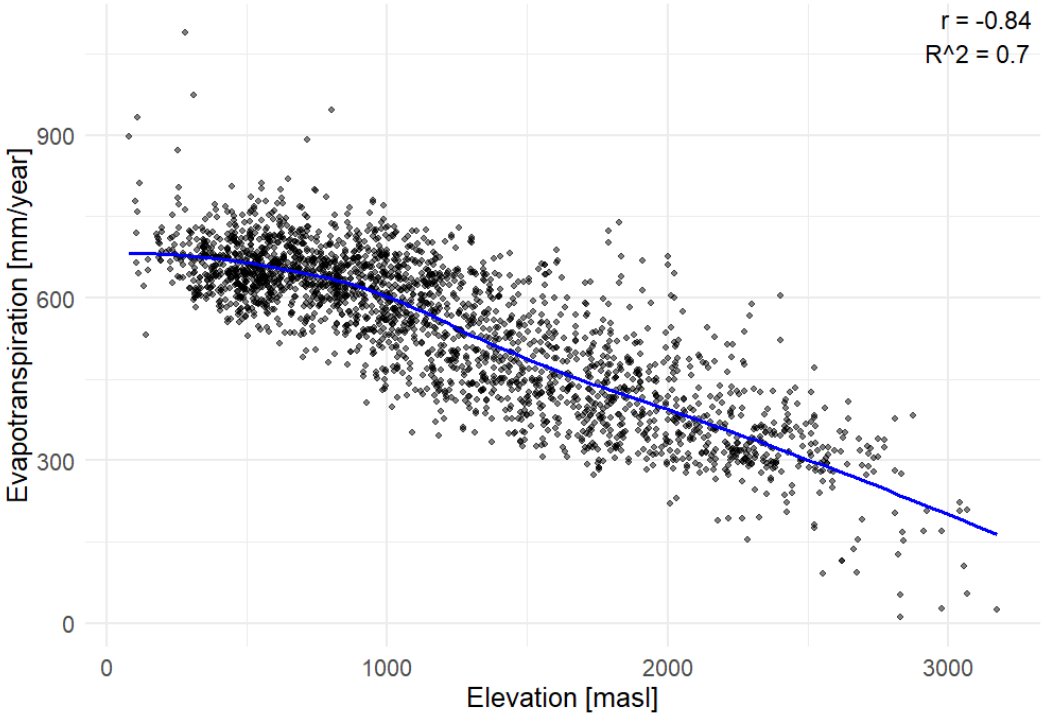

(b)

Fig. 3.11. (a) Mean yearly evapotranspiration on the Alps, (b) evapotranspiration in relation with altitude. The blue line represents the locally weighted regression.

As previously discussed, precipitation patterns are heavily modulated by orography, whereas evapotranspiration rates exhibit a strong dependence on elevation. This interplay results in a spatially heterogeneous water balance across the Alpine region. Figure 3.12 illustrates the spatial distribution of the Aridity Index (AI) across the Alps. AI, defined as the ratio between incoming precipitation and outgoing evapotranspiration, serves as a proxy for assessing the relative dryness or humidity of a given area. Although the majority of the Alpine domain falls within the "humid" classification according to the AI (AI>0.65), the variability in both precipitation and evapotranspiration fluxes is striking. On average, approximately 35% of the incoming precipitation is returned to the atmosphere via evapotranspiration. However, there are substantial regional deviations from this mean. For instance, southern regions such as Provence (France), which receives significantly less precipitation compared to the inner Alpine zones but are characterized by dense vegetation cover, exhibit notably high ET rates returning up to 70% of the received precipitation back to the atmosphere. Similarly, several valleys across the Alps display strong drier conditions compared to the surrounding highlands. Examples include Val di Susa, Val d'Aosta, and the Adige Valley in northern Italy; the Ticino Valley, Valais, and the Chur Rhine Valley in Switzerland; and the Inn Valley downstream of Innsbruck in Austria. These regions consistently show elevated ET-to-PR ratios, with ET accounting for at least 25% of the local precipitation, and reaching values as high as 50% in the Adige Valley.

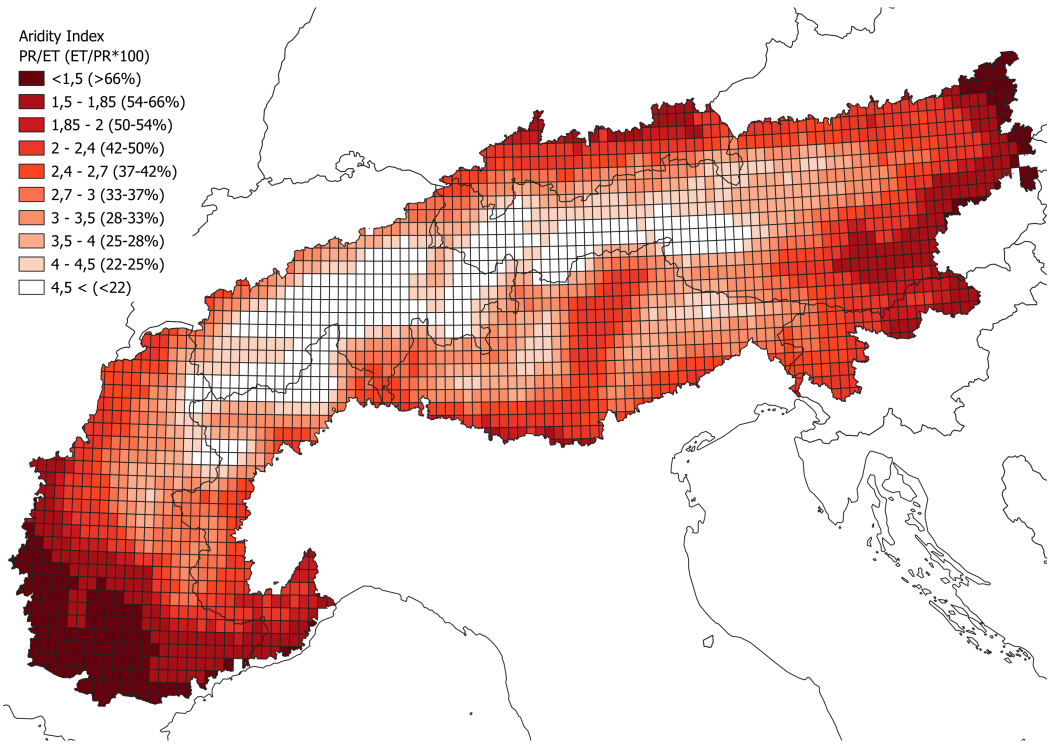

Fig. 3.12. Pattern of the mean aridity index (i.e., precipitation over evapotranspiration) in the Alps.

Thanks to the coupling of RECON and ERA5-Land, it was possible to define the mean yearly downwind plume of precipitation the Alps contribute to with its evapotranspiration (Figure 3.13). The colored area represents the mean annual Alpine evapotranspiration projected forward to the respective sink of precipitation, while the shading shows the contribution to the local precipitation of the evapotranspiration that occured on the Alps. Most of the sinks are located in the northern hemisphere, and Europe, Russia, the Mediterranean Sea, and the North Sea, stand out as the main collectors of Alpine precipitation contributions. In fact, these areas fall in the main downwind plume, from dark green to orange, that receives 99% of the moisture that evapotranspires from the Alps and finds its moisture sink maximum in easter Europe. It is important to note that a quantitative interpretation of the different zonal sinks (e.g., european, continental, marine) is not possible from Figure 3.13 as it does not take into account the areal extent of the moisture sources: the color scale accurately reflects the magnitude of the incoming flux for each grid cell; however, it does not permit a quantitative comparison of the relative importance of different sink regions, such as the Alps, Europe, and Russia. Analogously to the upwind plume, the shape

of the downwind moisture plume and the magnitude of local contributions reflect the variation between winter larger-scale geostrophic atmospheric circulation and summer more regional convective climatic processes. The westerly winds are the main responsible for the long-distance moisture transport from the Alps towards eastern Europe and Asia as well as for the reduced contributions to the Mediterranean Sea and the minor one to the north Atlantic Ocean.

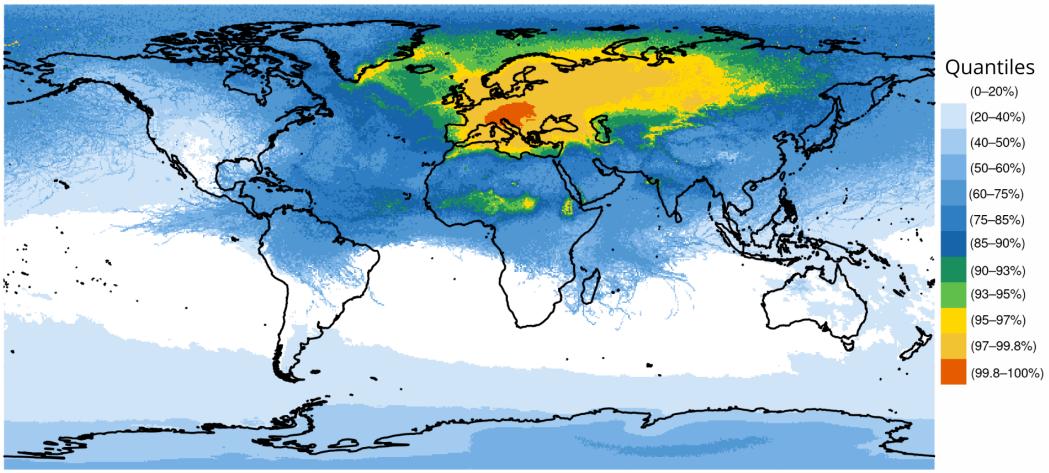

Fig. 3.13. Destination areas of 99% of Alpine evapotranspiration.

To quantify the contribution to different moisture sinks of Alpine evapotranspiration, the precipitation area was divided into two major macro-regions: continental and marine surface. To minimize the influence of minor or noisy sources and focus on the dominant contributors, only the regions receiving 99% of total Alpine evapotranspiration were considered. The resulting main receiving areas, highlighted in Figure 3.14, are Europe, Russia, the Mediterranean Sea, and the northern Sea. Although the north Atlantic Ocean was not identified as a major recipient of moisture evaporated from the Alps, the contribution to its precipitation was still analyzed to assess the imbalance between the moisture it supplies to the Alps and the moisture it receives back.

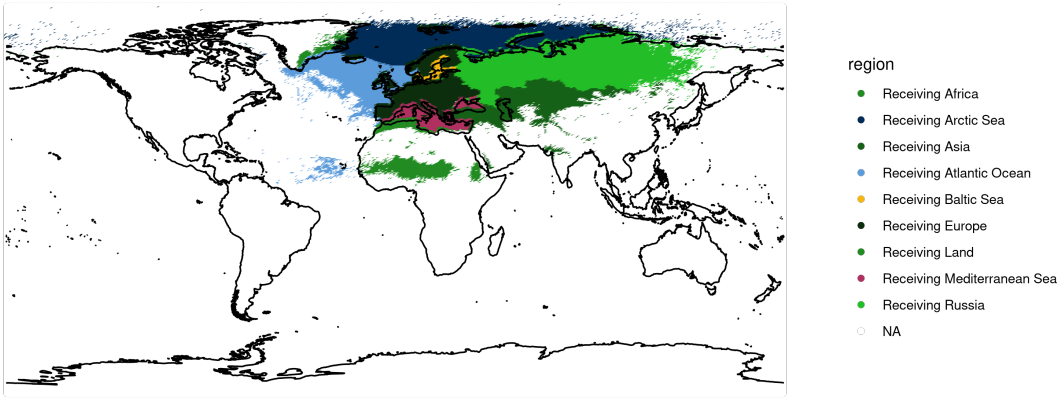

Fig. 3.14. Downwind plume from evapotranspiration on the Alps

Table 3.3. Year-averaged destination areas of evapotranspiration from the Alps. Note that Russia, geographically, mostly is in Asia but partially also in Europe.

Destination Sink	[km^3]	Relative Contribution [%]
Marine	14.8	14.7
Mediterranean Sea	5.29	5.24
Arctic Sea	4.25	4.21
North Atlantic Ocean	3.36	3.33
Baltic Sea	1.72	1.71
Continental	85.9	85.3
Europe	74.1	73.5 (86.1 of land)
Asia	10.1	10 (11.7 of land)
Russia	17.6	17.7 (21 of land)
North Africa	1.21	1.2 (2 of land)
Total	101	100

Table 3.3 lists the mean annual moisture sinks of Alpine evapotranspiration in the period 2008-2017, highlighting the prevalence of continental sinks. In fact, continental sinks account for 85.3% of the total Alpine evapotranspiration, while precipitation occurring over marine surfaces represents 14.7%. The majority of the moisture returning to land falls on Europe, which alone receives approximately 74 km^3 of water, corresponding to 73.5% of the total evapotranspiration and 86.1% of the land-sink output. The second main land sink is Asia, which receives 10% of the total evapotranspiration. A notable fraction of continental-sink moisture reaches

Russia, which alone receives 17.6% of the Alpine evapotranspiration. It should be noted that Russia extends across both Asia and Europe. Accordingly, the 17.7 km^3 of Alpine-sourced moisture received by Russia is shared between its European and Asian domains with a preponderance of the magnitude of the plume on the European side. Even though the north Atlantic Ocean provides the Alps with the largest amount of incoming moisture (116 km^3), as a collector the strongest marine connection is observed with the Mediterranean Sea, which receives 5.29 km^3 of Alpine moisture, equivalent to 35.6% of the total marine sink and 5.24% of the overall moisture output. The Arctic Sea can be identified as second marine collector of alpine moisture, receiving 4.25 km^3 that account for 28.6% of the marine sink and 4.21% of the total sinks. Minor sinks are also present in other regions: a small fraction of Alpine evapotranspiration is transported towards north Africa (especially Maghreb and Sahel regions), where 1.2% of alpine moisture contributes to local precipitation, and the Baltic Sea, that receives 1.7% of moisture. Comparing Table 3.1 and Table 3.3, it is notable the strong spatial and magnitude imbalance between the source of moisture that falls on the Alps and the sinks of moisture that are fed from the Alps. This "hopping" water source-sink supply chain is known to be one of the factors that can contribute to meteorological drought propagation [174, 175].

The northern and southern sides of the Alps both influence how atmospheric moisture moves across the region. As previously seen, the northern side tends to partially deflect the incoming flow from the Atlantic Ocean, while the southern side often acts as a barrier that Mediterranean moisture has to overcome before flowing northward. The respective roles of the northern and southern sides as sources of atmopsheric moisture contributing to both continental and marine sinks are illustrated in Figure 3.15 and Figure 3.16. The former illustrates the downwind plume on the northern side of the Alps, focusing on the nearest regions, whereas the latter depicts the relative difference in downwind contributions between the southern and northern sides—shown in red where the southern side contributes more (in relative terms) than the northern side, and in blue where the opposite is true. From both sides, a downwind moisture plume extends mainly toward the northeast, supplying water to the eastern Alps and the lowlands of eastern Europe. At the same time, the plume also stretches southward, reaching the Apennines in Italy and the western Balkan coast, highlighting how the Alps have an impact also on smaller distances. A notable example of this is the Pianura Padana which is visibly an important sink of Alpine Moisture, for the southern side plume. On a yearly average, the

northern side contributes approximately for 2/3 of the total alpine evapotranspiration, corresponding to a spatially averaged flux of 515 mm/yr, while the southern side, accounting for the remaining 1/3 has a stronger flux of around 560 mm/yr. Despite these differences in magnitude, both sides provide moisture to continental and marine sinks with similar shares (Table 3.4). However, a slight asymmetry can be observed: the southern side shows a stronger share in supplying marine sinks (15.3% for the southern versus 14.4% for the north), while the northern side exhibits a marginal predominance in supplying continental sinks (85.6% for the north versus 84.7% for the south). When focusing on the continental sinks, vapor originating on the southern side appear to travel shorter distances as its plume decays more rapidly than then one of the northern side. Quantitatively, southern moisture precipitates mainly within Europe (73.7%), with smaller fractions reaching Russia (15%) and Asia (8.89%). In comparison, the northern source demonstrates a slightly more gradual rain-out pattern, with 73.4% of its moisture deposited over Europe, 18.8% over Russia, and 10% extending as far as Asia. Moreover, the southward transport of moisture toward Africa is more pronounced for the southern side, which contributes 1.5% of its evapotranspiration to the African continent, compared with 1.1% from the northern side. The most pronounced difference, concerns the supply to the Mediterranean Basin. The southern side delivers a substantially higher fraction of their evapotranspired moisture (7.15%) to the Mediterranean Sea, while only 4.39% of the moisture from the northern slopes fall in that basin. Conversely, the Artic Sea and the Baltic Sea are slightly stronger sinks for the northern source region. In fact, the Artic Sea receives 4.6% of the northern moisture and only 3.25% of the southern. Similarly, the Baltic Sea receives about 1.8% of northern moisture compared with 1.4% from the southern side. These results mark, once again, the role of the Alps as a relevant obstacle for airflow in the atmospheric circulation and as factor shaping connections between different areas of the northern hemisphere.

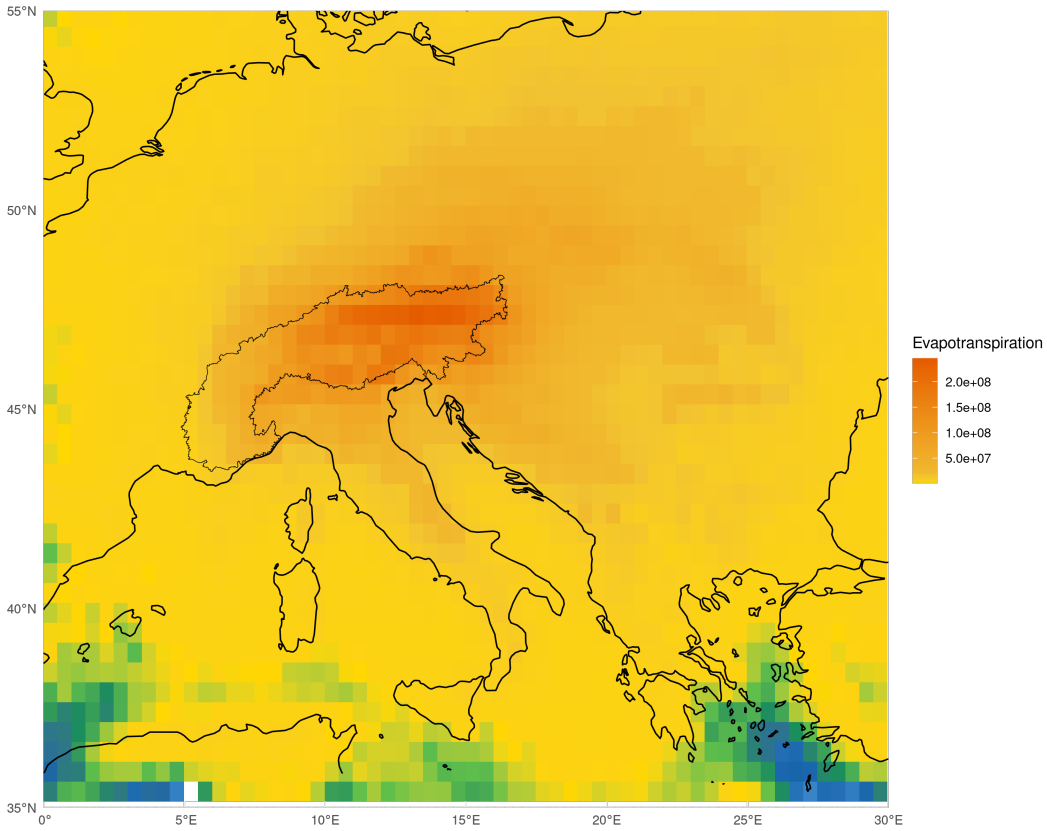

Fig. 3.15. Mean yearly destination of the evaporation from the northern side of the Alps

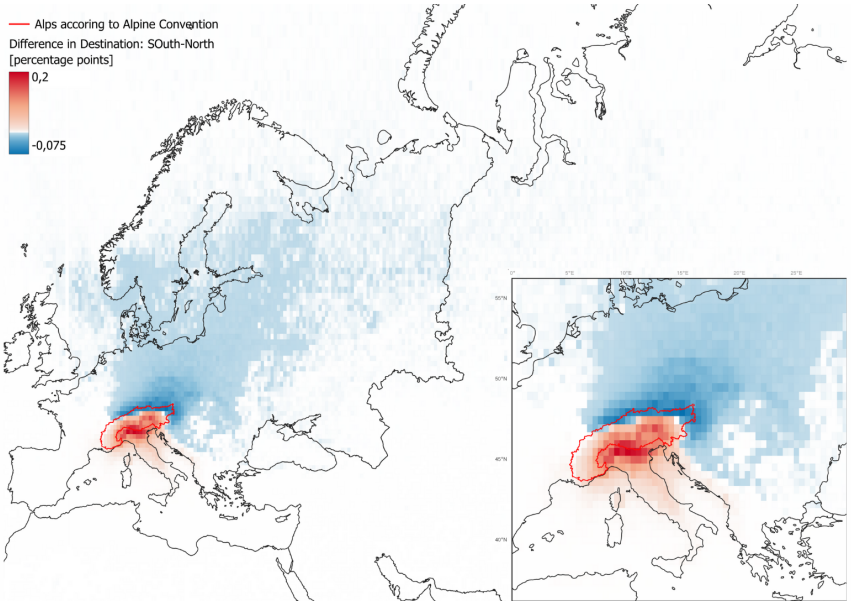

Fig. 3.16. Difference in downwind shed between southern and northern side of the Alps. In red where southern side(relatively) contributes more than the north, in blue where the northern side (relatively) contributes more than the south.

Table 3.4. Mean yearly destination of evapotranspiration from the northern and southern side of the Alps

Destination Sink	**North**	**south**
	[km^3] [%]	[km^3] [%]
Marine	9.86 (14.4)	4.79 (15.3)
Mediterranean Sea	3 (4.39)	2.24 (7.15)
Arctic Sea	3.18 (4.6)	1.02 (3.25)
North Atlantic Ocean	2.29 (3.34)	1.04 (3.32)
Baltic Sea	1.27 (1.8)	0.46 (1.4)
Land	58.6 (85.6)	26.5 (84.7)
Europe	50.4 (73.4)	23.1 (73.7)
Asia	7.24 (10.5)	2.78 (8.89)
Russia	12.9 (18.8)	4.68 (15)
Africa	0.75 (1.1)	0.47 (1.5)
Total	68.5 (100)	31.3 (100)

Alpine recycling

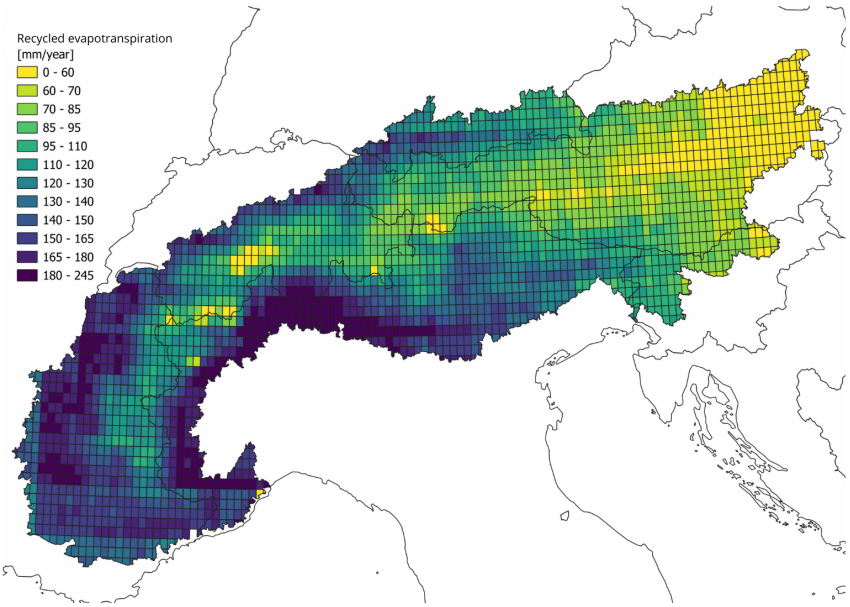

Fig. 3.17. Mean yearly alpine evapotranspiration that contributes to precipitation on the Alps

The Alps act as a source of precipitation not only for most of Europe but also for the mountain range itself. A significant portion of the moisture that evaporates or transpires from the region returns as precipitation, highlighting a strong internal recycling process. These recycling sources are unevenly distributed along the Alpine arc, with the largest contributions found on the western side (Figure 3.17), particularly across the mid-latitudes of the Italian and French sectors.

On average, the alpine recycled flux amounts to about 22.5 km^3 per year, representing 22.3% of the total annual evapotranspiration, 8% of the total incoming precipitation and 21% of the land-derived precipitation. The largest single contribution comes from the southern side of the Alps, which annually contributes with 8 km^3 to the Alpine recycle, accounting for 35.5% of the recycling flux. The western Alps, which comprise the French part and the Swiss canton of Valais, are the second contributor, accounting for 30% of the exchanged water flux with 6.8 km^3. The northern side, including west, center, and east zones, is strongly inhomogeneous and for this reason it was not accounted as a single contributor. However, the total volume of moisture leaving the northern side amounts to 14.5 km^3.

Figure 3.18a and Figure 3.18b show, respectively, the shares of total local evapotranspiration that contributes to Alpine precipitation and the shares of total local precipitation originating from the Alpine region. The shares resolution corresponds

to grid cells larger than those of ERA5-Land (0.1°) shown in the previous plots; this is because the shares depend on the spatial resolution of the RECON dataset (0.5°), as defined in Equation 3.2 and Equation 3.1.

From Figure 3.18a, it is visible how the evapotranspiration share strongly depends on topography. The highest shares of 30-38% (in dark blue) correspond in fact to the highest ranges of the west-southern west side of the Alps. Lower shares are found at lower elevations. However, while this is true for the west side, on the east side, the elevation gradient seems to be less relevant. The high Austrian ranges seem in fact not to share the same contributing effect of the french-swiss-italian ones. A reasonable explanation can be found in the fact that, while stronger geostrophic winds can bring moisture from west to east of the Alps, the convective processes for the Austrian Alps to contribute to themselves are not as effective.

From preliminary analysis, it resulted that local recycling expressed as precipitation due to evapotranspiration in the same cell is negligible because it accounts for less than 0.5mm for 75% of the cells. The recycled moisture returns to the Alps in a similarly uneven pattern (Figure 3.18b). In fact, while in France the alpine evapotranspiration contributes for a maximum of 4% of the mean annual precipitation, the eastern sector of the Alps experiences double of the contribution. Especially across Austria, more than 8.5% of total precipitation has alpine origin.

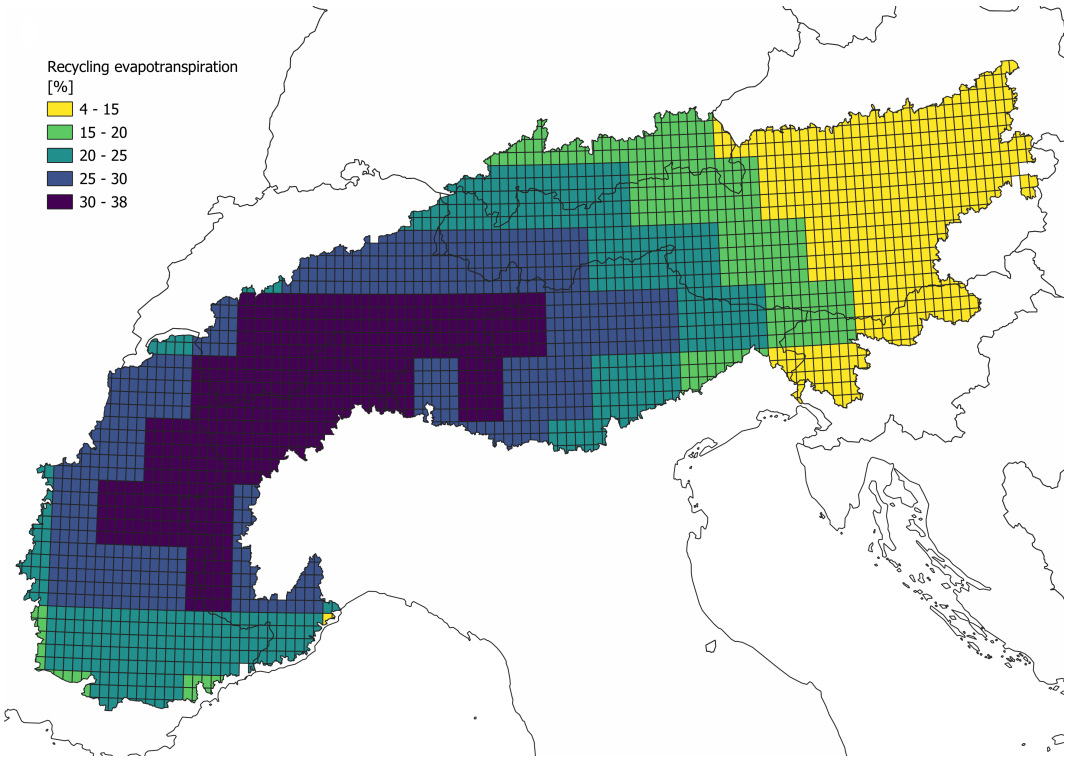

(a)

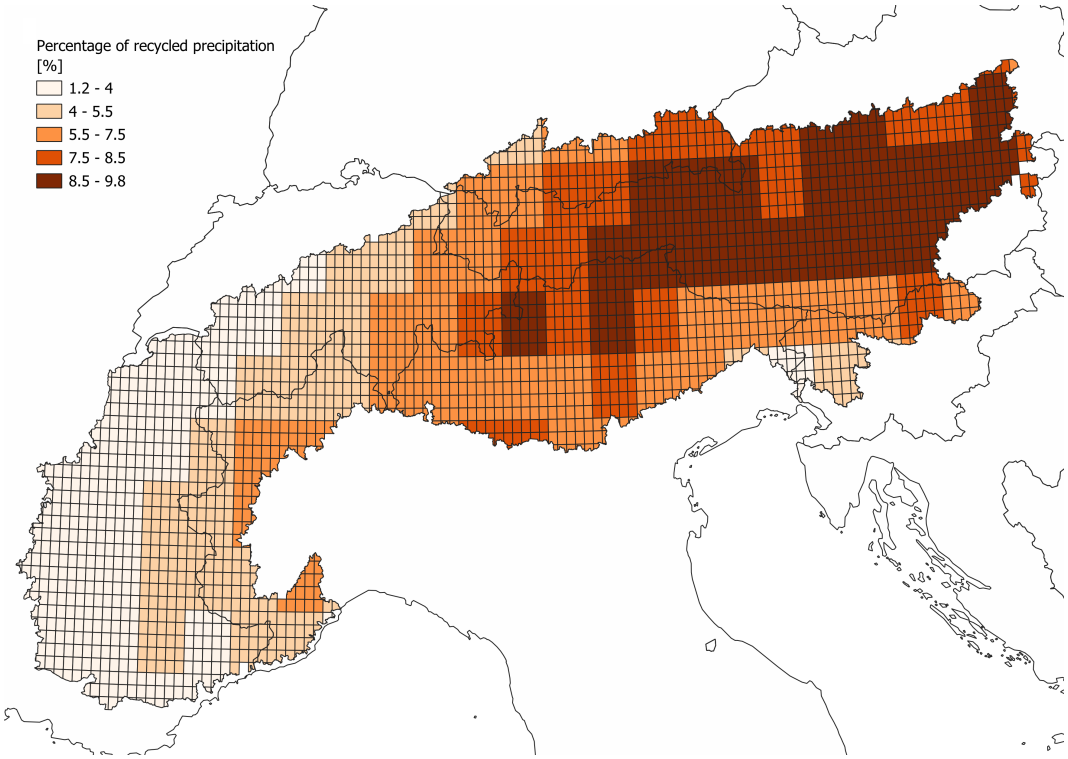

(b)

Fig. 3.18. (a) Mean yearly alpine percentage of evapotranspiration that contributes to alpine precipitation (b) Mean yearly alpine percentage of precipitation with alpine origin. Large cells in depend on RECON resolution (0.5°) while small cells in depend on ERA5-Land resolution (0.1°)

The imbalance between the western and eastern Alps in terms of moisture sources and sinks indicates a net transport of water vapor from the southwestern Alps toward the northeastern sector. The proportion of alpine evapotranspiration that contributes to alpine precipitation appears to be largely independent of latitude, displaying a mirrored pattern on either side of the main Alpine divide. However, when we also account for cross-side contributions—moisture from the northern slopes precipitating on the southern side and vice versa—important differences emerge.

Figure 3.19 illustrates this contrast. The upper panel shows evapotranspiration originating on the northern side that later precipitates in the south, while the lower panel depicts the opposite flow. In both cases, a marked spatial heterogeneity is evident. Northern evapotranspiration is dominated by contributions from the French Alps, followed by the Swiss Alps, with significant input from lower-elevation areas. The highest northern peaks contribute very little to precipitation on the southern side, whereas the highest southern peaks act as major recipients of moisture evaporated in the north. Notably, major summits near the French–Italian border (Gran Paradiso, Mont Blanc, Monte Rosa) receive almost no moisture from France despite their proximity; instead, downwind areas accumulate it. Additional moisture sinks are located farther east, particularly over the Orobie and Adamello ranges in central Italy and the Dolomites.

Figure 3.19b shows that evapotranspiration from the southern side is more uniformly distributed. Large contributions originate from the lower western Italian Alps and the Adige Valley, with a pronounced maximum of 150–180 mm/yr near the large lakes on the Swiss–Italian border (Ticino region). This moisture is then transported across the Alpine crest, where it precipitates mainly along the Germany–Austria border near Salzburg (100–110 mm), around Innsbruck (90–100 mm), and in the Hohe Tauern National Park (90–100 mm). The French Alps appear largely disconnected from this south-to-north moisture pathway, as the transport again follows a west–east trajectory.

Overall, the annual moisture exchange between the two sides is nearly balanced (Table 3.5): the northern Alps deliver more than 6.2 km^3 of water vapor to the southern and receive about 5.8 km^3 in return. Yet the spatially averaged local contributions differ substantially. On average, the northern side supplies about 47 mm/yr of moisture, whereas the southern side contributes roughly twice as much

(around 100 mm), consistent with the generally higher evapotranspiration rates observed on the southern slopes.

The recycling within each side amounts to a rough 2 km^3 for the southern and 8.3 km^3 for the north, corresponding to 2.16% and 4.4% of the total incoming precipitation and on each side, respectively.

Table 3.5. Mean yearly contributions to precipitation over the northern and southern side of the Alps, taking into account recycling fluxes

Contribution Source	**North**	**South**
	[km^3] [%]	[km^3] [%]
Land	73.5 (38.2)	33.6 (36.1)
Recycled	14.1 (7.4)	8.2 (8.9)
North	8.3 (4.4)	6.2 (6.7)
South	5.8 (3.0)	2.0 (2.2)
Total	190.5 (100)	92.4 (100)

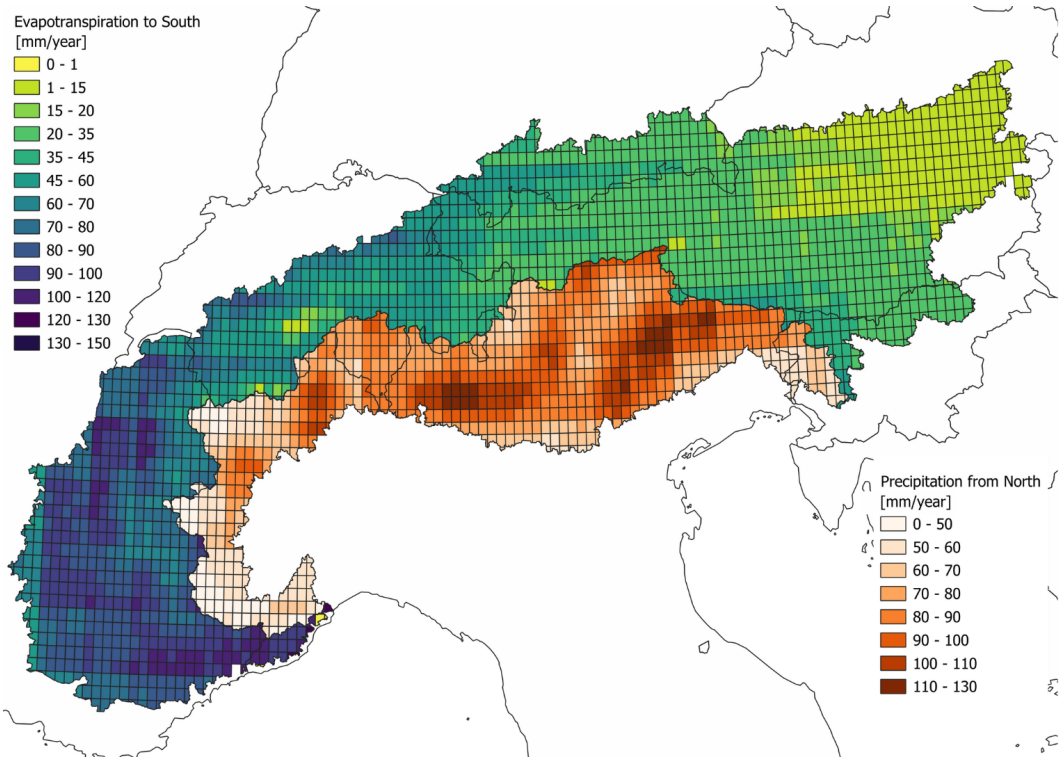

(a)

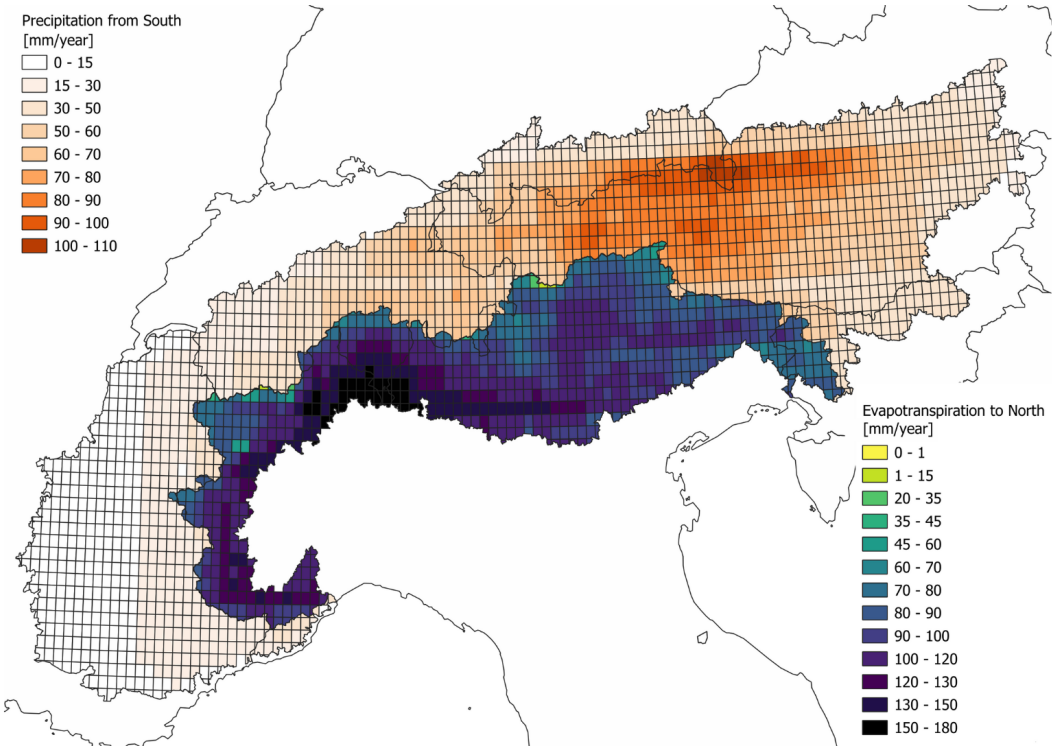

(b)

Fig. 3.19. (a) Mean yearly alpine northern evapotranspiration that contributes to southern alpine precipitation (b) Mean yearly alpine southern evapotranspiration that contributes to northern alpine precipitation.

3.2.2 Alps-agricultural land link

Moisture originating from the Alps, as seen in Figure **??**, mainly falls on Europe providing water not only to the Alps themselves but also to the lowlands. Lowlands include not only cities and woods but, importantly, cropland. The connection between the Alps and the downwind agricultural land through the atmosphere highlights the fundamental hydro-climatic role of the Alps in the European food production, not only in terms of river water but also as a precipitation supplier. One the most important areas strongly dependent for food production on the Alps on the riverine side, is the Pianura Padana (Section 1.1). This region, located in norhtern Italy is, in fact, watered by the Po River, the Adige River and their effluents, which mostly rely on water coming from the Alps. It is relevant to study the dependence of the Pianura Padana agricultural land from the Alps also in terms of precipitation.

For the period 2008-2017, on an yearly average, Pianura Padana receives 72 km^3 of rain.As visible in Figure 3.20, the precipitation distribution is highly not uniform. Generally, western Piemonte and northern Lombardia receive from 1000 to 1600 mm/yr while the drier central plain, around Milano, Cremona and Parma, receive 700-900 mm/yr. The Emilia-Romagna and Veneto region exibit a particular low rain income as they are located in a double rain-shadow area. For their position they are in fact on the leeward side of both Alps and Appenins that block mositure coming from the Atlantic and from the Tirrenean Sea respectively. This results in a cumulative precipitation of 600-800 mm/yr. Out of the 46'000 km^2, more than 30'000 km^2 of Pianura Padana are used for agricultural production (Section 3.1). on an annual average it receives 37.2 km^3 of rainwater. Figure 3.20 shows the spatial distribution of the rain patterns.

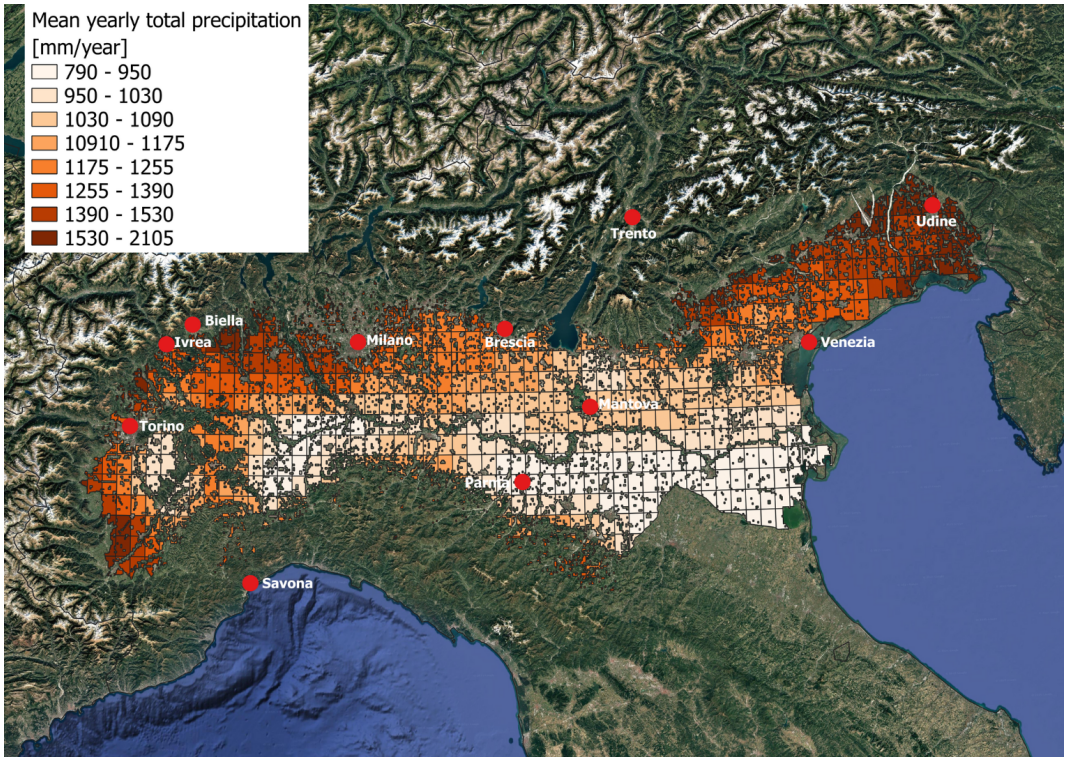

Fig. 3.20. Mean yearly precipitation over agricultural land in Pianura Padana according to ERA5-Land dataset

Origin of rainwater for Pianura Padana

Pianura Padana, located just up against the southern Alps, relies on a very similar evaporation shed strongly dependent on evaporation from Europe, Atlantic Ocean and Mediterranean Sea (Table 3.6). Marine moisture dominates the precipitation budget, contributing approximately 66% of the total annual rainfall, while the remaining 34% comes from continental sources. Among marine sources, the Atlantic Ocean plays a particularly important role, providing nearly 12 km^3 of precipitation annually, which corresponds to about 34% of the total. This contribution comes from large-scale atmospheric circulation that transports moisture from the ocean toward continental Europe. Close behind, the Mediterranean Sea is responsible for roughly 11.2 km^3 (around 32% of total precipitation). The Mediterranean contribution can be further broken down by sub-basins: The Adriatic Sea provides 1.1 km^3, equivalent to just over 3% of the total precipitation, while the Aegean–Levantine Sea contributes only 0.2 km^3, representing less than 1% of the total. The largest share of Mediterranean-derived moisture comes from the Tyrrhenian Sea and the western Mediterranean,

supplying 7.54 km^3, which accounts for 21% of total precipitation. The Ionian Sea and central Mediterranean add another 2.25 km^3, corresponding to roughly 6% of the total.

Together, these marine sources illustrate how the surrounding seas, particularly the western and central Mediterranean, are crucial in sustaining the Pianura Padana's rainfall, complementing moisture transported from the Atlantic Ocean. Continental sources, though smaller, also play a significant role, especially in the recycling of moisture over land. Overall, land-based sources contribute about 12 km^3 per year, making up roughly 34% of total precipitation. Most of this continental input comes from Europe, which provides 9.26 km^3, or about 26% of the total precipitation. A smaller fraction, 2.26 km^3, originates from Africa, accounting for around 6% of the total. Together, these land sources indicate that moisture transport from surrounding land is an important secondary source of rainfall, while African contributions, though smaller, are not negligible.

Table 3.6. Mean yearly origin of precipitation on Pianura Padana agricultural land

Contribution Source	**Agricultural Land** [km^3] [%]
Marine	23 (66.1)
North Atlantic Ocean	11.9 (33.9)
Mediterranean Sea	11.2 (31.6)
Adriatic Sea	1.1 (3.14) (9.9 of Mediterranean)
Aegean-Levantine Sea	0.2 (0.6) (1.9 of Mediterranean)
Tyrrhenian Sea and western Mediterranean Sea	7.54 (21) (68 of Mediterranean)
Ionian Sea and central Mediterranean Sea	2.25 (6.38) (20 of Mediterranean)
Land	12 (33.9)
Europe	9.26 (26.3) (77.5 of Land)
Africa	2.26 (6.43) (19 of Land)
Total	35.2 -

Alps as origin of rainwater for Pianura Padana

The Alps exert a major influence on the weather and climate patterns of the Pianura Padana through their strong barrier effect on atmospheric circulation. This orographic influence creates contrasting conditions across the region, producing rain shadow

effects in some areas while enhancing precipitation in others. Although this is the most evident and direct impact of the mountain range, it is not the only one. The Alps also act as a significant source of precipitation for the entire plain, contributing moisture that sustains its hydrological balance.

On average, about 6% of the total alpine evapotranspiration falls as precipitation over the Pianura Padana each year, with roughly 2% specifically reaching agricultural land (Figure 3.21a). These fluxes of roughly 6 and 2 km^3 from the Alps to Pianura Padana and agricultural land, , respectively, account on average for about 8 and 5% of the incoming precipitation. While these contributions may appear modest in absolute terms, they are comparable in magnitude to the atmospheric moisture fluxes originating from the Ionian Sea and north-west Africa (Table 3.6). This is remarkable considering that these marine and continental sources extend over areas two or more times larger than the Alps. Furthermore, the volume of precipitation with alpine origin is comparable to the 8 km^3 of maximum Snow Water Equivalent (SWE) accumulated over the southern Alps [176]. The SWE can be interpreted as the water storing capacity of the Alps. These 8 km^3 of SWE can be seen as the water that the souther Alps release downstream in the Po river in spring and summer and that the italian agricultural land relay on. It is noteworthy that agriculture in northern Italy requires, on average, approximately 8.1 km^3 of irrigation water [177].

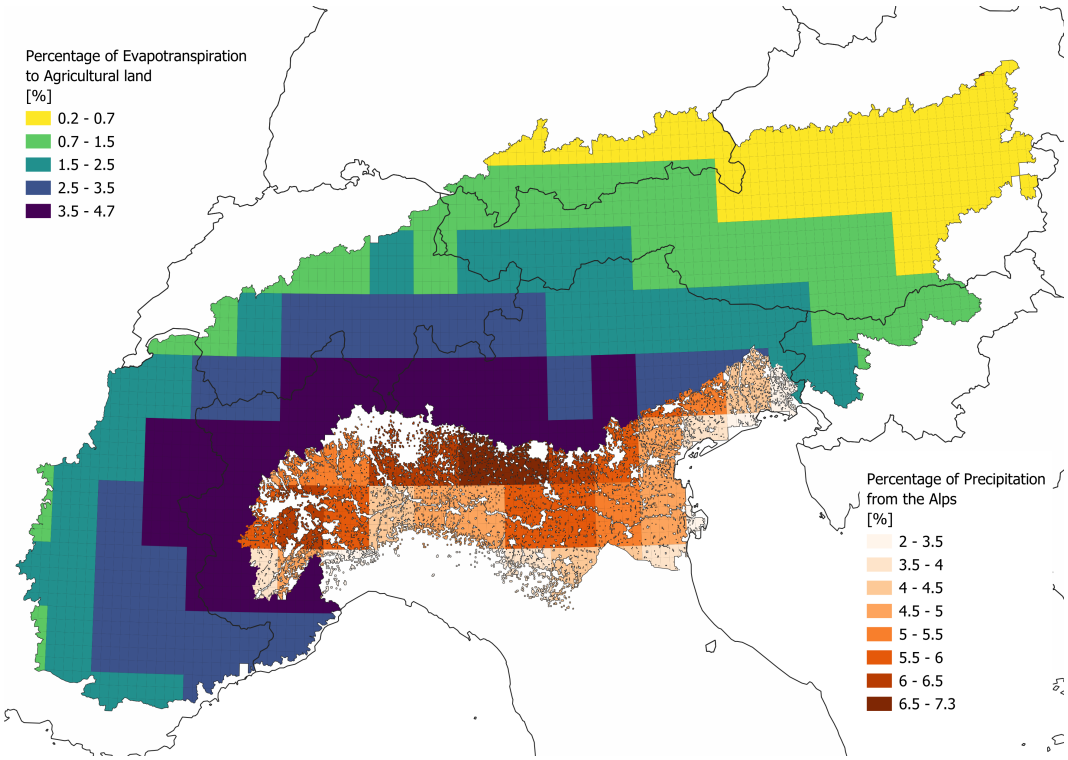

(a)

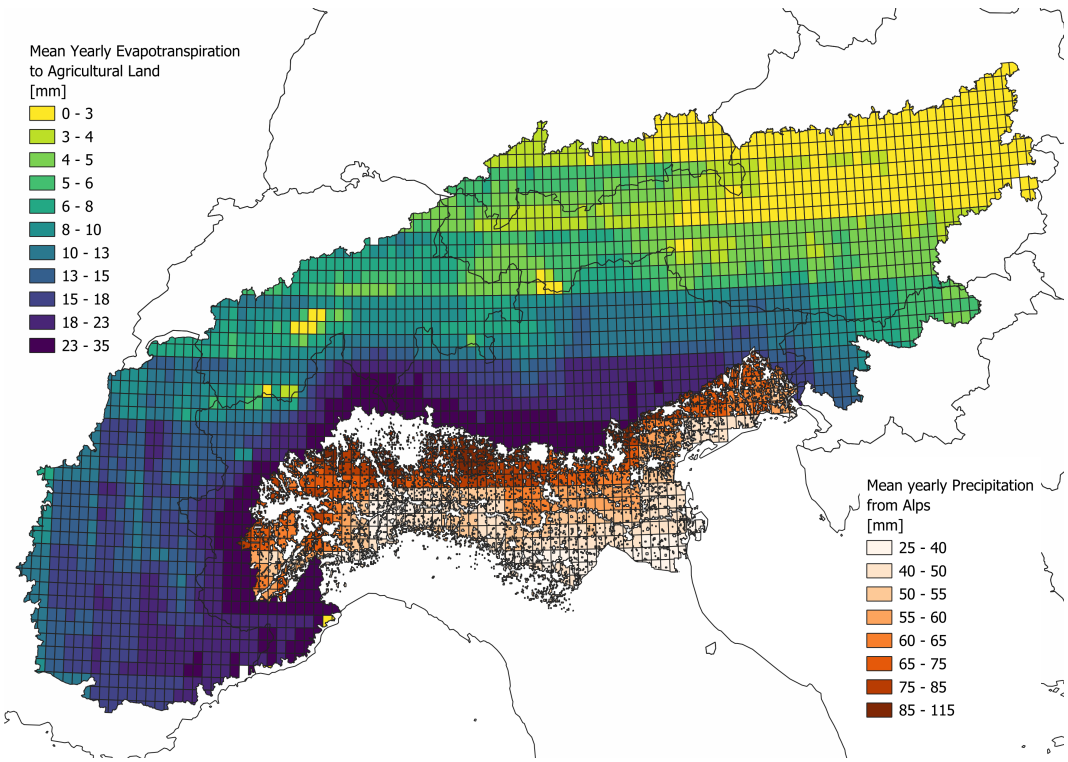

(b)

Fig. 3.21. (a) Mean yearly percentage of evapotranspiration from the Alps to agricultural land and of precipitation on agricultural land with alpine origin. (b) Mean yearly evapotranspiration-precipitation fluxes from the Alps to agricultural land in the Pianura Padana. Large cells in (a) depend on RECON resolution (0.5°) while small cells in (b) depend on ERA5-Land resolution (0.1°)

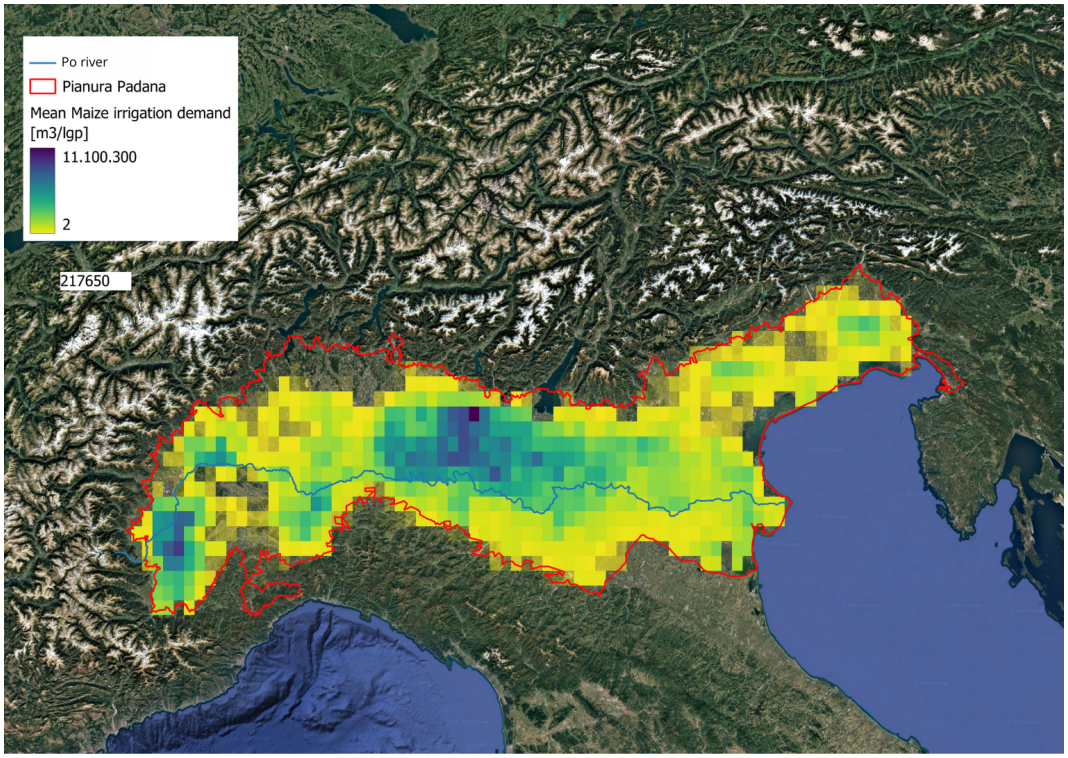

Fig. 3.22. Spatial distribution of mean maize irrigation demand (m^3) for the whole growing season (lgp) across Pianura Padana. The mean maize irrigation demand represents the water required on average by the maize cultivation according to WaterCROPv2.

For further comparison, the mean irrigation water demand for maize was evaluated in the Pianura Padana, as maize represents the second-largest source of irrigation demand in northern Italy, accounting for 19.7% of total irrigation abstractions [177]. Figure 3.22 shows the spatial distribution of maize irrigation demand as estimated using WaterCROPv2 with the configuration described in Section 2.1.2. Under this setup, WaterCROPv2 estimates an annual water use of approximately 1.2 km^3, which is in good agreement with official data reporting a total maize irrigation demand of 1.6 km^3 for northern Italy [140]. These results indicate that the Alpine region, despite its relatively limited spatial extent, supplies the agricultural lands of the Pianura Padana with a water flux comparable to the total irrigation requirements of maize cultivation across the entire region.

Both the sources of evapotranspiration and the areas receiving alpine-derived precipitation are far from being uniformly distributed. As visible in Figure 3.23b, the south central-western Alps emerge as the main atmospheric moisture contributors to precipitation over the agricultural land of the Pianura Padana. The most significant

receiving areas are concentrated around Torino in the west, between Milano and Brescia, and from Parma to Mantova in the central plain. In these regions, 5–7.3% of the mean annual precipitation can be traced back to alpine evapotranspiration, representing 15–20% of the precipitation originating from evapotranspiration over land. The central–eastern plain, usually drier and largely dependent on the Po River for irrigation, receives a significant portion of Alpine precipitation, highlighting its strong dependence on the Alps as a water source. In absolute terms the alpine incoming flux translates in a spatially averaged contribution of 66 mm/yr showing a concentration effect of the average 11 mm/yr of evaporation over the Alps.

From Figure 3.21a it is visible how the strength of the hydrological connection between agricultural land and the Alps varies noticeably from one area to another, even among neighboring grid cells without significant orographic barriers. This spatial variability suggests that short-range atmospheric processes, such as local convective circulation, play a key role in shaping the link between alpine evapotranspiration and plain precipitation – particularly during summer, when convective phenomena are more frequent and intense.

Figure 3.23 illustrates this dynamics by depicting the alpine evapotranspiration source areas associated with four distinct UTrack cells distributed across the Pianura Padana. A comparison between the top-left panel and the others reveals that proximity to the Alps significantly influences the spatial distribution of moisture sources. Areas closer to the mountains tend to exhibit more localized and intense moisture origins, whereas areas farther away receive moisture from spatially dispersed sources and influenced by broader atmospheric patterns.

Moreover, when comparing the top-right and bottom panels of Figure 3.23, it becomes evident that the geographic location of the target area determines the specific alpine sectors contributing most strongly to its precipitation. For example, agricultural land around Udine (top-right panel) shows a pronounced link to the Dolomites and Carnic Alps, indicating the importance of nearby eastern alpine ranges as moisture sources. In contrast, the areas surrounding Milano (bottom-left panel) and Biella (bottom-right panel) exhibit a closer connection to the western and southern Alpine sectors. Interestingly, even these two latter areas, which are geographically close and separated by no major orographic obstacles, demonstrate different source dependencies. Moisture contributing to precipitation around Milano is primarily associated with the Ticino region and the southern side of the Alps, whereas Biella,

despite the proximity, has a weaker link to Ticino and receives a larger share of moisture originating from the French side of the western Alps. This highlights the small-scale spatial heterogeneity of atmospheric moisture transport between the Alps and the Pianura Padana and the possible seasonal dependency. The linkage between the Alps and agricultural areas is believed to intensify markedly in summer, when enhanced evapotranspiration and convective activity amplify the Alpine moisture feedback. This makes the Alpine contribution particularly relevant for sustaining crop and pasture productivity during the dry phases of the growing season, when water demand peaks for most cereals and summer vegetables.

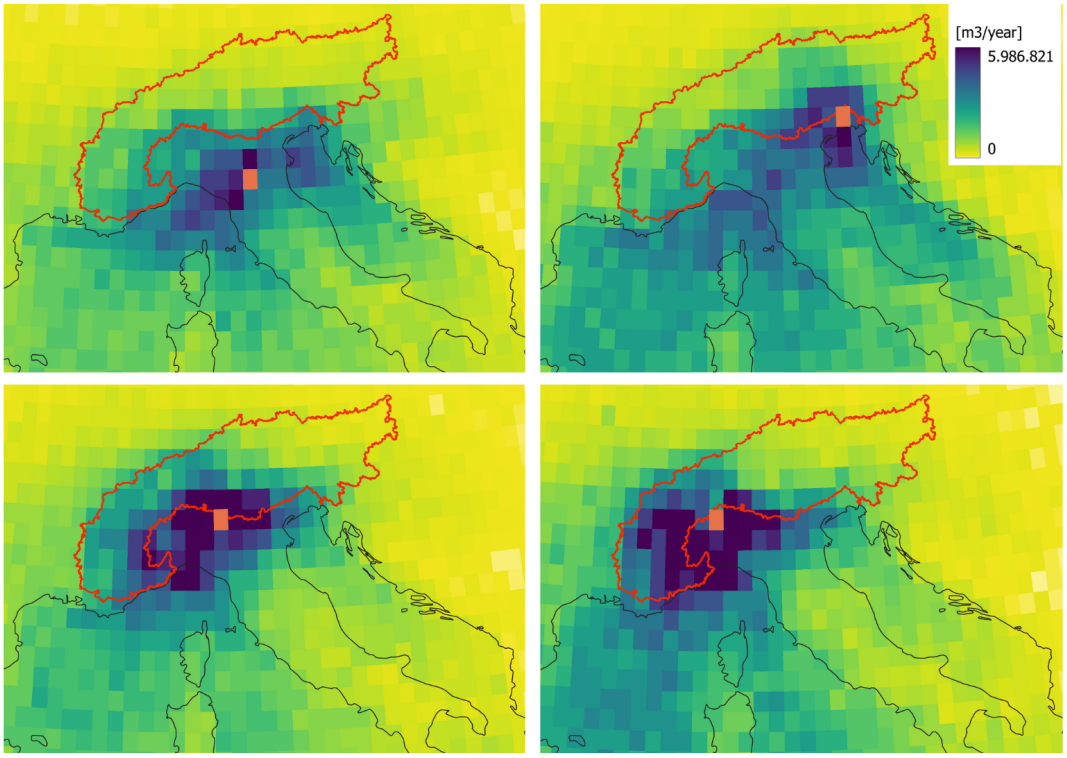

(a)

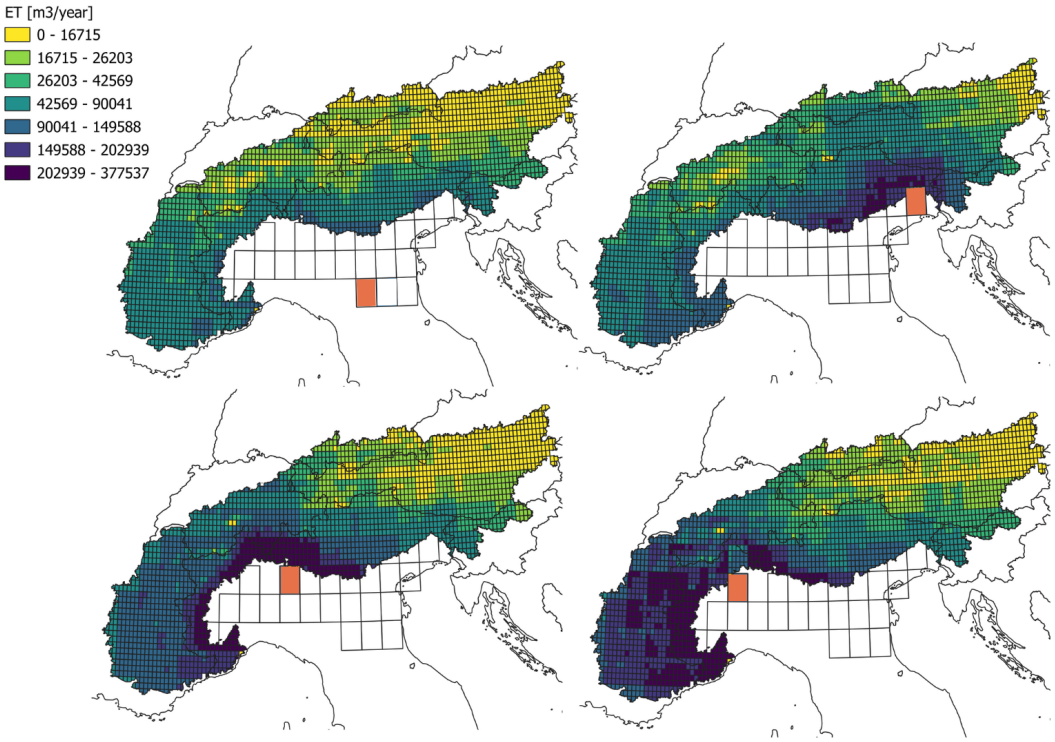

(b)

Fig. 3.23. (a)Upwind plumes of evapotranspiration, and (b) alpine evapotranspiration contributions to precipitation over specific agricultural land areas (orange cells).

The role of agricultural land as source of precipitation on the Alps

The agricultural land being vegetated for most of the period along the year when plants are not quiescent is strong source of evapotranspiration. As visible in Figure 3.24, the Pianura Padana agriculture sends moisture to the atmosphere in a very dishomogeneous way with peaks of mean yearly flux in the north-west and in the east. The former is in the area between the Ticino river and the Po river, where the cities of Vercelli and Novara are located, while the latter is the area from Mantova to the Po Delta, both famous for paddy fields for rice production. On average, 42.4 km^3 of moisture leaves the whole plain every year, with 50% having agricultural origin (22.4 km^3).

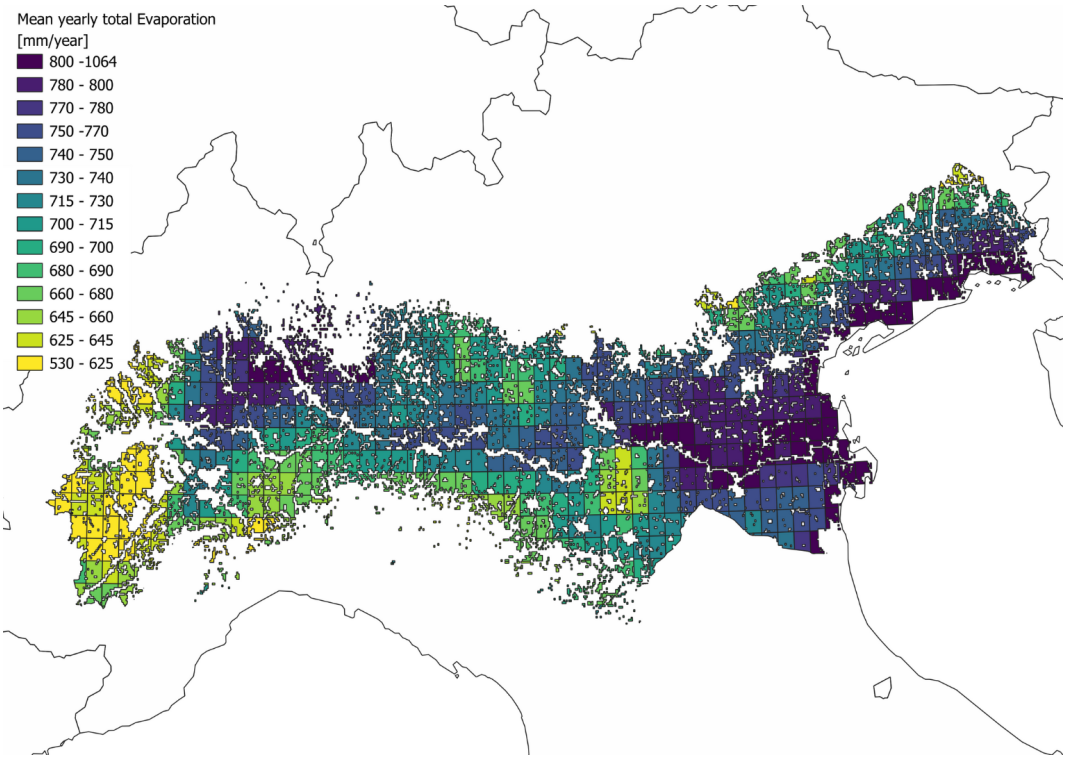

Fig. 3.24. Mean yearly evapotranspiration from agricultural land in Pianura Padana according to ERA5-Land dataset.

Figure 3.25a shows the spatial distribution of agricultural land evapotranspiration that sink as precipitation over the Alps and the spatial distribution of the latter. The top pannel shows the relative importance of the fluxes (ET and P) with respect to the total evapotranspiration from Pianura Padana and the total precipitation over the Alps, respectively. It is evident that a substantial fraction of the evapotranspiration

originating from the agricultural areas of the Pianura Padana is transported by atmospheric circulation toward the Alps. This signal is particularly strong in the western portion of the plain, which acts as a key moisture source for the central–southern Alps. These regions receive approximately 17–20% of the outgoing moisture from the western agricultural sector, corresponding to a contribution of roughly 1.7–2.6% to local precipitation totals.

Overall, however, the net contribution of agricultural evapotranspiration to Alpine precipitation remains modest when distributed across the entire mountain range. The total incoming flux of about 3.73 km^3 is spread over a vast and topographically complex area, resulting in an average contribution of only 1.2% to Alpine precipitation. When the entire Pianura Padana is considered as a source region, the total inflow exceeds 7 km^3, effectively doubling the contribution. This volume is larger than the flux imported from north America but of comparable magnitude (Table 3.1). In relative terms, it represents approximately 8% of all Europe-derived precipitation over the Alps.

The spatial pattern in Figure 3.25b highlights the areas that benefit most from agricultural evapotranspiration. These include the Orobie and Adamello ranges in the central southern Alps, as well as the Dolomites farther east. The distribution reflects the superposition of large-scale eastward moisture transport with smaller-scale orographic and mesoscale processes, which enhance moisture delivery to nearby regions.

When these results are compared to the Alpine moisture-export patterns toward agricultural areas (Figure 3.21), it becomes evident that on local scales the outgoing and incoming fluxes do not fully balance. Instead, the only clear source–sink match occurs on the western agricultural land which is both the sink of western Alps evapotranspiration and the source of central Alps precipitation. This creates a form of “moisture hopping connection" within the Alpine system, where deficits arising in the western Alps have the potential to propagate downwind toward the central Alps via the Piemonte region. Such a structure suggests a vulnerability in which localized drying or land-use changes on agricultural land may influence moisture availability and precipitation over more distant Alpine areas.

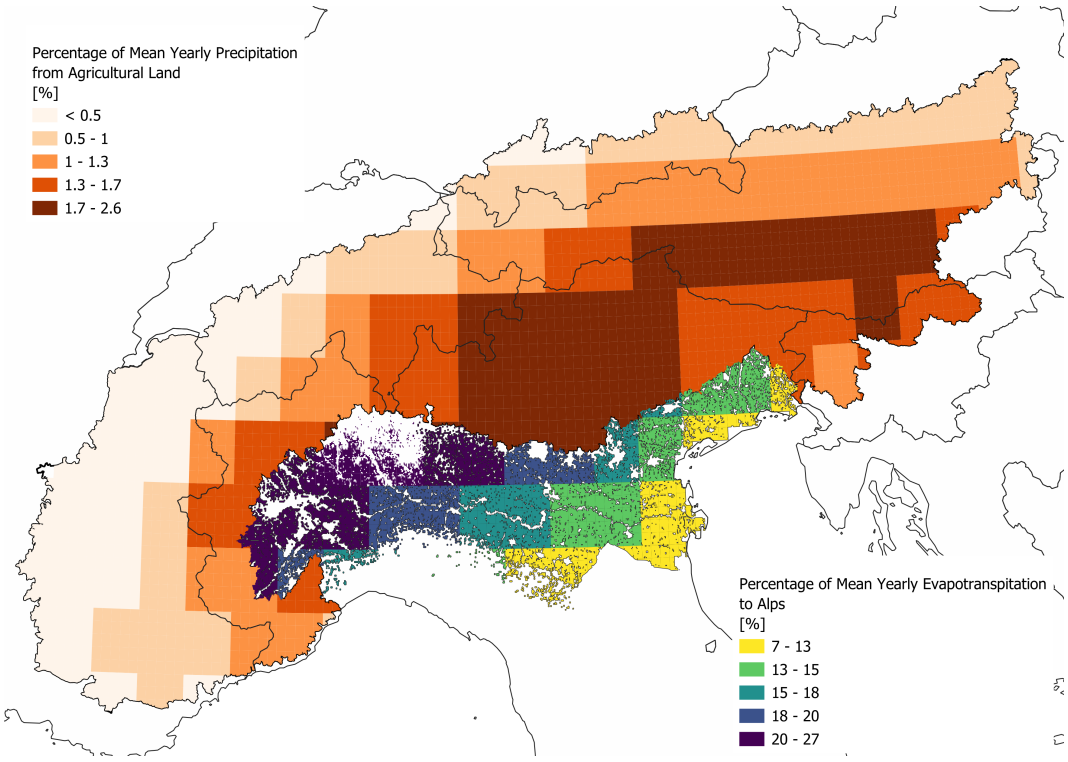

(a)

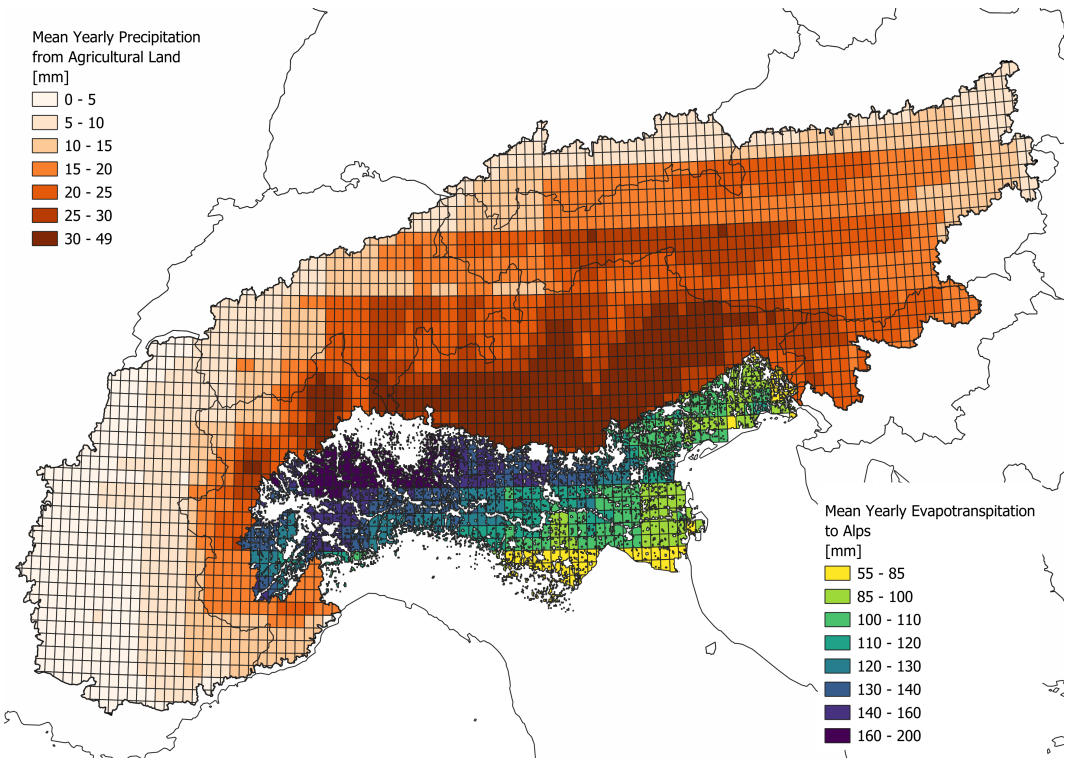

(b)

Fig. 3.25. (a) Mean yearly percentage of evapotranspiration from agricultural land to Alps and of precipitation on the Alps with alpine origin, (b) Mean yearly evapotranspiration-precipitation fluxes from agricultural land in the Pianura Padana plain to the Alps. Large cells in (a) depend on RECON resolution (0.5°) while small cells in (b) depend on ERA5-Land resolution (0.1°)

3.3 Conclusions

The Alps play an important role in the European hydrological cycle, not only as riverine water reservoirs but also as a major sink for atmospheric moisture transported from distant oceanic and continental regions, and an important source of evapotranspired water that sustains precipitation downwind. By coupling RECON with ERA5-Land, this study has quantified the atmospheric bidirectional fluxes, presenting the Alps as an active participant in atmospheric moisture redistribution rather than a passive recipient of rainfall.

On the incoming side, we showed that the Alps receive 286 km^3 of moisture per year, largely supplied by the north Atlantic (40.6%), Mediterranean Sea (21%), and European land surfaces (31.6%). Orography causes the incoming vapor to have highly uneven precipitation patterns, concentrating rainfall on windward slopes and leaving interior valleys comparatively dry. The contrast between the northern and southern sides of the Alps illustrates this duality clearly: while both receive substantial moisture from marine sources, the northern side is more strongly linked to the Atlantic Ocean while the southern side to the Mediterranean Sea. The latter connection results in the southern side being more exposed to climatic variability and a tendency to experience intense precipitation events.

On the outgoing side, evapotranspiration from the Alps amounts to roughly 101 km^3 per year, corresponding to one third of the incoming precipitation. Specifically, 85% of it precipitates again over continental Europe, and only 15% over the seas. This demonstrates a strong link between land and Alpine moisture, with Europe alone receiving 74 km^3 of Alpine-sourced water, and a significant share reaching as far as Russia (17.6%) and Asia (10%). At the same time, approximately 22.5 km^3 of this outgoing moisture returns directly to the Alps, providing up to 9.8% of local total precipitation. More specifically, the western Alps mainly provide water to the eastern Alps in an uneven pattern of evapotranspiration and precipitation. Furthermore, although the total exchange is nearly balanced between the northern and southern sides, the southern slopes contribute more moisture per unit area because of their higher evapotranspiration rates.

The asymmetry between the origin and destination of atmospheric moisture reveals a “hopping” pattern of source–sink interactions in which the Alps receive moisture from regions they do not supply with water in return. Such imbalances are known to

play a role in the propagation of meteorological droughts [174, 175], underscoring the need to consider long-range atmospheric moisture pathways when assessing water security in Europe.

The atmospheric coupling between the Alps and the Pianura Padana emerges as particularly significant. Although the plain receives most of its rainfall from marine sources, Alpine evapotranspiration contributes from 2% up to 7% of local precipitation and roughly 5% over agricultural land on average. Remarkably, the magnitude of this Alpine-derived precipitation is comparable to that imported from some Mediterranean sub-basins despite the Alps' much smaller spatial extent and to the whole maize irrigation demand in Pianura Padana. In reverse, evapotranspiration from the agricultural land of the Pianura Padana also contributes moisture back to the Alps but with modest amounts. The strongest signals arise in the western plain, areas that supply moisture to the central southern Alps.

Taken together, these results showed the role of the Alps in the large and small-scale atmospheric water transport. Their dual function as water towers and water source reinforces their critical role in sustaining European agriculture, and water resources. At the same time, the strong spatial variability and asymmetry in source–sink relationships highlight potential vulnerabilities. Changes in land use, irrigation intensity, or atmospheric circulation may propagate across this network, influencing precipitation patterns far from their point of origin. In fact, by quantifying both the incoming and outgoing fluxes, our analysis reveals that hydrological dependencies extend far beyond catchment boundaries: precipitation over the Alps depends on remote marine basins, while Alpine evapotranspiration provides downwind moisture that supports Italian and European agriculture. Understanding these pathways is therefore essential for anticipating regional water shortages, assessing the resilience of food production systems, and interpreting how climatic anomalies in one region may influence hydrological conditions elsewhere. By explicitly mapping these source–sink relationships, this study provides a framework that can support climate adaptation efforts, and guide integrated water-resource strategies that acknowledge the atmospheric linkages binding the Alps to the rest of Europe.

Chapter 4

Field and Lab activities

This section describes the field and laboratory activities carried out during a visiting period at the University of Bern, with the aim of gaining direct experience regarding *in situ* measurements, assessing their uncertainty, and comparing modelling results with direct observations. In particular, this section presents the activities conducted within a pilot project developed through a collaborative effort among the Hydrology and the Organic Micropollutants research groups. The primary objective of the project is to identify the origin of pesticides and PFAS previously detected in the SteinWasser streamflow.

The SteinWasser stream originates from the Steingletscher glacier and flows into the Aare River, one of Switzerland's longest rivers and a major tributary of the Rhine. Beyond its hydrological relevance, the stream serves as a long-term study site for the University of Bern and has been, and continues to be, monitored for pollutants, stable isotopes, electrical conductivity, temperature, and discharge. The past detection of pesticides and PFAS in its waters had raised an unresolved question regarding their source. While the use of passive samplers had allowed the identification of the presence of pollutants, now the discharge measurements aimed at improving pollutant quantification and glacier surface sampling at assessing whether these substances originated from the surface of the upstream Steingletscher glacier. Addressing this question is crucial for determining whether the detected contaminants in the water represent past pollution persisting in the ice or ongoing arrivals. The presence of banned pesticides on the glacier surface would suggest that these compounds persist in the atmosphere and are still transported to high-altitude Alpine environments,

polluting headwaters. To test this hypothesis, surface snow and ice samples were collected from the top layer of the Steingletscher.

Accordingly, Section 4.1 describes the activities carried out along the SteinWasser stream to measure discharge and perform laboratory uncertainty analyses, while Section 4.2 details the sampling campaign conducted on the Steingletscher glacier to collect snow and ice samples.

(a)

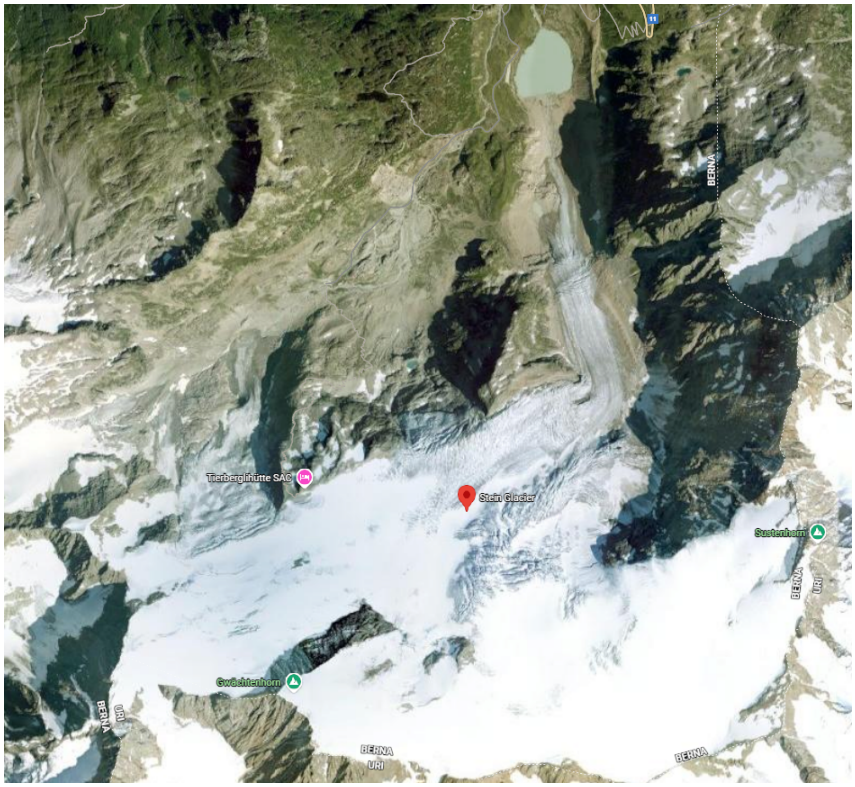

(b)

Fig. 4.1. (a) Location and (b) satellite view of Steingletscher system (Steingletscher glacier, SteinWasser streamflow, and SteinSee lake)

4.1 SteinWasser discharge estimation and lab uncertainty analysis

In situ estimation of river discharge is a key process in hydrological investigations, particularly in glacierized catchments where flow conditions are highly variable and strongly influenced by melt processes and meteorological forcing. In the SteinWasser stream, discharge measurements are performed at the same location where passive samplers for organic pollutants are located. Passive sampling techniques provide time-integrated concentrations of persistent organic pollutants and PFAS; their interpretation depends on the knowledge of streamflow conditions during the exposure period. Discharge data are therefore required to define pollutant loads and run comparisons between chemical concentration and hydrological variability.

In mountain streams, and particularly in glacier-fed systems, traditional velocity–area discharge measurements are often difficult to apply due to irregular and unsteady geometries. Tracer dilution methods offer an alternative under such conditions and are widely applied in alpine hydrology. Among these, the salt slug method is commonly used because it is cheap, simple, and environmentally safe when applied at appropriate concentrations. The method is based on injecting a known mass of salt into the stream and measuring the electrical conductivity downstream. Under well-mixed conditions, the dilution of the tracer is directly related to the discharge, allowing flow rates to be estimated without detailed stream geometry information.

This section presents the application of the salt slug method to estimate SteinWasser discharge at the location of passive pollutant samplers. Furthermore, we report here the activities carried out to study the sensitivity of the salt slug method to calibration temperature and probe positioning.

4.1.1 River discharge estimation through salt slug method

One of the most commonly applied method to evaluate river discharge is the gauging method by tracer dilution. This method is based on the injection of a tracer into the streamflow and on measuring its concentration in time. The measurement is run downstream the injection point at a distance sufficient to ensure good mixing across the cross-section so that the dilution of the tracer is a function of flow rate and does not depend on the location of the measurement. Most often the tracer is cooking salt

as it is cheap, easy to find, harmless to the river ecosystems for the concentration used, and its concentration is easily retrievable from conductivity measurements. A linear relationship exists between incremental salinity, S, and conductivity, EC:

$$EC(t) = kS(t) + EC_0 \tag{4.1}$$

assuming EC_0 to be the base electrical conductivity of river water and k a calibration coefficient. The calibration coefficient is not constant but strongly depends on the temperature of the water.

The mass M of salt injected disperses downstream in a cloud of salty water according a fluid dynamical process called longitudinal dispersion, due to the inhomogeneous velocity profile across the stream cross-section. The passage of the salt cloud is detectable from the fact that electrical conductivity increases from the base conductivity, EC_0, that represents the base salinity, S_0, of the river water, to a peak value and then declines back to EC_0. The longitudinal dispersion reduces the peak values the further the cloud moves downstream. The time required for the peak to arrive at the measuring point is inversely related to the velocity of the streamflow, while the duration of the salt wave, t_w, depends on the longitudinal dispersion. The dispersion of the salt is related to the discharge according to the following relation:

$$Q = \frac{M}{\int_o^{t_w} (S_t - S_o) dt} \tag{4.2}$$

Thus, by measuring the evolution of EC and through the calibration coefficient k, it is possible to recover the discharge Q. However, it is important to remember that this method, to be applied successfully, requires the streamflow to be stable and salt to be well mixed. The former condition, implies that the location of the salt injection has to be far from tributaries' injections or bifurcations and that measurements can not be run during rainy days. The latter condition, instead requires the streamflow to be turbulent.

The measurement procedure consists of two main phases:: (1) the calibration, and (2) the actual salinity measurement in the river.

1. **Calibration** Calibration is required to determine the calibration coefficient k under the specific field conditions (e.g., temperature and baseline conductivity).

The aim is to assess the slope of the linear relationship between conductivity and incremental salinity by performing multiple injections of a concentrated secondary solution into sampled river water. The procedure can be outlined as follows:

Initial rinsing: Before starting the calibration, it is essential to thoroughly rinse all equipment – flasks, thermoses, probes, pipettes, and any other materials – with river water. This step prevents contamination from previous measurements and ensures the accuracy of the conductivity readings.

Preparation of the secondary solution: Once the equipment is clean, the secondary solution has to be prepared: a known amount of river water has to be poured into the flask or thermos that already contains the salt, the container has to be sealed tightly and shook until the salt has completely dissolved. This method minimizes the risk of losing salt due to splashing or sticking to the sides of the container. It is important to keep the water at the river water temperature. This can be achieved by placing the flask in a bath of river water or using a thermos.

Setting up the calibration tank: Afterwards, the calibration tank has to be prepared. The calibration tank can be a large cylinder or a thermos, filled with a known amount of river water. The choice of the container depends on two main factors: the number of conductivity probes that need to be calibrated simultaneously, and whether or not there are calm, still areas of the river available for use. If using a cylinder, it should be kept cool with a surrounding water bath.

Conductivity measurements and evaluation of the calibration coefficient k: The first step to evaluate the calibration coefficient requires to immerse the conductivity probes in the calibration tank and to record the initial electrical conductivity EC_0 of the river water. This provides the baseline measurement. Afterwards, using a pipette, gradually fixed volumes of the secondary salt solution have to be added to the tank. After each addition, the new conductivity value has to be measured and recorded. It is crucial to keep the pipette vertical during each addition to avoid compromising its accuracy (e.g. rest it on the edge of the tank). Modern conductivity probes and meters usually record these values automatically and can interpolate the data to determine the calibration

coefficient k, which will be used during the computation of river discharge (Equation 4.1).

2. **River Measurement** The river measurement consists in dumping salt slug in the river and recording the salt wave in terms of electrical conductivity. The procedure can be outlined as follows:

   Preparation of the salt solution (slug): The injection solution has to be prepared as close as possible to the injection site to minimize the difficulty of transporting a large volume of water. To prepare the solution a known amount of salt has to be dissolved into a known amount of river water. To speed up the dissolution process, a power drill equipped with a paint stirrer can be used. To avoid accidental spills during mixing, it can be convenient to used a bucket or container that is larger than the final solution volume.

   Probe arrangement: To capture the variability of conductivity across the stream cross-section and along the flow direction, four conductivity probes should be places in a T-shaped configuration. Ideally, the measurement process should be carried out by a team of three people: two individuals holding two probes each (for a total of four probes), and a third person responsible for injecting the salt solution into the river. To minimize the risk of data loss due to equipment malfunction, it is advisable to connect some of the probes to one computer and the others to another.

   Measurement execution: Once the probes are properly positioned in the river, the recording can be started to establish the baseline conductivity before the salt is added. Then, the prepared salt slug has to be poured into the river with a single release. It's important to avoid splashing and to ensure that the entire solution enters the river at once. The conductivity values have to be continuously recorded for at least five minutes, with measurements taken at one-second intervals. During this period, the probes have to remain fully submerged in the water to maintain consistent readings. Lifting them out, even briefly, can corrupt the data.

   Data interpretation: After data collection, the conductivity meter or associated software typically calculates the river discharge using the data and the previously determined calibration coefficient k.

   Sample collection: As a good practice, it is wise to collect a sample of the river water in a clean bottle. This sample can be taken back to the lab for

further analysis or verification, especially if any anomalies are suspected in the field data.

Equipment The following is a list of equipment considered essential for conducting discharge measurements using the salt slug method. Additional notes and recommendations are provided based on practical and personal experience in the field.

Required equipment:

1. Waders, rubber boots and work gloves: they are necessary to allow operators to safely work inside the river bed and at low water temperatures;

2. Salt for secondary solution: Performing measurements in the laboratory prior to field activities helps prevent inaccurate dosing. Moreover, when feasible, it is advisable to store the salt directly in the thermos used for preparing the secondary solution, as this approach minimizes salt losses, reduces the risk of splashing, and limits temperature variation;

3. two thermos: one for secondary solution, one as calibration tank if only 1 probe is used;

4. Big cylinder: used as a calibration tank in case multiple probes are used. After rinsing with river water, it can be used to measure the water to pour into the bucket for injection solution;

5. Small cylinder: it used to measure water to pour in the thermos (or big cylinder);

6. Thermometer: it allows for easier reading of water temperature to monitor possible variations during the calibration process. The temperature has to be kept as stable as possible;

7. Salt for injected solution: The injection solution should be sufficiently concentrated to produce a clearly measurable signal, while remaining dilute enough to ensure complete dissolution of the salt. A commonly used concentration is 5 kg of salt dissolved in 20 L of river water (approximately 25%); however, because low water temperatures can slow dissolution, the concentration may

be reduced to about 20% (e.g., 1 kg of salt per 5 L of water) to facilitate preparation;

8. Bucket: preferably the container should have a capacity larger than the final volume of the injection solution to prevent losses caused by splashing during stirring. Better if it has handles to facilitate safe and controlled pouring of the solution into the river;

9. Drill, paint stirrer, and batteries: it is highly important during the preparation of the injection solution to facilitate the dissolution of salt in river water, especially in case of cold water;

10. Probes: EC probes measure both Electrical Conductivity(EC) and temperature (T). 4 would be the best fit in order to measure across the river cross-section and along the river flow, thanks to a T-positioning;

11. Conductivity meter;

12. Computer: it is very important to pay attention to battery sensitivity to cold and to raindrops;

13. Waterproof labels: in case of river water samples;

14. Bottles: in case of river water samples;

15. Pipettes and Pipette tips;

Lab counterpart. Sampled river water may be transported to the laboratory to perform additional analyses, validation tests, or to repeat the calibration procedure under more controlled conditions. Conducting the calibration in the laboratory generally allows for higher accuracy, as several factors that can compromise field measurements can be better controlled or avoided. These include uncertainties in salt mass determination, inaccuracies in water volume measurements, instability of water temperature, potential dilution from rainfall, losses due to splashing during stirring, and contamination of pipettes or other handling equipment. Errors related to salt dosing can be minimized by pre-weighing the salt in the laboratory and storing it in closed containers, rather than in bags from which material may be lost during transfer. When calibration is repeated in the laboratory using sampled river water,

the same procedure described previously is followed, ensuring consistency between field and laboratory calibrations while improving overall measurement reliability.

4.1.2 SteinWasser discharge evaluation

This section presents the evaluation of SteinWasser discharge and the associated laboratory analysis aimed at assessing the sensitivity of discharge estimates to water temperature.

Measuring campaign

Even though the evaluation of SteinWasser streamflow discharge was repetitively carried out, this section presents the evaluation conducted the 8^{th} of July 2025 as also laboratory measurements were performed on the collected river water samples. The in field calibration procedure was run at 12.20am, while the discharge measurement was delayed at 14.50 due to technical problems. The discharge measurement site was located upstream of SteinSee, in a relatively straight and morphologically stable section of SteinWasser, the stream draining from Steingletscher (Figure 4.2). The site was selected in order to obtain good mixing of the tracer plume and avoid the disturbances present in the braided section of the stream.

The calibration was carried out using the equipment (Figure 4.10) and following the procedure described in Section 4.1.1. Specifically, to obtain the secondary solution, 5g of salt were dissolved in 20mL of river water. The salt had been previously weighed in the lab with a high precision scale and placed in a flask with cap. The temperature of the river water measured in the river bed was of 2.8°C but once 4L of river water was located in the calibration tank, the three available probes (coded A, B, and C) measured a mean temperature of 4.7°C (Table 4.1). Despite the overcast and cold day, the water temperature rose because no water bath could be performed and, due to multiple probes, the thermos was not suitable. At this temperature, the mean base electrical conductivity was 96.16 μS/cm (Table 4.1). The used probes were the TQ-Tracer by Sommer. 2 mL of secondary solution was added to the calibration solution at each step using a pipette.

Fig. 4.2. satellite view of Steingletscher system: glacier, meltwater river, lake, measuring site.

(a) (b)

Fig. 4.3. (a) Material used during the discharge measuring campaign at SteinGletscher; (b) Measurement of river velocity.

Table 4.1. River water base conditions measured during calibration and during in-stream measurement.

Probe	**Temperature Calibration [°C]**	**Temperature Measurement [°C]**	**EC Calibration [μS/cm]**	**EC Measurement [μS/cm]**
A	4.6	2.12	94.7	100.7
B	4.7	2.44	97.9	100.6
C	4.7	2.33	95.9	99.9

To obtain the salt slug, 5kg of salt were dissolved in 20L of river water. A drill with a paint stirrer head was used to facilitate the process. As three probes were available, they were placed across the cross-section of the river, around 50 meters downstream of where salt slug was injected (Figure 4.3b). Probes A and C were positioned in the central part of the streamflow, whereas probe B was placed laterally. As a couple of hours passed between calibration and conductivity measurement

due to technical issues, the river water temperature had dropped to a mean value of 2.3°C with a corresponding base EC of 100.4 μS/cm (Table 4.1). Due to the fact that calibration water temperature differed from in-stream conditions, a dedicated laboratory assessment of temperature effects on the calibration coefficient had to be carried out.

Lab evaluations

Laboratory calibrations were performed on sampled river water to quantify the sensitivity of discharge estimates to calibration temperature. The objective was to isolate temperature effects under controlled conditions and to evaluate the magnitude of errors introduced when calibration and in-stream temperatures differ.

Three calibration experiments were conducted at different target temperatures:

1. At 4.7°C: this temperature matches the one used during the field calibration. It includes the error introduced by the mismatch with the actual river temperature, thus reproducing the uncertainty present in field conditions;
2. At 2.8°C: this temperature matches the river temperature originally measured;
3. At 2.3 °C: this temperature closely matches the actual river conditions, providing a more accurate estimate of the calibration coefficient k and, consequently, a more reliable discharge computation.

The most challenging aspect of the laboratory measurements was bringing the water to the target temperature and maintaining it constant in a room-temperature environment. Thermoses were unsuitable, as they did not allow active temperature control (cooling or heating). The adopted solution was to place the cylinder containing river water in an ice bath (Figure 4.4). The ice bath consisted of an ice beaker and an ice cap.

Fig. 4.4. Lab set up to keep the cylinder with river water cool.

The ice beaker was prepared by freezing the following setup: a water-filled plastic bag was placed at the bottom of a larger beaker, on top of which a smaller beaker was positioned and weighted to prevent floating; the remaining space between the walls was then filled with water. The ice cap was obtained by freezing about 3 cm of water in a beaker in which two weighted vials were placed. Two different vial diameters were selected to match the different diameters of the probes (Figure 4.5a): the JENWAY probe (laboratory) and the SOMMER probe (field).

Although glass was preferable to plastic for detaching ice from the vials and beakers, the extraction process was further facilitated by briefly placing the beaker in a warm bath and injecting warm water into the vials. To prevent meltwater from dripping into the calibration tank, the ice cap was wrapped in a plastic bag. Two holes were made to allow the probes to pass through, and the plastic was sealed around them with tape (Figure 4.5b). As the ice melted during each calibration, the freezing process had to be repeated for every calibration run.

Finally, the secondary solution was stored in a bag filled with crushed ice to prevent temperature fluctuations in the calibration solution during injections.

(a) (b)

Fig. 4.5. (a) Ice cap with holes for the probes; (b) Sealed probes.

The first step of the calibration process was rinsing the cylinder, used as a calibration tank, and the probe with distilled water to be sure to avoid contamination, and let them dry. For each calibration, 5g of salt was diluted in 20mL of river water to create the secondary solution. This secondary solution was injected 0.5mL per step in the calibration solution. For the calibration at 2.3°C and 2.8°C, the initial calibration solution was 250mL or river water, while for the one at 4.7°C it was 150mL due to a shortage of stored river water.

The analysis was initially planned using two probes in order to compare their EC measurements. However, because the two probes respond differently to temperature fluctuations and maintaining a stable water temperature proved difficult, only the SOMMER probe was ultimately used. This choice was made since it is the probe employed in the field and therefore the most relevant for the analysis. Only a simple comparison between the two probes was run on the measurement of the base electrical conductivity of river water at different temperatures. It was important to note how both probes need a long time to adjust their temperature measurement, while the EC evaluation stabilizes more rapidly.

4.1.3 Results and Discussion

Measuring campaign

The evaluated calibration coefficients from the field-calibration process at 4.7°C are reported, for each probe, in Table 4.2.

Table 4.2. Measured values calibration coefficient, k, at 4.7 °C for the different probes.

Probe	**k** [μ**S L/cm g**]
A	1750
B	1861
C	2060

Figure 4.6 shows the conductivity values registered from the three probes located in the streamflow: in green Probe A, in red Probe B, and in blue Probe C. The presence of peaks of different heights shows that the tracer was not well mixed across the cross-section. In fact, Probe A, in green, and Probe B, in blue, received the peak roughly at the same time but with different magnitude (even if located roughly 1.5m apart on the same cross section) showing that even though they experienced the same flow velocity they did not experience the same salt wave. This implies a not well mixed condition across the cross-section because, otherwise, the signal would have been more similar. Specifically, Probe A, with a higher peak, was more closely located to the center of the salt plume if compared to Probe C. Probe B will not be taken into account in the following stages as its measurement strongly differs from the others. In fact, due to the relatively fast flow and the small lateral mixing, the later positioning in the streamflow of the probe has likely undermined the effectiveness of the measurement.

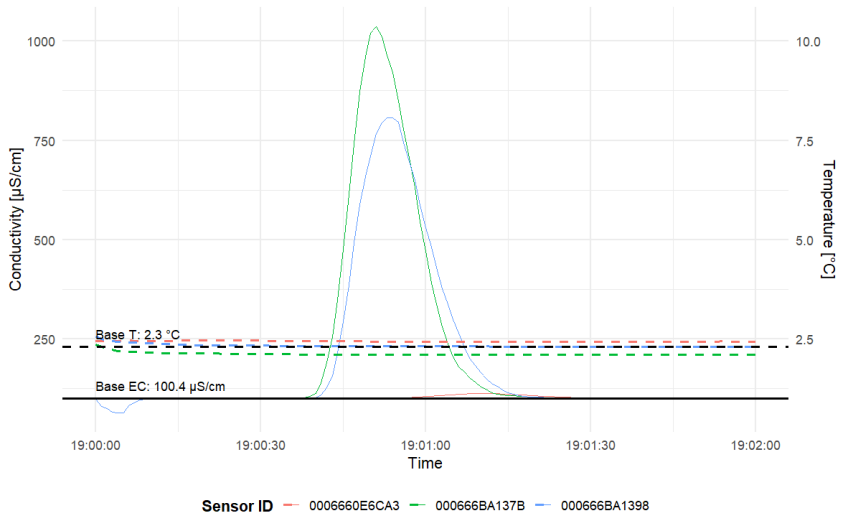

Fig. 4.6. Conductivity measurement registered by the three probes located in the stream flow after the slug dumping. Green, blue and red lines refer to probe A, probe C, and probe B, respectively.

From the field-calibration and EC measurements, the three probes evaluated respectively a discharge of A: 677 L/s, B: 36395 L/s, C: 843 L/s. The discharge measured by Probe B, as mentioned before, will be discarded as it is not considered to be reliable due to the positioning of the probe in the stream flow. The discharge measured by probes A and C are both realistic as they both align with rough estimates. In fact, the stream was roughly 50 cm high in the deepest point, 3 m wide and with a velocity of 1.1 m/s, thus it would roughly transport 1.65 m^3 assuming a rectangle cross-section and 0.8 m^3 with a triangular one. These values are of the same order of magnitude as the tracer-based estimates. Since an incorrect evaluation of k directly affects the calculation of Q, the experimental determination of the calibration coefficient can also be used to obtain a correct evaluation of Q.

Lab evaluation

The calibration measurements revealed distinct linear relationships between EC and salinity depending on temperature, as expected. Tables 4.3, 4.4, and 4.5 present the experimental data of the calibration procedure run at 4.7°C, 2.8°C, and 2.3°C respectively. Figure 4.7 shows the corresponding linear interpolations in grey, orange and blue, respectively. The calibration coefficient is given by the slope. It is worth noting the higher baseline conductivity observed in the river water during calibration

at 2.3 °C. This anomaly can be attributed to the fact that the sampled water bottle was not shaken prior to extracting the portion used for calibration. As a result, salt likely settled at the bottom during storage, and since the pipette drew water from this area, a more concentrated sample was analyzed. From the calibration coefficients k obtained from the experiments carried out, and reported in Table 4.6, it is visible how the temperature strongly affects the discharge evaluation, as 14% and 12% differences in the factor estimation occur between 4.7°C and the lower temperatures (2.8°C and 2.3°C, respectively). This difference propagates to discharge evaluation.

Table 4.3. Calibration experimental data (T = 4.7 °C).

add [L]	**salt added [g]**	**cum salt [g]**	**vol [L]**	**salinity [g/L]**	**T [°C]**	**EC [µS/cm]**
0	0	0	0.15	0	4.7	98.5
0.0005	0.125	0.125	0.1505	0.8306	4.7	1688
0.0005	0.125	0.25	0.151	1.6556	4.7	3293
0.0005	0.125	0.375	0.1515	2.4752	4.7	4812
0.0005	0.125	0.5	0.152	3.2895	4.7	5300

Table 4.4. Calibration experimental data (T = 2.8 °C).

add [L]	**salt added [g]**	**cum salt [g]**	**vol [L]**	**salinity [g/L]**	**T [°C]**	**EC [µS/cm]**
0	0	0	0.25	0	2.8	76.3
0.0005	0.125	0.125	0.2505	0.4990	2.8	818
0.0005	0.125	0.25	0.251	0.9960	2.8	1630
0.0005	0.125	0.375	0.2515	1.4911	2.8	2340
0.0005	0.125	0.5	0.252	1.9841	2.8	3070
0.0005	0.125	0.625	0.2525	2.4752	2.8	3790
0.0005	0.125	0.75	0.253	2.9644	2.8	4580
0.0005	0.125	0.875	0.2535	3.4517	2.8	5430
0.0005	0.125	1	0.254	3.9370	2.8	6000

Table 4.5. Calibration experimental data (T = 2.3 °C).

add [L]	salt added [g]	cum salt [g]	vol [L]	salinity [g/L]	T [°C]	EC [µS/cm]
0	0	0	0.25	0	2.3	230
0.0005	0.125	0.125	0.2505	0.4990	2.3	1328
0.0005	0.125	0.25	0.251	0.9960	2.3	1780
0.0005	0.125	0.375	0.2515	1.4911	2.3	2470
0.0005	0.125	0.5	0.252	1.9841	2.3	3140
0.0005	0.125	0.625	0.2525	2.4752	2.3	4425
0.0005	0.125	0.75	0.253	2.9644	2.3	4620
0.0005	0.125	0.875	0.2535	3.4517	2.3	5510

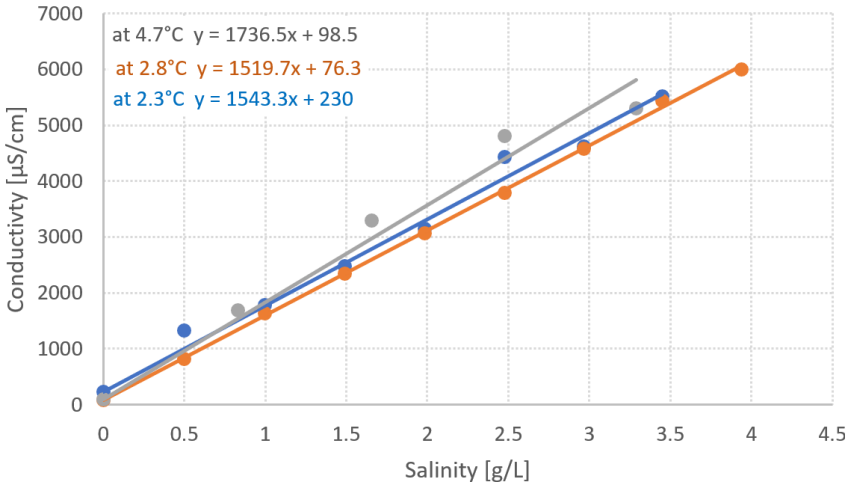

Fig. 4.7. Experimental data of electrical conductivity vs. incremental salinity at different temperatures: 4.7°C in gray, 2.8°C in orange, 2.3°C in blue.

Table 4.6. Experimental values of temperature, calibration coefficient k.

Temperature [°C]	k [μS L/cm g]
4.7	1736.2
2.8	1519.7
2.3	1543.3

Table 4.7 reports the variation of the discharge Q according to the calibration coefficient, which implies a temperature dependence, and the location of the probe in

the stream flow. The evaluation of k at 4.7°C instead of 2.8°C and 2.3°C caused an error of 98.09 L/s (Probe C), 83.79 L/s (Probe A) and 87.40 L/s (Probe C), 74.66 L/s (Probe A) respectively. In this specific case, these variations are comparable to the differences due to the different locations of the probes in a not well-mixed stream: Probe A, less central than probe C, no matter the k coefficient applied, estimates consistently more than 100 L/s more, corresponding to a +14.49%.

Table 4.7. Experimental discharge (Q) values for different probes (A and C) and calibration coefficients ($k(T)$). Variations and Δ on the right side of the table and on the left-bottom refer to variations along the row (different k), the column (different probe) respectively.

Probes	**Q [L/s]**						
	$k = 1736.2$ ($T = 4.7$°C)	$k = 1519.7$ ($T = 2.8$°C)	$k = 1543.3$ ($T = 2.3$°C)	Variation [%] 4.7–2.8°C	Variation [%] 4.7–2.3°C	Δ [L/s] 4.7–2.8°C	Δ [L/s] 4.7–2.3°C
C	786.62	688.53	699.22	14.25	12.50	98.09	87.40
A	671.96	588.17	597.30	14.25	12.50	83.79	74.66
Variation [%] C–A	14.49	14.49	14.49				
Δ [L/s] C–A	114.66	100.36	101.92				

The idea of estimating the difference in discharge only due to the different location of the probes in a not well-mixed stream means assuming no variations in calibration coefficient k estimations even at a defined temperature. As visible in Table 4.2, even though being temperature consistent (T=4.7°C) between the probes, the field calibration resulted in three different k coefficients. This variability can be reconducted to a inhomogeneous mixing in the calibration tank or too quick recording of the EC values after each addition of the secondary solution. It is, in fact, a matter of compromise: the stabilization of EC values requires time but the longer the calibration takes, the warmer the water in the calibration tank becomes. As the field k coefficients that come closer the ones obtained in lab for T=4.7°C is the one evaluated on the field by Probe A, it will be taken as reference to evaluate the different discharges Q according to the EC measurements of each Probe. Table 4.8 reports the Q values that would have been evaluated by the three different probes if they all had the same calibration coefficient k. This allows to restrict the uncertainty in discharge evaluation to the SteinWasser stream conditions.

Table 4.8. Discharge (Q) values assuming the same calibration coefficient, $1/k$, at 4.7 °C for the different probes

Probe	k	Q [L/s]
A	1750	677
B	1750	30918
C	1750	793

Since the field measurement of the discharge could not univocally define SteinWasser discharge due to the different estimations of the probes (A: 677 L/s, C: 843 L/s), the mean value was take as discharge value: 760 L/s. It is relevant to note how the mean value in case of no calibration variability (k constant for 4.7°C) is 728 L/s and for calibration at the same temperature of the stream (T=2.8°C) is 638 L/s.

4.1.4 Conclusions

The results of this study demonstrate that tracer-based discharge estimation is strongly influenced by both the calibration procedure and the mixing of the stream. The field measurements in SteinWasser showed that incomplete lateral mixing can lead to substantial differences in the recorded salt waves, detectable thanks to the different placement of the probes within the stream cross-section. These differences resulted in a 14.49% difference in discharge evaluation. Furthermore, laboratory calibrations confirmed the strong temperature dependence of the conductivity–salinity relationship, with variations in the calibration coefficient, and thus in the discharge evaluation, of 12-14% due to differences in temperature between the stream flow and the calibration tank. Overall, the findings highlight how a 2°C difference between the calibration tank and stream flow has the same impact on the discharge evaluation as a poorly mixed condition in the stream flow.

4.2 Steingletscher glacier sampling for pesticides and PFAS transported by incoming moisture fluxes

Glaciers are increasingly recognized as reservoirs and secondary sources of persistent organic pollutants (POPs). Substances such as insecticides, fungicides, and

herbicides can be transported over long distances through the atmosphere, deposited in cold, high-altitude environments due to snow precipitation and there accumulate. This phenomenon is particularly important in European mountain regions as they are close to emission sources such as industrial, agricultural, and densely populated areas [178–180]. Once deposited, these contaminants can be stored in glacier ice and snowpacks for decades and subsequently released through meltwater. However, the increasing melt rates observed in European glaciers raise concerns regarding the speed at which pollutants are transported through the glacier reservoir into the downstream rivers [181]. This highlights the need to better understand the links between atmospheric transport, cryospheric storage, and hydrological transport of pollutants.

Within this context, the Steingletscher represents an example to investigate the age and the origin of the pesticides and PFAS traces found in the Steinwasser stream. The present Section describes the sampling campaign designed to assess whether traces of pesticides and PFAS could be found in snow and ice samples from the surface of Steingletscher. In the hypothesis that persistent pollutants could be found on the surface, this would imply that the atmospheric transport of these pollutants is an ongoing process and that their transfer through the ice mass occurs over relatively short timescales.

4.2.1 Sampling campaign

The sampling campaign included preparatory lab activities, aimed at organizing and assembling the required equipment, followed by the fieldwork conducted on the glacier.

Preparation and Equipment

To address the research question of whether pesticides and PFAS are present on the surface of the glacier, a large amount of ice is required in order to be able to enrich the meltwater in the lab. At the same time, assessing the potential spatial variability of pollutant traces requires sampling at multiple locations across the glacier surface. As a compromise, the objective of the sampling campaign was to obtain:

1. 7X3 snow samples in glass vials

2. 7x3 snow samples in plastic vials
3. 7x3 ice samples in glass vials
4. 6 glass bottles of ice
5. 2 bottles of water

The choice of different materials for sampling containers was due to the physico-chemical behavior of the target compounds. Glass containers are generally preferred for organic pollutants such as many pesticides, as these compounds can adsorb onto plastic surfaces and plastic materials may release organic contaminants into the samples. In contrast, PFAS are known to strongly adsorb to glass, which can result in losses and biased concentration measurements. For this reason, PFAS-targeted samples were collected in plastic containers.

At each snow sampling location, three samples were collected to capture small-scale spatial variability. Two samples were taken closely (approximately 50 cm apart), while a third was collected further away (approximately 1 m). Analogously, ice samples were collected in triples; however, because individual ice cores exceeded the volume of a single vial, multiple containers were required to store each core.

In addition to the sampling containers, auxiliary equipment was prepared to ensure safe and efficient fieldwork and to minimize contamination risks. This included spare pre-labeled vials, sampling bags for organizing material by location, work gloves and rubber gloves to limit contamination from sunscreen, insulated thermal bags and ice packs to reduce sample warming, a thermometer for rapid temperature checks, and basic glacier tools such as a shovel, ice screws matched to the vial diameter, and an ice axe for extracting ice blocks.

All glass vials and bottles were prepared before the field campaign by baking them in a laboratory oven to remove potential residual organic contaminants (Figure 4.8).

Fig. 4.8. Preparation of vials for baking.

To prevent labeling errors in the field, all containers were pre-labeled in the laboratory (Figure 4.9) using a defined alphanumeric coding system that indicated sample type (snow, ice, or water), glacier of origin, sampling location, and replicate number. For snow samples, replicate identifiers reflected their relative spatial arrangement at each site. The coding system followed the scheme: *"letter"-"glacierCode"-"alphanumeric"*(e.g. sSTE1a).

- Letter:
  - "s": snow sample
  - "i": ice sample
  - "w": water sample
- GlacierCOde: STE stands for STEingletscher
- Alphanumeric:
  - for "i" and "w" samples: *"alphanumeric"* is only a number in ascending order according to the sampling order of ice and water samples

  - for "s" samples: *"alphanumeric"* is a number+letter.
    * number: number in ascending order according to the sampling order of snow samples
    * letter (a,b or c): "a" and "b" are the samples taken roughly 50cm apart, "c" is the one taken around 1m away from "a" and "b"

For clarity, here it is an example for "sSTE1a"

- s: snow sample
- STE: at Steingletcher
- 1: first snow-sample location of the sampling camping
- a: out of the 3 samples, this is the first one

Fig. 4.9. Prepared vials (from top to bottom): brown glass vials for snow sampling, orange-cap plastic vials for snow sampling, blue-cap glass vials for ice sampling.

Finally, to facilitate the sampling process and avoid confusion during fieldwork, vials were organized in numerical order, wrapped in plastic film, and stored in separate bags according to sample type. This preparatory work was essential to ensure efficient sampling under variable and sometimes challenging glacier conditions (Figure 4.10)

Fig. 4.10. Vials and extra material

Sampling

The sampling campaign was conducted on the 24^{th} of July 2025 by two operators (me and and Justine Berg from the Hydrological group of the University of Bern). The sampling process took place mostly in sunny and warm conditions, except for the first two sampling locations, affected by low cloud cover. Snowfall had occurred in the days preceding the campaign, however, on the lower part of the glacier, snow was already largely absent already on the evening of the 23^{rd}.

Samples were taken in 10 locations (Figure 4.11) across the glacier on the way down from the upper glacier near SustenHorn (Point A) at 3500 masl to Tierberglihütte (Point B) at 2790 masl (Figure 4.12).

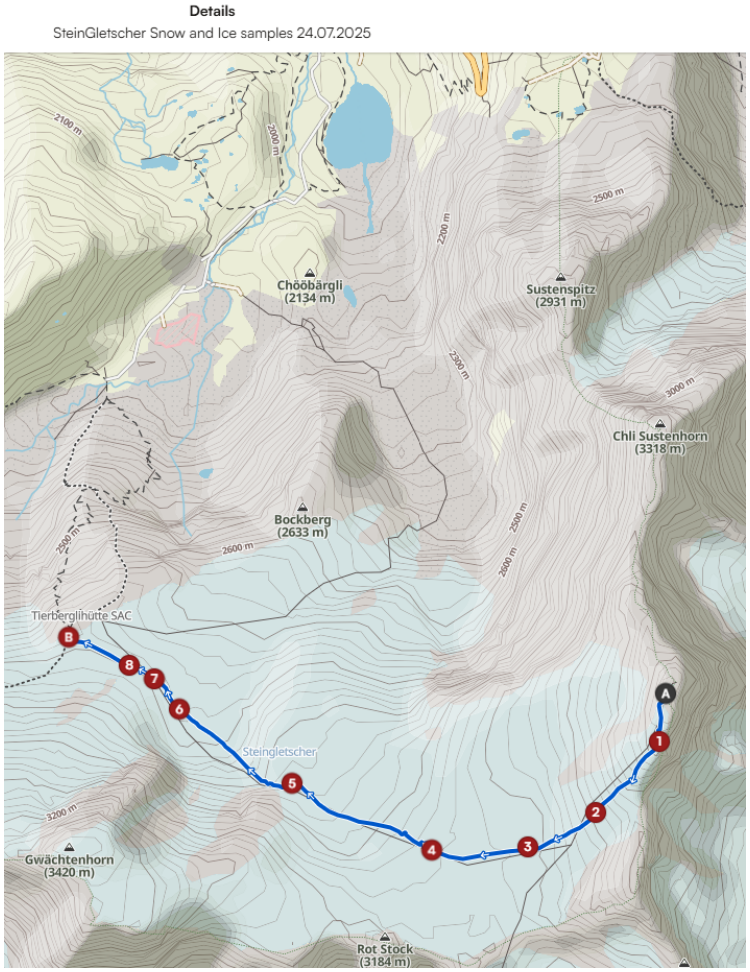

Fig. 4.11. Sampling locations from Point A, SustenHorn, to Point B, Tierberglihütte.

Fig. 4.12. View of Steingletcher on the right and Tierberglihutte on the left. In red the sampling route from SustenHorn (Point A) to the last point close to Tierberglihutte (Point B).

This transect-based approach was adopted to capture variability across different sections of the glacier, including changes in elevation and surface morphology. Sampling locations were not predefined before the field campaign but were instead defined in the field based on local glacier morphology and accessibility. This strategy allowed for the sampling on a wide range of morphological characteristics, such as steep slopes, flat areas, local depressions across both the upper and lower parts of the glacier.

Depending on local conditions, snow, ice, and/or surface meltwater samples were collected at each location. Snow sampling involved collecting the uppermost surface layer of snow, ensuring to compact the snow inside the vial both to reduce airspace, and thus minimise isotopic contaminations between air and snow, and collect more mass. Ice samples were obtained either by coring with ice screws for the glass vials or by extracting ice blocks using an ice axe for glass bottles. At one location (Point 3), an ice lens was identified approximately 30 cm below the snow surface and sampled separately in a plastic bag (Figure 4.13b). Surface meltwater samples were

collected at locations where superficial meltwater flow was observed, particularly in the lower part of the glacier.

As sampling locations were not decided beforehand, the sample numbers and location numbers do not correspond. The accordance between sampling location and sample code is here reported:

- Point A: sSTE1
- Point 1: sSTE2 + iSTE1 + iSTE1Bottle(x2)
- Point 2: sSTE3
- Point 3: sSTE4 + iSTE2 + icelayer
- Point 4: sSTE5 + iSTE3 + iSTE3Bottle(x2)
- Point 5: sSTE6 + iSTE4
- Point 6: sSTE7 + iSTE5 + wSTE1
- Point 7: iSTE6 + iSTE6Bottle(x2)
- Point 8: iSTE7 + wSTE2
- Point B: sSTE8 + iSTE8

Point A, 1, 2 corresponded to steep slope areas in the upper glacier (Figure 4.13a), while Points 3 and 4 corresponded to flat/local depression areas. Point 5 was located within the serac area between the upper and lower parts of the glacier. Points 6,7,8 were located in the relatively flat areas of the lower part of the glacier, were surface meltwater flow was abundant.

From point 4 onward (Figure 4.13c), samples contained liquid water due to high air temperatures. At Points 6,7, and 8 active surface runoff was observed (Figure 4.13d). Samples collected at Point B were not planned in advance and were collected using spare vials.

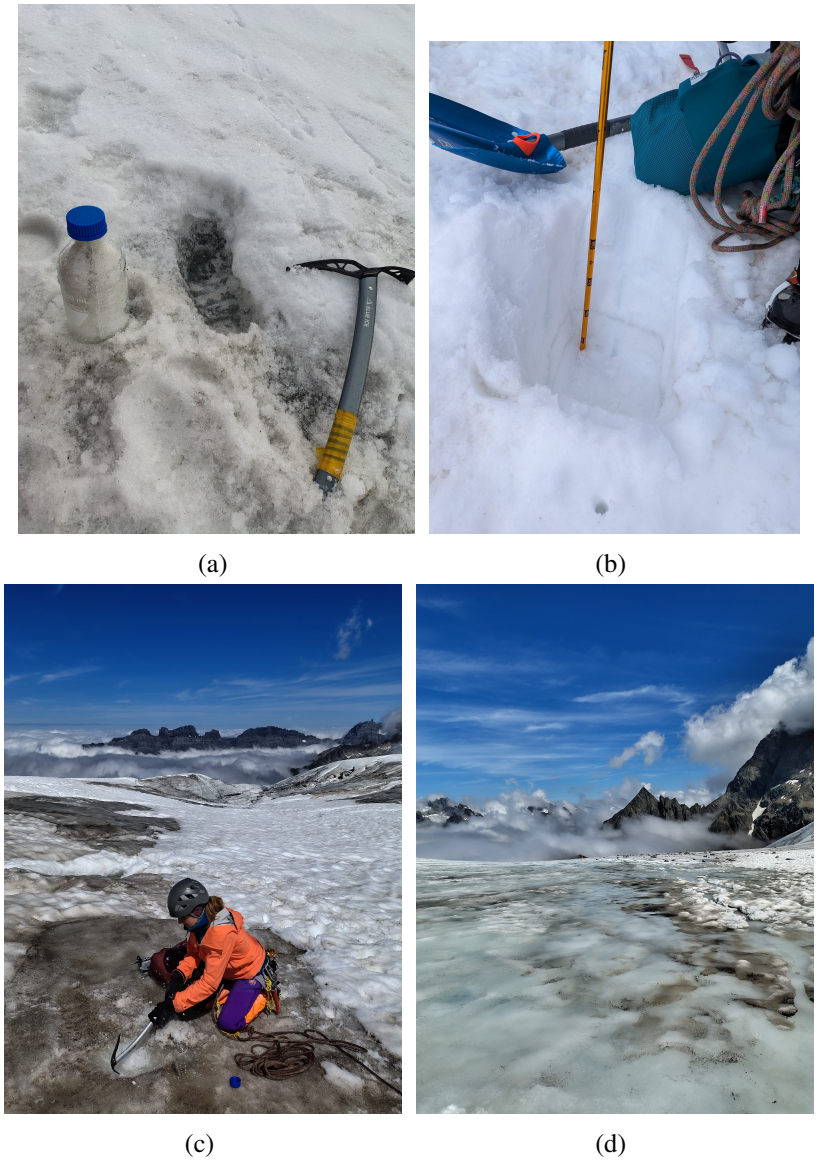

(a) (b)

(c) (d)

Fig. 4.13. (a) Ice sampling at point A, (b) ice lens at Point 3, (c) ice sampling at Point 4, (d) running water at Point 6

During the field campaign, all vials and bottles were stored in insulated cooling bags. The use of ice packs in the field was not feasible due to weight and space limitations associated with glacier travel and the limited number of operators. Once returned back at 2100 masl, in the vehicle samples were immediately transferred to a cooled box to reduce thermal exposure. Once back in the laboratory, all samples were placed in a freezer at 20 °C for long-term storage. This procedure was adopted to

minimize chemical alteration both in terms of pollutants concentration and isotopic composition before the laboratory processing and analysis.

4.2.2 Origin of pesticide and PFAS traces in SteinWasser: glacier samples and moisture tracking

For this study, the RECON model was applied to identify the upwind moisture plume responsible for precipitation over the Steingletscher. Since the ice samples—particularly those collected in the lower part of the glacier—contained substantial amounts of meltwater originating from higher elevations and potentially being mixed with water from earlier periods, a mean annual analysis was performed to account for contributions from precipitation occurring in previous months.

4.2.3 Results and discussion

The Steingletscher is entirely contained within a single RECON cell (Figure 4.14, located along the Alpine divide in a region characterized by highly complex topography. This cell encompasses both the high-elevation peaks of the Bernese Oberland and Valais and the lower-lying valley floors and lakes of the surrounding area. Although such terrain complexity strongly influences local airflow patterns, RECON is expected to reliably capture the large-scale origin of precipitation reaching the site.

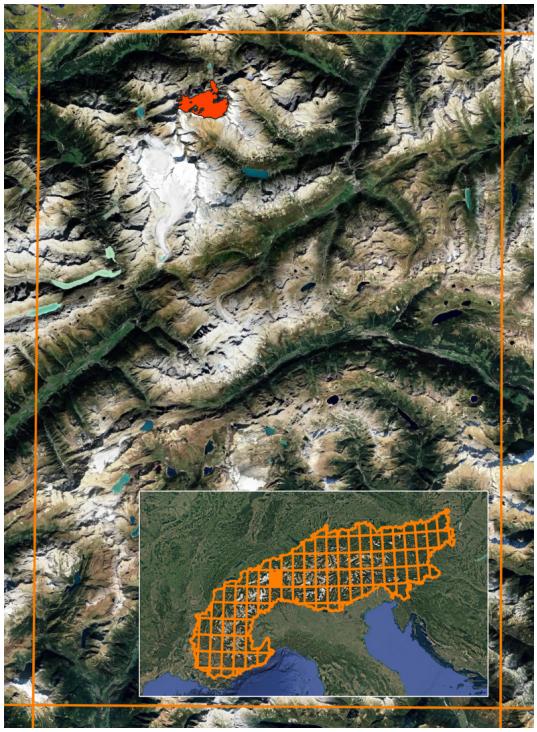

Fig. 4.14. Localisation of Steingletscher, in red, within the RECON grid, in orange.

Figure 4.15a illustrates the mean yearly upwind precipitation plume associated with the RECON cell, (colors refer to the quantiles), while Table 4.9 summarizes the mean annual contribution from each moisture source. Marine moisture dominates the precipitation budget, accounting for approximately 64.5% of total annual precipitation, whereas continental sources contribute the remaining 34.6%. Among marine sources, the Atlantic Ocean is the primary contributor, supplying more than 45.6% of the annual precipitation, followed by the Mediterranean Sea, which accounts for just under 19%. These proportions are consistent with those reported for the Northern Alps (Table 3.2), though with an even stronger dependence on Atlantic-derived moisture (by about three percentage points). As visible in Figure 4.15, continental moisture is predominantly of European origin, especially western Pianura Padana, eastern France and northern Spain, followed by the Maghreb, and west Africa and the eastern coast of north America. Specifically, European land areas contribute to 82.1% of land-based precipitation, whereas Africa accounts for only 13.4% of continental moisture (4.65% of total precipitation) (Table 4.9).

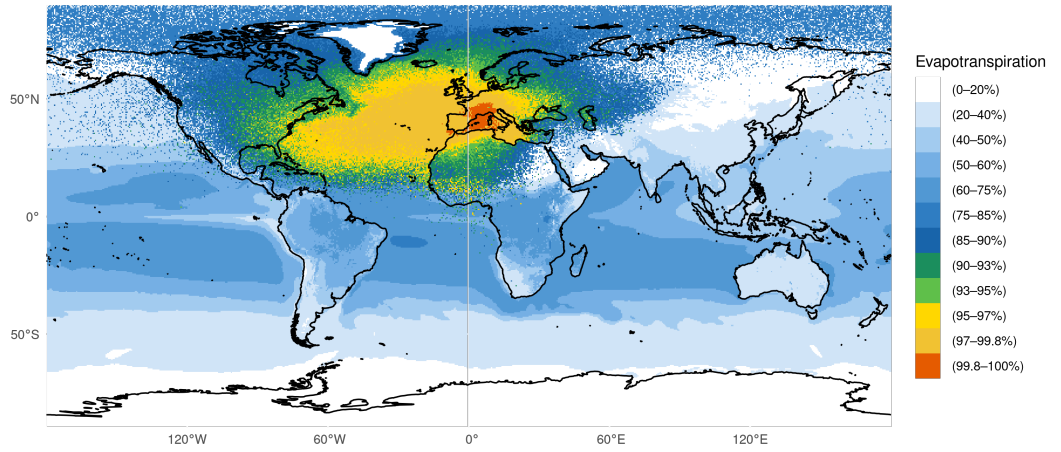

(a)

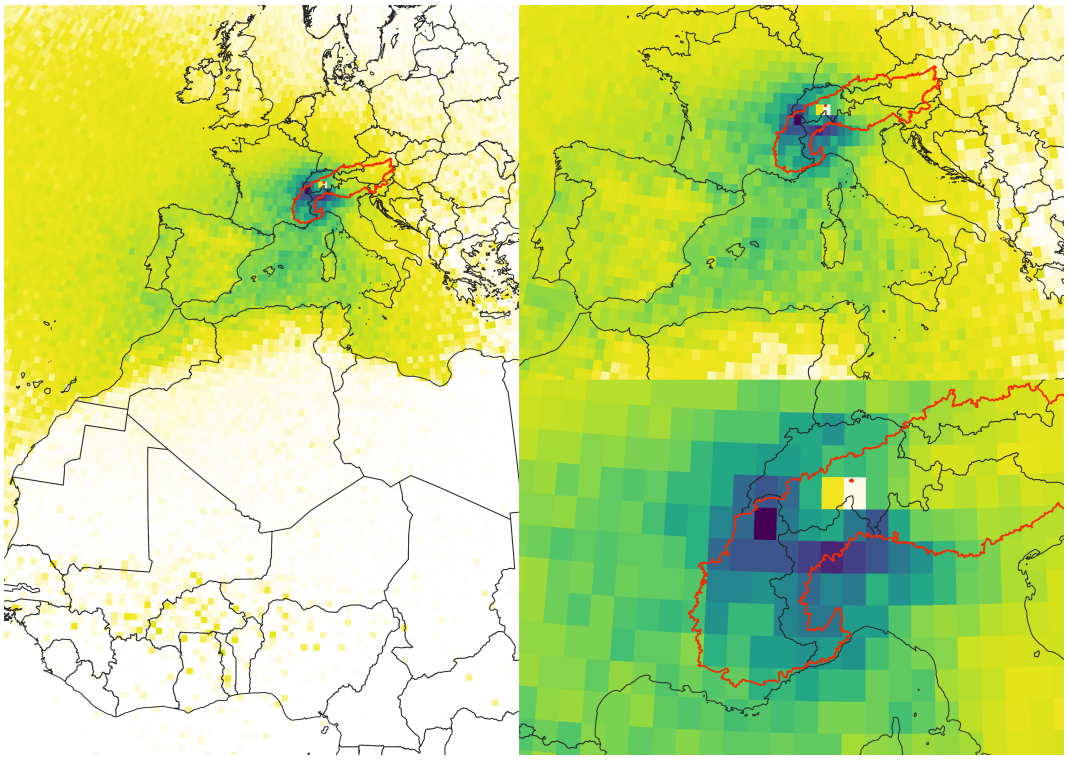

(b)

Fig. 4.15. Visual representation of the evapotranspiration shed of the precipitation occurring on the RECON cell containing Steingletscher. (a) Global upwind plume: the colors are related to cumulative quantiles. (b) Zooms of the upwind plumes: colors refer to the evapotranspiration flux from each contributing cell expressed in m^3/year (the maximum corresponds to roughly 20 mm)

Table 4.9. Mean yearly origin of precipitation on Steingletscher

Contribution Source	**Steingletscher** [%]
Marine	64.5
Atlantic Ocean	45.6
Mediterranean Sea	18.9
Adriatic Sea	0.67
Aegean-Levantine Sea	0.2
Tyrrhenian Sea and Western Mediterranean Sea	14.9
Ionian Sea and Central Mediterranean Sea	3.04
Land	34.6
Europe	28.5
Africa	4.65
North America	1.3

Preliminary analyses of water, snow, and ice samples collected at Steingletscher by Aurea Hernandez and Serafina Heiter (University of Bern) revealed the presence of 35 pesticide compounds in the surface layer of the glacier. Table 4.10 shows the list of pesticides, their type, the current EU status and whther they are compounds that travel through moisture transport. The presence of banned pesticides in surface samples suggests that these compounds are still reaching the glacier through ongoing atmospheric deposition, although contributions from previously deposited contaminants cannot be excluded. The upwind plume from the month of July can identify the possible sources.

Several of the detected compounds correspond to pesticides that are no longer approved for use in the European Union, including acetochlor, carbendazim, chlorpyrifos, diazinon, dinoseb, diuron, flusilazole, isoproturon, prochloraz, and propiconazole. Many of these substances were widely used in European agriculture throughout the late twentieth and early twenty-first centuries before being progressively withdrawn. Consequently, current emissions from agricultural applications in Europe are expected to be relatively low. Nevertheless, several of these compounds exhibit physicochemical properties that allow them to volatilize from soils or vegetation and undergo atmospheric transport over regional or long distances [182]. Semi-volatile pesticides such as chlorpyrifos and diazinon have relatively high

atmospheric transport potential and have frequently been detected in rainwater and snow deposition [183]. In contrast, other compounds such as diflufenican, flufenacet, and napropamide are less volatile and tend to be more strongly associated with soils or particles, making them less likely to be transported over long distances through atmospheric moisture pathways. Given that the moisture source analysis indicates that most precipitation reaching the glacier originates from European land areas, the presence of these compounds in SteinWasser likely reflects a combination of regional atmospheric transport and the remobilization of legacy contaminants stored in environmental reservoirs.

4.2.4 Conclusions

Overall, the activities presented in this chapter highlight the value of integrating field observations, laboratory analyses, and modelling approaches to investigate the connections between atmospheric transport, cryospheric storage, and alpine water quality. The discharge measurements carried out in the SteinWasser stream highlighted the sensitivity of discharge estimates to both probe positioning and calibration conditions, showing that incomplete mixing across the stream section and temperature differences between field and calibration environments can introduce uncertainties on the order of 10–15%. These results emphasize the importance of being aware of uncertainties in field measurements, especially in this case, when interpreting pollutant concentrations in the stream water. In parallel, the glacier sampling campaign provided the first evidence of multiple pesticide compounds in surface snow and ice on Steingletscher, suggesting that contaminants detected in the SteinWasser stream may originate from both legacy storage within the glacier and ongoing atmospheric deposition. Moisture tracking analyses, which showed that most precipitation-sourced reaching the glacier originates from European land areas, offer an initial framework for identifying the potential atmospheric pathways through which pollutants reach high-altitude Alpine environments. Even though further laboratory analyses and longer observational records are required to fully characterize these processes, the work presented here establishes a methodological basis for future investigations. More broadly, it highlights the potential of interdisciplinary research linking hydrology, meteorology–climatology, and environmental pollutant analysis.

Table 4.10. Detected pesticide compounds, their type, EU regulatory status, and atmospheric transport potential.

Compound	Type	EU status	Atmospheric transport
Acetochlor	Herbicide	Banned since 2012	Moderate
Azoxystrobin	Fungicide	Approved	Moderate
Carbendazim	Fungicide	Banned since 2014	Moderate
Chlorpyrifos	Insecticide	Banned since 2020	High
Cyprodinil	Fungicide	Approved	High
Diazinon	Insecticide	Banned since 2007	High
Difenoconazole	Fungicide	Approved	Moderate
Diflufenican	Herbicide	Approved	Low
Dinoseb	Herbicide	Banned since 1991	Moderate
Diuron	Herbicide	Banned since 2008	Moderate
Ethofumesate	Herbicide	Approved	Low
Fenoxycarb	Insecticide	Approved	Moderate
Fenpropidin	Fungicide	Approved	Moderate
Fenpropimorph	Fungicide	Approved	Moderate
Fluazifop-P-butyl	Herbicide	Approved	High
Fluazinam	Fungicide	Approved	Moderate
Flufenacet	Herbicide	Approved	Low
Fluopicolide	Fungicide	Approved	Moderate
Fluopyram	Fungicide	Approved	Moderate
Flusilazole	Fungicide	Banned since 2013	Moderate
Fluxapyroxad	Fungicide	Approved	Moderate
Imidacloprid	Insecticide	Banned outdoor since 2018	Moderate
Isoproturon	Herbicide	Banned since 2016	Low
Mandipropamid	Fungicide	Approved	Moderate
Metalaxyl	Fungicide	Approved	High
Metrafenone	Fungicide	Approved	Moderate
Napropamide	Herbicide	Approved	Low
Pethoxamid	Herbicide	Approved	Low
Picoxystrobin	Fungicide	Approved	Moderate
Pirimicarb	Insecticide	Approved	Moderate
Prochloraz	Fungicide	Banned since 2023	Moderate
Propiconazole	Fungicide	Banned since 2019	Moderate
Prosulfocarb	Herbicide	Approved	High
Pyraclostrobin	Fungicide	Approved	Moderate
Pyraflufen-ethyl	Herbicide	Approved	Low

Chapter 5

Conclusions

Mountain regions and lowland agriculture are tightly connected through both riverine and atmospheric pathways. Mountains support lowland agriculture through river discharge and contributing to lowland precipitation. At the same time, lowland agriculture can, in turn, supply atmospheric moisture that produces precipitation over mountain regions. Despite the increasing recognition of these complex interactions, the quantification of both atmospheric linkages and the regional-scale agricultural dependence on mountain water remain poorly explored. Thus, in this framework, this study addressed these knowledge gaps by investigating the bilateral interconnection between the Alps and lowland agriculture. Specifically, particular attention was paid to quantifying the dependence of Pianura Padana agriculture on irrigation water and atmospheric Alpine water supply, and to the role of moisture transport in conveying agriculture-borne pesticide traces to the alpine Steingletscher glacier catchment.

This was achieved by combining agro-hydrological modelling, to evaluate irrigation demand, with atmospheric moisture tracking to quantify the atmospheric fluxes.

On the irrigation demand side, this research introduced and applied WaterCROPv2, a physically based agro-hydrological model designed to balance reliability, transparency, and computational efficiency at regional scales. Building on the original WaterCROPv1, the updated model improves the estimation of the crop water demand through a higher temporal resolution and the inclusion of several processes such as the daily plant physiology, rainfall interception, and dynamic soil leakage. Despite its simplicity and reliance on readily available input data, WaterCROPv2 demonstrated good agreement with reference data and previous studies, and sensitivity analyses

confirmed the robustness of its outputs. While limitations in applicability remain under extreme stress conditions and for perennial crops, the model proved to be well-suited for regional-scale assessments of herbaceous and seasonal crops. The application of WaterCROPv2 to maize cultivation in Italy allowed for the evaluation of its mean irrigation water demand while showing its potential as a decision-support tool for water managers and policymakers. The analysis identified regions where maize production is climatically sustainable and others where it is highly water-demanding. The flexibility of the model to test alternative irrigation strategies, such as a complete transition to micro-irrigation, enabled the evaluation of management scenarios. This scenario suggested a mean reduction in irrigation water use of about 21%, with potential savings of up to 30–40% in areas with high water availability where low efficiency irrigation system are currently used. By intersecting irrigation demand with existing irrigation infrastructure, the study further highlighted where investments in system upgrades would have the greatest benefits. In a context of increasing water scarcity, WaterCROPv2 offers a practical tool to assess agricultural sustainability.

On the atmospheric side, coupling the moisture-tracking dataset, RECON, with ERA5-Land, the study quantified the mean yearly bidirectional atmospheric moisture fluxes between the Alps and the lowlands, showing how the Alps function as a major sink for atmospheric moisture and as a significant source of evapotranspired water that contributes to downwind precipitation. Annually, the Alps receive approximately 286 km^3 of atmospheric moisture, mainly originating from the North Atlantic, the Mediterranean Sea, and European land. Orographic effects lead to strong spatial heterogeneity in precipitation, with contrasts between the northern and southern Alpine slopes both in terms of origin and magnitude. Evapotranspiration from the Alps amounts to about 101 km^3 per year with the vast majority recycling over European land. This highlights how Alpine moisture supports precipitation across large parts of Europe, including regions far beyond the Alpine domain. At the same time, a non-negligible fraction of this moisture returns to the Alps, contributing up to nearly 10% of local precipitation. The coupling between the Alps and the Pianura Padana showed the existing atmospheric link between highlands and lowland agriculture. Alpine evapotranspiration contributes, on an yearly average, to about 5% of precipitation over agricultural land, reaching up to 7% in specific hotspots. Single sink locations highlighted the local nature of agriculture dependency from Alpine evapotranspiration hinting at the existence of stronger convective seasonal fluxes.

Furthermore, even though moisture transport from the Pianura Padana back to the Alps is weaker, localized feedbacks exist, especially between the western plain and the central Southern Alps. The asymmetric nature of these source–sink relationships identified both at smaller (Alps-Pianura Padana) and larger (Alps-Europe) scales highlights the "hopping" behaviour of atmospheric moisture transport, for which regions supplying moisture are not necessarily the ones receiving it in return. This imbalance has relevant implications for the propagation of meteorological droughts.

The relevance of moisture transport from lowland agricultural land to the Alps found evidence on the detection of pesticides, agriculture-born pollutants, in the high alpine catchment of Steingletscher glacier in the Swiss Alps. While the sampling campaign has had the role of understanding whether the glacier is currently acting a secondary source of pollutants or the pesticides are still incoming via moisture fluxes, the moisture tracking analysis assessed the source regions of incoming moisture. The identification of the upwind plume indicated that the glacier is also influenced by long-distance source regions rather than only local sources. This highlights that high-alpine environments, despite their remoteness, are affected by anthropogenic processes occurring in local and far lowland regions. Including smaller scale atmospheric dynamics and applying single sink analysis it would be possible to better depict the dynamics of moisture transport towards such alpine environments.

By jointly quantifying irrigation demand and atmospheric moisture pathways, this study shows that hydrological dependencies cannot be fully understood through surface water analyses only. Extending this joint framework to multiple crops and climate scenarios, future works could compare total agricultural demand with future local water availability addressing potential issues related to groundwater and surface water exploitation for agricultural purposes. More over, by incorporating hydrological modeling of the Po River basin and performing discharge routing analyses, the river flow could be partitioned into mountain-origin and plain-origin components. This would enable a more precise quantification of Pianura Padana irrigation dependence on Alpine-derived water resources. Furthermore, considering inter-annual and seasonal variability of atmospheric fluxes, it would be possible to disentangle the convective connections from the long-distance circulation, to estimate how vulnerable the incoming atmospheric moisture pathways are, and to assess the propagation dynamics of droughts between mountain regions and agricultural land. Overall, these suggestions for future works reflect the importance of researching on

the connection between highland and lowland regions as they directly influence water availability for agriculture and energy production and contribute to the transport of air pollutants and thus, extending their impacts well beyond hydrological processes only.

References

[1] Daniel Viviroli, Hans H. Dürr, Bruno Messerli, Michel Meybeck, and Rolf Weingartner. Mountains of the world, water towers for humanity: Typology, mapping, and global significance. *Water Resources Research*, 43:W07447, 2007. doi: 10.1029/2006WR005653.

[2] Sarah Hanus, Peter Burek, Mikhail Smilovic, Jan Seibert, and Daniel Viviroli. Seasonal variability in the global relevance of mountains to satisfy lowland water demand. *Environmental Research Letters*, 19(11):e114078, 2024. doi: 10.1088/1748-9326/ad8507.

[3] FAO. *The state of the world's land and water resources for food and agriculture (SOLAW) - Managing systems at risk.* Food and Agriculture Organization of the United Nations, 2011. URL https://www.fao.org/4/i1688e/i1688e00.htm.

[4] Tony Fujs and Haruna Kashiwase. Strains on freshwater resources: The impact of food production on water consumption. World Bank Data Blog, 2023. URL https://blogs.worldbank.org/en/opendata/strains-freshwater-resources-impact-food-production-water-consumption.

[5] Bingfang Wu, Fuyou Tian, Miao Zhang, Shilong Piao, Hongwei Zeng, Weiwei Zhu, Junguo Liu, Abdelrazek Elnashar, and Yuming Lu. Quantifying global agricultural water appropriation with data derived from earth observations. *Journal of Cleaner Production*, 358, 2022. doi: 10.1016/j.jclepro.2022.131891.

[6] C. Adler, P. Wester, I. Bhatt, C. Huggel, G. E. Insarov, M. D. Morecroft, V. Muccione, and A. Prakash. Cross-chapter paper 5: Mountains. In H.-O. Pörtner, D. C. Roberts, M. Tignor, E. S. Poloczanska, K. Mintenbeck, A. Alegría, M. Craig, S. Langsdorf, S. Löschke, V. Möller, and A. Okem, editors, *Climate Change 2022: Impacts, Adaptation and Vulnerability*, pages 2273–2318. Cambridge University Press, Cambridge, UK and New York, NY, USA, 2022. URL https://www.ipcc.ch/report/ar6/wg2/chapter/ccp5/.

[7] Yoshihide Wada, Dominik Wisser, and Marc F. P. Bierkens. Global modeling of withdrawal, allocation and consumptive use of surface water and groundwater resources. *Earth System Dynamics*, 5:15–40, 2013. doi: 10.5194/esd-5-15-2014. URL https://esd.copernicus.org/articles/5/15/2014/.

[8] J. Hristov, J.-C. Ciscar, L. Feyen, and A. Soria. Climate change impacts on eu agriculture: Final report of the peseta iv project, 2020. URL https://joint-research-centre.ec.europa.eu/system/files/2020-05/pesetaiv_task_3_agriculture_final_report.pdf.

[9] C. Schneider, C. L. R. Laize, J. Alcamo, T. Henrichs, and Z. W. Kundzewicz. How will climate change modify river flow regimes in europe? *Hydrology and Earth System Sciences*, 17:325–345, 2013. doi: 10.5194/hess-17-325-2013. URL https://hess.copernicus.org/articles/17/325/2013/.

[10] Nicola Colombo, Mauro Valt, Emanuele Romano, Franco Salerno, Danilo Godone, Paola Cianfarra, Michele Freppaz, Maurizio Maugeri, and Nicolas Guyennon. Long-term trend of snow water equivalent in the italian alps. *Journal of Hydrology*, 608:128185, 2022. doi: 10.1016/j.jhydrol.2022.128185. URL https://www.sciencedirect.com/science/article/pii/S0022169422011027.

[11] Sarah Hanus, Peter Burek, Mikhail Smilovic, Jan Seibert, Yoshihide Wada, and Daniel Viviroli. Dependence of lowland water use on mountain runoff globally: Interannual variability and future changes at seasonal scale. *Earth's Future*, 13, 2025. doi: 10.1029/2025EF006407. URL https://agupubs.onlinelibrary.wiley.com/doi/full/10.1029/2025EF006407.

[12] Ze-Long Yang, Peng Bai, and Kaiwen Wang. Irrigated agriculture on the southern and northern slopes of the tianshan mountains faces different risks of water scarcity. *Advances in Climate Change Research*, 2025. doi: 10.1016/j.accre.2025.10.009. URL https://www.sciencedirect.com/science/article/pii/S167492782500231X.

[13] Jorge Jódar, Jesús Carrera, and Antonio Cruz. Irrigation enhances precipitation at the mountains downwind. *Hydrology and Earth System Sciences*, 14:2003–2010, 2010. doi: 10.5194/hess-14-2003-2010.

[14] Remco J. de Kok, Obbe A. Tuinenburg, Pleun N. J. Bonekamp, and Walter W. Immerzeel. Irrigation as a potential driver for anomalous glacier behavior in high mountain asia. *Geophysical Research Letters*, 45(4):2047–2054, 2018. doi: 10.1002/2017GL076158. URL https://agupubs.onlinelibrary.wiley.com/doi/abs/10.1002/2017GL076158.

[15] European Commission. Cap strategic plan for italy 2023-2027, 2022. Commission Implementing Decision approving the CAP Strategic Plan of Italy.

[16] Food and Agriculture Organization of the United Nations. Global land cover – share (glc-share). https://www.fao.org/land-water/land/land-governance/land-resources-planning-toolbox/category/details/en/c/1036355/, n.d. Land Resources Planning Toolbox. Accessed December 2025.

[17] Benedetta Monteleone and Ilaria Borzì. Drought in the po valley: Identification, impacts and strategies to manage the events. *Water*, 16(8):1187, 2024. doi: 10.3390/w16081187.

[18] SuWaNu Europe Project. State of play analysis: Po river basin (italy), 2021. URL https://suwanu-europe.eu/wp-content/uploads/2021/05/State-of-play_Po-River-Basin-Italy.pdf. Project report.

[19] ISTAT. Preliminary estimate of agricultural economic accounts – year 2024, 2025. URL https://www.istat.it/wp-content/uploads/2025/01/Report_Preliminary_estimate_of_agricultural_economy_trend_2024.pdf.

[20] IPCC. Climate change 2022: Impacts, adaptation and vulnerability, 2022.

[21] Francesco Tornatore. District water balance and use of water in agriculture in the po river basin. Presentation at the 22nd EURO-INBO International Conference, Parma, Italy, 2025. URL https://www.inbo-news.org/wp-content/uploads/2025/05/2025_EURO-INBO_Parma_WEFE_ADBPo_Tornatore.pptx.pdf. Available as PDF from International Network of Basin Organizations (INBO).

[22] Yves Tramblay, Aristeidis Koutroulis, Luis Samaniego, Sergio M. Vicente-Serrano, Florence Volaire, Aaron Boone, Michel Le Page, Maria Carmen Llasat, et al. Challenges for drought assessment in the mediterranean region under future climate scenarios. *Earth-Science Reviews*, 210:103348, 2020. doi: 10.1016/j.earscirev.2020.103348.

[23] Jonathan Spinoni, Jürgen Vogt, Guido Naumann, Paulo Barbosa, and Alessandro Dosio. Will drought events become more frequent and severe in europe? *International Journal of Climatology*, 38:1718–1736, 2018. doi: 10.1002/joc.5291.

[24] Francesco Avanzi, Francesca Munerol, Massimo Milelli, Simone Gabellani, Christian Massari, Manuela Girotto, Edoardo Cremonese, Marta Galvagno, Giulia Bruno, Umberto Morra di Cella, Lauro Rossi, Marco Altamura, and Luca Ferraris. Winter snow deficit was a harbinger of summer 2022 socio-hydrologic drought in the po basin, italy. *Communications Earth & Environment*, 5:64, 2024. doi: 10.1038/s43247-024-01222-z.

[25] Martin Beniston, Daniel Farinotti, and Markus Stoffel. The european mountain cryosphere: A review of its current state, trends, and future challenges. *The Cryosphere*, 12:759–794, 2018. doi: 10.5194/tc-12-759-2018.

[26] Francesco Avanzi, Giampaolo Ercolani, Simone Gabellani, Elena Cremonese, Paolo Pogliotti, Gianluca Filippa, Umberto Morra di Cella, Sara Ratto, Hervé Stevenin, Marco Cauduro, and Stefano Juglair. Learning about precipitation lapse rates from snow course data improves water balance modeling. *Hydrology and Earth System Sciences*, 25:2109–2131, 2021. doi: 10.5194/hess-25-2109-2021.

[27] Ronald B. Smith. The influence of mountains on the atmosphere. *Advances in Geophysics*, 21:87–230, 1979.

[28] Christoph Schär, Huw C. Davies, and Daniel Lüthi. Simulation of mesoscale atmospheric dynamics in the vicinity of the alps. *Quarterly Journal of the Royal Meteorological Society*, 124:361–394, 1998.

[29] Stefano Tibaldi, Ennio Tosi, Antonio Navarra, and Luca Pedulli. Northern and southern patterns of atmospheric blocking. *Tellus A*, 42:343–356, 1990.

[30] C. David Whiteman. *Mountain Meteorology: Fundamentals and Applications*. Oxford University Press, New York, 2000. ISBN 978-0195132717.

[31] R.G. Barry. Mountain weather and climate. *Routledge*, 1992.

[32] C. W. Thornthwaite and J. R. Mather. *The Water Balance*, volume 8. Publications in Climatology, 1955.

[33] H. L. Penman. Natural evaporation from open water, bare soil and grass. *Proceedings of the Royal Society of London. Series A*, 193(1032):120–145, 1948. doi: 10.1098/rspa.1948.0037.

[34] Jan Doorenbos and William O. Pruitt. *Crop Water Requirements*. FAO Irrigation and Drainage Paper No. 24. FAO, Rome, 1977.

[35] Lorenzo A. Richards. Capillary conduction of liquids through porous mediums. *Physics*, 1(5):318–333, 1931. doi: 10.1063/1.1745010.

[36] Reinder A. Feddes, Peter J. Kowalik, and Henry Zaradny. *Simulation of Field Water Use and Crop Yield*. John Wiley & Sons, New York, 1978.

[37] Ian R. Cowan. Transport of water in the soil–plant–atmosphere system. *Journal of Applied Ecology*, 2(1):221–239, 1965. doi: 10.2307/2401706.

[38] John R. Philip. Plant water relations: Some physical aspects. *Annual Review of Plant Physiology*, 17:245–268, 1966. doi: 10.1146/annurev.pp.17.060166.001333.

[39] C. Allan Jones and James R. Kiniry. *CERES-Maize: A Simulation Model of Maize Growth and Development*. Texas A&M University Press, College Station, TX, 1986.

[40] Cornelis A. van Diepen, Joost Wolf, Herman van Keulen, and Cornelis Rappoldt. Wofost: A simulation model of crop production. *Soil Use and Management*, 5(1):16–24, 1989. doi: 10.1111/j.1475-2743.1989.tb00755.x.

[41] James R. Williams, C. Allan Jones, and Paul T. Dyke. A modeling approach to determining the relationship between erosion and soil productivity. *Transactions of the ASAE*, 27(1):129–144, 1984. doi: 10.13031/2013.32748.

[42] Jeffrey G. Arnold, Raghavan Srinivasan, Raghavan S. Muttiah, and James R. Williams. Large area hydrologic modeling and assessment part i: Model development. *Journal of the American Water Resources Association*, 34(1):73–89, 1998. doi: 10.1111/j.1752-1688.1998.tb05961.x.

[43] Michael B. Abbott, Jeffrey C. Bathurst, Jean A. Cunge, Patrick E. O'Connell, and Jens Rasmussen. An introduction to the european hydrological system—she, 2: Structure of a physically based, distributed modelling system. *Journal of Hydrology*, 87(1–2):61–77, 1986. doi: 10.1016/0022-1694(86)90115-2.

[44] Jens C. Refsgaard, Morten Thorsen, Jens B. Jensen, S. Kleeschulte, and Søren Hansen. Large scale modelling of groundwater contamination from nitrate leaching. *Journal of Hydrology*, 221(3–4):117–140, 1999. doi: 10.1016/S0022-1694(99)00081-5.

[45] Chinnasamy Santhi, Jeffrey G. Arnold, James R. Williams, William A. Dugas, Raghavan Srinivasan, and Larry M. Hauck. Validation of the SWAT model on a large river basin with point and nonpoint sources. *Journal of the American Water Resources Association*, 37(5):1169–1188, 2001. doi: 10.1111/j.1752-1688.2001.tb03630.x.

[46] Philip W. Gassman, Miguel R. Reyes, C. H. Green, and Jeffrey G. Arnold. The soil and water assessment tool: Historical development, applications, and future research directions. *Transactions of the ASABE*, 50(4):1211–1250, 2007. doi: 10.13031/2013.23637.

[47] Pasquale Steduto, Theodore C. Hsiao, Dirk Raes, and Elias Fereres. Aquacrop—the FAO crop model to simulate yield response to water. *Agronomy Journal*, 101(3):426–437, 2009. doi: 10.2134/agronj2008.0139s.

[48] Richard G. Allen, Masahiro Tasumi, and Ricardo Trezza. Satellite-based energy balance for mapping evapotranspiration. *Journal of Irrigation and Drainage Engineering*, 133(4):380–394, 2007. doi: 10.1061/(ASCE)0733-9437(2007)133:4(380).

[49] Qiaozhen Mu, Maosheng Zhao, and Steven W. Running. Improvements to a modis global terrestrial evapotranspiration algorithm. *Remote Sensing of Environment*, 115(8):1781–1800, 2011. doi: 10.1016/j.rse.2011.02.019.

[50] Alberte Bondeau, Pete C. Smith, and Sönke Zaehle. Modelling the role of agriculture for the 20th century global terrestrial carbon balance. *Global Change Biology*, 13(3):679–706, 2007. doi: 10.1111/j.1365-2486.2006.01305.x.

[51] Sebastian Rost, Dieter Gerten, and Alberte Bondeau. Agricultural green and blue water consumption and its influence on the global water system. *Water Resources Research*, 44:W09405, 2008. doi: 10.1029/2007WR006331.

[52] Hester Biemans, Ingjerd Haddeland, and Pavel Kabat. Impact of reservoirs on river discharge and irrigation water supply during the 20th century. *Water Resources Research*, 47:W03509, 2011. doi: 10.1029/2009WR008929.

[53] Dieter Gerten, Jens Heinke, and Holger Hoff. Global water availability and requirements for future food production. *Journal of Hydrometeorology*, 12(5): 885–899, 2011. doi: 10.1175/2011JHM1328.1.

[54] Grey S. Nearing, Frederik Kratzert, and Markus Reichstein. Machine learning and process-based modeling: Physical insights and synergies. *Hydrology and Earth System Sciences*, 25:1343–1374, 2021. doi: 10.5194/hess-25-1343-2021.

[55] Chaopeng Shen. A transdisciplinary review of deep learning research and its relevance for water resources scientists. *Water Resources Research*, 54(11): 8558–8593, 2018. doi: 10.1029/2018WR022643.

[56] L. P. H. van Beek and Marc F. P. Bierkens. The global hydrological model PCR-GLOBWB: Conceptualization, parameterization and verification. *Hydrology and Earth System Sciences*, 15:273–293, 2011. doi: 10.5194/hess-15-273-2011.

[57] Royal Meteorological Society (Great Britain). Weather prediction by numerical process. by lewis f. richardson. cambridge (university press), 1922. 4°. pp. xii + 236. 30s. net. *Quarterly Journal of the Royal Meteorological Society*, 48 (203):282–284, 1922. Web.

[58] William P. Elliott and Diane J. Gaffen. On the utility of radiosonde humidity archives for climate studies. *Bulletin of the American Meteorological Society*, 72(10):1507–1520, 1991. doi: 10.1175/1520-0477(1991)072<1507:OTUORH>2.0.CO;2.

[59] Y. Mintz and Victor P. Starr. A hemispheric study of the atmospheric water balance. *Monthly Weather Review*, 79(6):151–159, 1951. doi: 10.1175/1520-0493_1951_079_0151_AHSOTW_2_0_CO_2.

[60] Gene S. Benton and Mariano A. Estoque. Water-vapor transfer over the north american continent. *Journal of Meteorology*, 11(6):462–477, 1954. doi: 10.1175/1520-0469(1954)011<0462:WVTOTN>2.0.CO;2.

[61] John W. Hutchings. Water-vapor transfer over the australian region. *Journal of the Atmospheric Sciences*, 18(5):615–630, 1961. doi: 10.1175/1520-0469(1961)018<0615:WVTOTA>2.0.CO;2.

[62] E.M. Rasmusson. Atmospheric water vapor transport and the water balance of north america: Part i. *Monthly Weather Review*, 99(2):119–135, 1967. doi: 10.1175/1520-0493(1971)099<0119:AOAWTI>2.3.CO;2.

[63] Eugene M. Rasmusson. Atmospheric water vapor transport and the water balance of north america. ii: Large-scale water balance investigations. *Monthly Weather Review*, 96(10):720–734, 1968. doi: 10.1175/1520-0493(1968)096<0720:AWVTAT>2.0.CO;2.

[64] Victor P. Starr, Jose P. Peixoto, and Alfred R. Crisi. Hemispheric water balance for the igy. *Tellus*, 17(4):463–472, 1965. doi: 10.3402/tellusa.v17i4.9163.

[65] Jose P. Peixoto. Pole to pole divergence of water vapor. *Tellus*, 22(1):17–25, 1970. doi: 10.3402/tellusa.v22i1.10154.

[66] Andreas Stohl, Gerhard Wotawa, Petra Seibert, and Helga Kromp-Kolb. Interpolation errors in wind fields as a function of spatial and temporal resolution and their impact on different types of kinematic trajectories. *Journal of Applied Meteorology*, 34(10):2149–2165, 1995. doi: 10.1175/1520-0450(1995)034<2149:IEIWFA>2.0.CO;2.

[67] Andreas Stohl. Computation, accuracy and applications of trajectories—a review. *Atmospheric Chemistry and Physics*, 8(17):6595–6630, 1998. doi: 10.5194/acp-8-6595-2008.

[68] Andreas Stohl and Paul James. A lagrangian analysis of the moisture pathways into the amazon basin. *Journal of Geophysical Research*, 110:D21102, 2005. doi: 10.1029/2004JD005608.

[69] Harald Sodemann, Cornelia Schwierz, and Heini Wernli. Interannual variability of greenland winter precipitation sources: Lagrangian moisture diagnostic and north atlantic oscillation influence. *Journal of Geophysical Research: Atmospheres*, 113:D03107, 2008. doi: 10.1029/2007JD008503.

[70] Luis Gimeno, Andreas Stohl, Ricardo M. Trigo, Francina Dominguez, Kei Yoshimura, and L. Yu. Oceanic and terrestrial sources of continental precipitation. *Climate Dynamics*, 35:753–773, 2010. doi: 10.1007/s00382-010-0953-9.

[71] Animesh K. Gain, Walter W. Immerzeel, Frederiek C. Sperna Weiland, and Marc F. P. Bierkens. Impact of climate change on the stream flow of the lower brahmaputra: trends in high and low flows based on discharge-weighted ensemble modelling. *Hydrology and Earth System Sciences*, 15(5):1537–1545, 2011. doi: 10.5194/hess-15-1537-2011. URL https://hess.copernicus.org/articles/15/1537/2011/.

[72] Heini Wernli and Huw C. Davies. A lagrangian-based analysis of extratropical cyclones. i: The method and some applications. *Quarterly Journal of the Royal Meteorological Society*, 123(538):467–489, 1997. doi: 10.1002/qj.49712353811.

[73] Ruud J. van der Ent and Obbe A. Tuinenburg. Oceanic and terrestrial sources of continental precipitation. *Geoscientific Model Development*, 6(5):2049–2062, 2013. doi: 10.5194/gmd-6-2049-2013.

[74] Francina Dominguez, Gonzalo Miguez-Macho, and Huancui Hu. Wrf with water vapor tracers: A study of moisture sources for the north american monsoon. *Journal of Hydrometeorology*, 17(7):1915 – 1927, 2016. doi:

10.1175/JHM-D-15-0221.1. URL https://journals.ametsoc.org/view/journals/hydr/17/7/jhm-d-15-0221_1.xml.

[75] Gianpaolo Balsamo, Clément Albergel, Anton Beljaars, Souhail Boussetta, Eric Brun, Hannah Cloke, Dick Dee, Emanuel Dutra, Joaquín Muñoz-Sabater, Florian Pappenberger, Patricia de Rosnay, Timothy Stockdale, and Frédéric Vitart. Era-interim/land: a global land surface reanalysis data set. *Hydrology and Earth System Sciences*, 19:389–407, 2015. doi: 10.5194/hess-19-389-2015. URL https://hess.copernicus.org/articles/19/389/2015/.

[76] Hans Hersbach, Bill Bell, Paul Berrisford, et al. The era5 global reanalysis. *Quarterly Journal of the Royal Meteorological Society*, 146(730):1999–2049, 2020. doi: 10.1002/qj.3803.

[77] Alexandra Winschall, Stephan Pfahl, Harald Sodemann, and Heini Wernli. Comparison of eulerian and lagrangian moisture source diagnostics – the flood event in eastern europe in may 2010. *Atmospheric Chemistry and Physics*, 14: 6605–6619, 2014. doi: 10.5194/acp-14-6605-2014.

[78] David Noone and Ian Simmonds. Isotopic composition of global precipitation simulated by a general circulation model. *Journal of Geophysical Research*, 109:D06115, 2004. doi: 10.1029/2004JD004803.

[79] Camille Risi, Sandrine Bony, and Françoise Vimeux. Understanding the sahelian water budget through the isotopic composition of water vapor and precipitation. *Journal of Geophysical Research*, 115:D24110, 2010. doi: 10.1029/2010JD014545.

[80] Martin Werner, Petra M. Langebroek, T. Carlsen, Markus Herold, and Gerrit Lohmann. Atmospheric water vapour isotopes in echam5-wiso — part 1: Model description and validation. *Geoscientific Model Development*, 4:111–133, 2011. doi: 10.5194/gmd-4-111-2011.

[81] Franziska Aemisegger, Stephan Pfahl, Harald Sodemann, Iris Lehner, and Heini Wernli. Deuterium excess as a proxy for continental moisture recycling and plant transpiration. *Atmospheric Chemistry and Physics*, 14:4029–4054, 2014. doi: 10.5194/acp-14-4029-2014.

[82] Elke Suess, Franziska Aemisegger, Jeroen E. Sonke, Michael Sprenger, Heini Wernli, and Lenny H.E. Winkel. Marine versus continental sources of iodine and selenium in rainfall at two european high-altitude locations. *Environmental Science & Technology*, 53(4):1905–1917, 2019. doi: 10.1021/acs.est.8b05533. URL https://pubs.acs.org/doi/10.1021/acs.est.8b05533.

[83] Masaki Satoh, Tetsuya Matsuno, Hiroyuki Tomita, Hiroshi Miura, Takemura Nasuno, and Shigeru Iga. Nonhydrostatic icosahedral atmospheric model (nicam) for global cloud resolving simulations. *Journal of Computational Physics*, 227(7):3486–3514, 2008. doi: 10.1016/j.jcp.2007.02.006. URL https://www.sciencedirect.com/science/article/abs/pii/S0021999107000654.

[84] Stephan Pfahl, Heini Wernli, and Kei Yoshimura. The isotopic composition of precipitation from a winter storm – a case study with the limited-area model cosmoiso. *Atmospheric Chemistry and Physics*, 12:1629–1648, 2012. doi: 10.5194/acp-12-1629-2012.

[85] Bjorn Stevens, Masaki Satoh, and Ludovic Auger. Dyamond: The dynamics of the atmospheric general circulation modeled on non-hydrostatic domains. *Bulletin of the American Meteorological Society*, 2019. doi: 10.1175/BAMS-D-19-0124.1.

[86] Johann H. Jungclaus, Stephan J. Lorenz, Hauke Schmidt, Victor Brovkin, Nils Brüggemann, Fatemeh Chegini, Tobias Crüger, Philipp De-Vrese, Veronika Gayler, Marco A. Giorgetta, Oliver Gutjahr, Helmuth Haak, Stefan Hagemann, Markus Hanke, Tatiana Ilyina, Peter Korn, Jörg Kröger, Louisa Linardakis, Christian Mehlmann, Uwe Mikolajewicz, Wolfgang A. Müller, Julia E. M. S. Nabel, Dirk Notz, Holger Pohlmann, Dian A. Putrasahan, Thomas Raddatz, Lars Ramme, Rene Redler, Christian H. Reick, Thomas Riddick, Titus Sam, Ralf Schneck, Reiner Schnur, Michael Schupfner, Jan-Simon von Storch, Felix Wachsmann, Karl-Heinz Wieners, Florian Ziemen, Bjorn Stevens, Jochem Marotzke, and Martin Claussen. The icon earth system model version 1.0. *Journal of Advances in Modeling Earth Systems*, 2022. doi: 10.1029/2021MS002813. URL https://agupubs.onlinelibrary.wiley.com/doi/full/10.1029/2021MS002813.

[87] Marat F. Khairoutdinov. Global system for atmospheric modeling: Model description and preliminary results. *Journal of Advances in Modeling Earth Systems*, 2022. doi: 10.1029/2021MS002968. URL https://agupubs.onlinelibrary.wiley.com/doi/abs/10.1029/2021MS002968.

[88] R. Koster, J. Jouzel, R. Suozzo, G. Russell, W. Broecker, D. Rind, and P. Eagleson. Global sources of local precipitation as determined by the nasa/giss gcm. *Geophysical Research Letters*, 13:121–124, 1986. doi: 10.1029/GL013i002p00121.

[89] Harald Sodemann, Cornelia Schwierz, and Heini Wernli. Sources of water vapour contributing to the elbe flood in august 2002—a tagging study in a mesoscale model. *Quarterly Journal of the Royal Meteorological Society*, 135 (638):205–223, 2009. doi: 10.1002/qj.374.

[90] Obbe A. Tuinenburg and Arie Staal. Tracking the global flows of atmospheric moisture and associated uncertainties. *Hydrology and Earth System Sciences*, 24(5):2419–2435, 2020. doi: 10.5194/hess-24-2419-2020.

[91] F. Dominguez, G. Miguez-Macho, and H. Hu. Wrf with water vapor tracers: A study of moisture sources for the north american monsoon. *Journal of Hydrometeorology*, 17:1915–1927, 2016. doi: 10.1175/JHM-D-15-0221.1.

[92] Andreas Stohl and Paul James. A lagrangian analysis of the moisture source for precipitation. *Journal of Climate*, 17(24):5041–5056, 2004. doi: 10.1175/1520-0442(2004)017<5041:MTOTWA>2.0.CO;2.

[93] Hans Hersbach, Bill Bell, Paul Berrisford, Gianpaolo Biavati, András Horányi, Joaquín Muñoz-Sabater, Julien Nicolas, Claire Peubey, Raluca Radu, Iryna Rozum, David Schepers, Adrian Simmons, Cornel Soci, Dick Dee, and Jean-Noël Thépaut. Era5 hourly data on single levels from 1940 to present. *Copernicus Climate Change Service (C3S)*, 2023. doi: 10.24381/cds.adbb2d47.

[94] Harald Sodemann. Beyond turnover time: Constraining the lifetime distribution of water vapor from simple and complex approaches. *Journal of the Atmospheric Sciences*, 77(2):413–433, 2020. doi: 10.1175/JAS-D-18-0336.1.

[95] Kevin E. Trenberth, John T. Fasullo, and Jessica Mackaro. Atmospheric moisture transports from ocean to land and global energy flows in reanalyses. *Journal of Climate*, 24(18):4907–4924, 2011. doi: 10.1175/2011JCLI4171.1. URL https://journals.ametsoc.org/view/journals/clim/24/18/2011jcli4171.1.xml.

[96] Kenneth P. Bowman. Large-scale isentropic mixing diagnosed from wind and tracer fields. *Journal of the Atmospheric Sciences*, 50(21):3367–3379, 1993. doi: 10.1175/1520-0469(1993)050<3367:LSIMDF>2.0.CO;2.

[97] M. L. Roderick and G. D. Farquhar. A simple framework for comparing the forward and backward lagrangian approaches to modelling the atmospheric moisture budget. *Journal of Hydrology*, 373(3–4):334–341, 2009. doi: 10.1016/j.jhydrol.2009.04.015.

[98] Yinglin Mu, Jason P. Evans, Andrea S. Taschetto, and Chiara Holgate. Refining the lagrangian approach for moisture source identification through sensitivity testing of assumptions using btrims1.1. *Geoscientific Model Development*, 19:1367–1385, 2026. doi: 10.5194/gmd-19-1367-2026.

[99] Paul A. Dirmeyer and K. L. Brubaker. A re-examination of the moisture sources for precipitation. *Journal of Climate*, 12(5):1357–1366, 1999. doi: 10.1175/1520-0442(1999)012<1357:AROTMT>2.0.CO;2.

[100] Luis Gimeno, Andreas Stohl, Ricardo M. Trigo, Francina Dominguez, Kei Yoshimura, Lisan Yu, Anita Drumond, Ana M. Durán-Quesada, and Raquel Nieto. Oceanic and terrestrial sources of continental precipitation. *Reviews of Geophysics*, 50:RG4003, 2012. doi: 10.1029/2012RG000389.

[101] Tove Rudebeck. Introducing corporate water stewardship in the context of global water governance. *Water Governance: Concepts, Methods, and Practice*, 2019. doi: 10.1007/978-3-030-13225-5_1.

[102] Asit K. Biswas and Cecilia Tortajada. Future water governance: Problems and perspectives. *Water Resources Development*, 26(2):129–139, 2010. doi: 10.1080/07900627.2010.488853.

[103] FAO. Water auditing/water governance analysis – governance and policy support: Methodological framework. 2024. doi: https://doi.org/10.4060/cc8993en.

[104] Martijn Cherlet, Charlie Hutchinson, James Reynolds, Jenny Hill, Sabine Sommer, and Graham von Maltitz, editors. *World Atlas of Desertification: Rethinking Land Degradation and Sustainable Land Management*. Publications Office of the European Union, 2018. doi: 10.2760/06292.

[105] H. Charles J. Godfray, John R. Beddington, Ian R. Crute, Lawrence Haddad, David Lawrence, James F. Muir, Jules Pretty, Sherman Robinson, Sandy M. Thomas, and Camilla Toulmin. Food security: The challenge of feeding 9 billion people. *Science*, 327:812–818, 2010. doi: 10.1126/science.1185383.

[106] John S. Wallace. Increasing agricultural water use efficiency to meet future food production. *Agriculture, Ecosystems and Environment*, 82:105–119, 2000. doi: 10.1016/S0167-8809(00)00220-6.

[107] Stephan Pfister, Peter Bayer, Annette Koehler, and Stefanie Hellweg. Projected water consumption in future global agriculture: Scenarios and related impacts. *Science of the Total Environment*, 409(20):4206–4216, 2011. doi: 10.1016/j.scitotenv.2011.07.019.

[108] Elisabeth Vogel, Markus G. Donat, Lisa V. Alexander, Malte Meinshausen, Deepak K. Ray, David Karoly, Nicolai Meinshausen, and Katja Frieler. The effects of climate extremes on global agricultural yields. *Environmental Research Letters*, 14(5), 2019. doi: 10.1088/1748-9326/ab154b.

[109] Zbigniew W. Kundzewicz. Climate change impacts on the hydrological cycle. *Ecohydrology and Hydrobiology*, 8:195–203, 2008. doi: 10.2478/v10104-009-0015-y.

[110] Jakob Stagl, Erich Mayr, Holger Koch, Fred F. Hattermann, and Shaohong Huang. Effects of climate change on the hydrological cycle in central and eastern europe. In *Managing Protected Areas in Central and Eastern Europe Under Climate Change*, volume 58 of *Advances in Global Change Research*. Springer, 2014. doi: 10.1007/978-94-007-7960-0_3.

[111] Jian Ma, Lei Zhou, Gregory R. Foltz, Xia Qu, Jun Ying, Hiroki Tokinaga, Carlos R. Mechoso, Jinbao Li, and Xingyu Gu. Hydrological cycle changes under global warming and their effects on multiscale climate variability. *Annals of the New York Academy of Sciences*, pages 1–17, 2020. doi: 10.1111/nyas.14335.

[112] Xin Wang and Lei Liu. The impacts of climate change on the hydrological cycle and water resource management. *Water*, 15(13):2342, 2023. doi: 10.3390/w15132342.

[113] Christa D. Peters-Lidard, Kevin C. Rose, Julie E. Kiang, Michael L. Strobel, Michael L. Anderson, Aaron R. Byrd, Michael J. Kolian, Levi D. Brekke, and Derek S. Arndt. Indicators of climate change impacts on the water cycle and water management. *Climatic Change*, 165(36), 2021. doi: 10.1007/s10584-021-03057-5.

[114] Gunter Wriedt, Marijn van der Velde, Alberto Aloe, and Fayçal Bouraoui. Estimating irrigation water requirements in europe. *Journal of Hydrology*, 373(3–4):527–544, 2009. doi: 10.1016/j.jhydrol.2009.05.018.

[115] FAO and OECD. The assessment of climate change-related vulnerability in the agricultural sector: reviewing conceptual frameworks. 2012. doi: 10.13140/2.1.4314.8809.

[116] EUCAP-Network. Agricultural rural inspiration awards (aria). *EU CAP Network*, 2023. URL https://eu-cap-network.ec.europa.eu/news/agriculture-rural-inspiration-awards-aria-2023_en.

[117] EUCAP-Network. Water efficiency benefits flow from cap strategic plans. *EU CAP Network*, pages 1–172, 2024. URL https://eu-cap-network.ec.europa.eu/news/water-efficiency-benefits-flow-cap-strategic-plans_en.

[118] Ayami Hayashi, Keigo Akimoto, Toshimasa Tomoda, and Masanobu Kii. Global evaluation of the effects of agriculture and water management adaptations on the water-stressed population. *Mitigation and Adaptation Strategies for Global Change*, 18:591–618, 2013. doi: 10.1007/s11027-012-9377-3.

[119] Luis Santos Pereira. Agriculture and food: Challenges and issues. *Water Resources Management*, 31:2985–2999, 2017. doi: 10.1007/s11269-017-1664-z.

[120] Juan Antonio Rodríguez Díaz, Rafael González Perea, and Miguel Ángel Moreno. Modelling and management of irrigation systems. *Water*, 12(3), 2020. doi: 10.3390/w12030697.

[121] Laurent Maton, Denis Leenhardt, Michel Goulard, and Jean-Emmanuel Bergez. Assessing the irrigation strategies over a wide geographical area from structural data about farming systems. *Agricultural Systems*, 86(3):293–311, 2005. doi: 10.1016/j.agsy.2004.09.010.

[122] Juan J. Cancela, Tomás S. Cuesta, Xosé X. Neira, and Luis S. Pereira. Modelling for improved irrigation water management in a temperate region of northern spain. *Biosystems Engineering*, 94(1):151–163, 2006. doi: 10.1016/j.biosystemseng.2006.02.010.

[123] Ajay Singh. Irrigation planning and management through optimization modelling. *Water Resources Management*, 28:1–14, 2014. doi: 10.1007/s11269-013-0469-y.

[124] Luis-Enrique Olivera-Guerra, Pierre Laluet, Víctor Altés, Chloé Ollivier, Yann Pageot, Giovanni Paolini, Eric Chavanon, Vincent Rivalland, Gilles Boulet, Josep-Maria Villar, and Olivier Merlin. Modeling actual water use under different irrigation regimes at district scale: Application to the FAO-56 dual crop coefficient method. *Agricultural Water Management*, 278, 2023. doi: 10.1016/j.agwat.2022.108119.

[125] Mohamed Salman, Manuel García-Vila, Elias Fereres, Dirk Raes, and Pasquale Steduto. The AquaCrop model—enhancing crop water productivity: Ten years of development, dissemination and implementation (2009–2019), 2021.

[126] Joop G. Kroes, Johan C. van Dam, Ruud P. Bartholomeus, Piet Groenendijk, Marcel Heinen, Rob F. A. Hendriks, Henk M. Mulder, Iwan Supit, and Pieter E. V. van Walsum. Swap version 4: Theory description and user manual, 2017.

[127] James W. Jones, Gerrit Hoogenboom, Cheryl H. Porter, Kenneth J. Boote, William D. Batchelor, Leslie A. Hunt, Paul W. Wilkens, Upendra Singh, Abraham J. Gijsman, and Joe T. Ritchie. The DSSAT cropping system model. *European Journal of Agronomy*, 18(3):235–265, 2003. doi: 10.1016/S1161-0301(02)00107-7.

[128] Richard G. Allen, Luis S. Pereira, Dirk Raes, and Martin Smith. Crop evapotranspiration: Guidelines for computing crop water requirements. *FAO Irrigation and Drainage Paper No. 56*, 1998. URL https://www.fao.org/3/X0490E/x0490e00.htm.

[129] An overview of apsim, a model designed for farming systems simulation. *European Journal of Agronomy*, 18(3):267–288, 2003. ISSN 1161-0301. doi: https://doi.org/10.1016/S1161-0301(02)00108-9. URL https://www.sciencedirect.com/science/article/pii/S1161030102001089. Modelling Cropping Systems: Science, Software and Applications.

[130] Claudio O. Stöckle, Marcello Donatelli, and Roger Nelson. Cropsyst, a cropping systems simulation model. *European Journal of Agronomy*, 18(3):289–307, 2003. doi: 10.1016/S1161-0301(02)00109-0.

[131] Willem G. M. Bastiaanssen, Richard G. Allen, Peter Droogers, Guido D'Urso, and Pasquale Steduto. Twenty-five years modeling irrigated and drained soils: State of the art. *Agricultural Water Management*, 92(3):111–125, 2007. doi: 10.1016/j.agwat.2007.05.013.

[132] Naftali Lazarovitch, Isaya Kisekka, Tobias E. Oker, Giuseppe Brunetti, Thomas Wöhling, Xianyue Li, Yong Li, Todd H. Skaggs, Alex Furman, Salini Sasidharan, Iael Raij-Hoffman, and Jiří Šimůnek. Modeling of irrigation and related processes with HYDRUS. In *Advances in Agronomy*, volume 181, pages 79–181. 2023. doi: 10.1016/bs.agron.2023.05.002.

[133] Sibyll Schaphoff, Werner von Bloh, Anja Rammig, Kirsten Thonicke, Hester Biemans, Matthias Forkel, Dieter Gerten, Jens Heinke, Jonas Jägermeyr, Jürgen Knauer, Felix Langerwisch, Wolfgang Lucht, Christoph Müller, Susanne Rolinski, and Katharina Waha. Lpjml4 – a dynamic global vegetation model with managed land – part 1: Model description. *Geoscientific Model Development*, 11:1343–1375, 2018. doi: 10.5194/gmd-11-1343-2018.

[134] Naota Hanasaki, Sayaka Yoshikawa, Yadu Pokhrel, and Shinjiro Kanae. A global hydrological simulation to specify the sources of water used by humans. *Hydrology and Earth System Sciences*, 22:789–817, 2018. doi: 10.5194/hess-22-789-2018.

[135] Davide D. Chiarelli, Chiara Passera, Lorenzo Rosa, Kyle F. Davis, Paolo D'Odorico, and Maria C. Rulli. The green and blue crop water requirement WATNEEDS model and its global gridded outputs. *Scientific Data*, 7(273), 2020. doi: 10.1038/s41597-020-00612-0.

[136] Petra Döll and Stefan Siebert. Global modeling of irrigation water requirements. *Water Resources Research*, 38(4), 2002. doi: 10.1029/2001WR000355.

[137] Marta Tuninetti, Stefania Tamea, Paolo D'Odorico, Francesco Laio, and Luca Ridolfi. Global sensitivity of high-resolution estimates of crop water footprint. *Water Resources Research*, 51:8257–8272, 2015. doi: 10.1002/2015WR017148.

[138] Raymond D. Jackson, Jerry L. Hatfield, Robert J. Reginato, Sherwood B. Idso, and Jr. Pinter, Paul J. Estimation of daily evapotranspiration from one-time-of-day measurements. *Agricultural Water Management*, 7(3):351–362, 1983. doi: 10.1016/0378-3774(83)90095-1.

[139] Francesco Laio, Amilcare Porporato, Luca Ridolfi, and Ignacio Rodriguez-Iturbe. Plants in water-controlled ecosystems: active role in hydrologic processes and response to water stress ii. probabilistic soil moisture dynamics. *Advances in Water Resources*, 24:707–723, 2002. doi: 10.1016/S0309-1708(01)00005-7.

[140] ISTAT. 6^th general agricultural census: Use of water resources for irrigation purpuses in agriculture (6° censimento generale dell'agricoltura: Utilizzo della risorsa idrica a fini irrigui in agricoltura). *STEALTH*, 2014. URL https://www.istat.it/it/files//2014/11/Utilizzo_risorsa_idrica.pdf.

[141] Ian Harris, Timothy J. Osborn, Phil Jones, and David Lister. Version 4 of the CRU TS monthly high-resolution gridded multivariate climate dataset. *Scientific Data*, 7:1–18, 2020. doi: 10.1038/s41597-020-0453-3.

[142] Mesfin M. Mekonnen and Arjen Y. Hoekstra. The green, blue and grey water footprint of crops and derived crop products. *Hydrology and Earth System Sciences*, 15:1577–1600, 2011. doi: 10.5194/hess-15-1577-2011.

[143] Guenther Fischer, Freddy Nachtergaele, Stefan Prieler, Harrij T. van Velthuizen, Laxmi Verelst, and David Wiberg. Global agro-ecological zones assessment for agriculture. *IIASA*, 2008. URL https://www.fao.org/soils-portal/data-hub/soil-maps-and-databases/harmonized-world-soil-database-v12/en/.

[144] Roger B. Clapp and George M. Hornberger. Empirical equations for some soil hydraulic properties. *Water Resources Research*, 14(4):601–604, 1978. doi: 10.1029/WR014i004p00601.

[145] MIPAAF. Metodologia di stima degli utilizzi e delle restituzioni. Technical report, Ministry of Agriculture, Food Sovereignty and Forestry, 2016.

[146] Luis S. Pereira, Pedro Paredes, Forrest Melton, Lila Johnson, Tingting Wang, Rodrigo López-Urrea, Juan J. Cancela, and Richard G. Allen. Prediction of crop coefficients from fraction of ground cover and height: Background and validation using ground and remote sensing data. *Agricultural Water Management*, 241, 2020. doi: 10.1016/j.agwat.2020.106197.

[147] Felix T. Portmann, Stefan Siebert, and Petra Döll. Mirca2000—global monthly irrigated and rainfed crop areas around the year 2000: A new high-resolution data set for agricultural and hydrological modeling. *Global Biogeochemical Cycles*, 24, 2010. doi: 10.1029/2008GB003435.

[148] Francesco Lupia, Simone Vanino, Francesco De Santis, and Nicola Laruccia. A model-based irrigation water consumption estimation at farm level. *INEA*, 2013.

[149] Nader Katerji, Pasquale Campi, and Marcello Mastrorilli. Productivity, evapotranspiration, and water use efficiency of corn and tomato crops simulated by AquaCrop under contrasting water stress conditions in the mediterranean region. *Agricultural Water Management*, 130:14–26, 2013. doi: 10.1016/j.agwat.2013.08.005.

[150] Davide Bocchiola, Elisa Nana, and Andrea Soncini. Impact of climate change scenarios on crop yield and water footprint of maize in the po valley of italy. *Agricultural Water Management*, 116:50–61, 2013. doi: 10.1016/j.agwat.2012.10.009.

[151] Roberto Casa, Massimo Rossi, and Gabriele Sappa. Assessing crop water demand by remote sensing and GIS for the pontina plain, central italy. *Water Resources Management*, 23:1685–1712, 2009. doi: 10.1007/s11269-008-9347-4.

[152] Francesca Todisco and Lorenzo Vergni. Climatic changes in central italy and their potential effects on corn water consumption. *Agricultural and Forest Meteorology*, 148(1):1–11, 2008. doi: 10.1016/j.agrformet.2007.08.014.

[153] ISPRA. Indicators of italian climate in 2020 (gli indicatori del clima in italia del 2020). 2021. URL https://www.isprambiente.gov.it/it/pubblicazioni/stato-dellambiente/rapporto_clima_2020-1.pdf.

[154] Erika Coppola and Filippo Giorgi. An assessment of temperature and precipitation change projections over italy from recent global and regional climate model simulations. *International Journal of Climatology*, 30:11–32, 2010. doi: 10.1002/joc.1867.

[155] Andreas Gobiet, Sven Kotlarski, Martin Beniston, Georg Heinrich, Jan Rajczak, and Markus Stoffel. 21st century climate change in the european alps—a review. *Science of the Total Environment*, 493:1138–1151, 2014. doi: 10.1016/j.scitotenv.2013.07.050. URL https://doi.org/10.1016/j.scitotenv.2013.07.050.

[156] Mariapina Castelli. Evapotranspiration changes over the european alps: Consistency of trends and their drivers between the mod16 and ssebop algorithms. *Remote Sensing*, 13(21):4316, 2021. doi: 10.3390/rs13214316. URL https://www.mdpi.com/2072-4292/13/21/4316.

[157] Matthias Herrnegger, Hans-Peter Nachtnebel, and Thomas Haiden. Evapotranspiration in high alpine catchments – an important part of the water balance. *Hydrology Research*, 43(4):460–475, 2012. doi: 10.2166/nh.2012.132.

[158] Yifan Jiao, Guofang Zhu, Di Qiu, Sheng Lu, Guo Meng, Rui Li, Qiang Wang, Lei Chen, and Wei Li. Variations in vegetation evapotranspiration affect water yield in high-altitude areas. *Biogeosciences*, 22:4433–4448, 2025. doi: 10.5194/bg-22-4433-2025.

[159] Zhihua Zhang, Qiudong Zhao, and Shiqiang Zhang. Abundant precipitation in qilian mountains generated from the recycled moisture over the adjacent arid hexi corridor, northwest china. *Water*, 13(23):3354, 2021. doi: 10.3390/w13233354. URL https://doi.org/10.3390/w13233354.

[160] Xuefeng Guan, Caleb Langhamer, David Schneider, et al. Lagrangian analysis of moisture sources of precipitation in the tianshan mountains, central asia. *Earth and Space Science*, 9(2):e2022EA002318, 2022. doi: 10.1029/2022EA002318. URL https://doi.org/10.1029/2022EA002318.

[161] Beiming Kang, Yan Ren, Yang Shi, Xiaomei Zhu, Jingjing Huang, and Wenwen Bai. Quantifying moisture source contributions to diverse precipitation events over the tibetan plateau. *Water*, 17(24):3587, 2025. doi: 10.3390/w17243587. URL https://doi.org/10.3390/w17243587.

[162] Alessio Berto, Dino Zardi, and Alberto Buzzi. Back-tracking water vapour contributing to a precipitation event over trentino: a case study. *Meteorologische Zeitschrift*, 13(3), 2004. doi: 10.1127/0941-2948/2004/0013-0189. URL https://doi.org/10.1127/0941-2948/2004/0013-0189.

[163] Harald Sodemann and Elias Zubler. Seasonal and inter-annual variability of the moisture sources for alpine precipitation during 1995–2002. *International Journal of Climatology*, 30:947–961, 2009. doi: 10.1002/joc.1932.

[164] Elena De Petrillo, Simon Fahrländer, Marta Tuninetti, Lauren Andersen, Francesco Laio, and Luca Ridolfi. Reconciling tracked atmospheric water flows to close the global freshwater cycle, 2024.

[165] Joaquín Muñoz-Sabater, Emanuel Dutra, Anna Agustí-Panareda, Clément Albergel, Gabriele Arduini, Gianpaolo Balsamo, Souhail Boussetta, Margarita Choulga, Shaun Harrigan, Hans Hersbach, Brecht Martens, Diego G. Miralles, María Piles, Nemesio J. Rodríguez-Fernández, Ervin Zsoter, Carlo Buontempo, and Jean-Noël Thépaut. Era5-land: A state-of-the-art global reanalysis dataset for land applications. *Earth System Science Data*, 13(9):4349–4383, 2021. doi: 10.5194/essd-13-4349-2021.

[166] Gökhan Sarigil, Mattia Neri, and Elena Toth. Evaluation of national and international gridded meteorological products for rainfall–runoff modelling in northern italy. *Journal of Hydrology: Regional Studies*, 56:102031, 2024. doi: 10.1016/j.ejrh.2024.102031.

[167] D. Dalla Torre, N. Di Marco, A. Menapace, D. Avesani, M. Righetti, and B. Majone. Suitability of era5-land reanalysis dataset for hydrological modelling in the alpine region. *Journal of Hydrology: Regional Studies*, 52:1–22, 2024. doi: 10.1016/j.ejrh.2024.101718.

[168] Andrea Menapace, Pranav Dhawan, Daniele Dalla Torre, Konstantinos Kaffas, Alice Crespi, Michele Larcher, Maurizio Righetti, and Alex J. Cannon. Review of bias correction methods for climate model outputs in hydrology. *Journal of Hydrology*, 660:133213, 2025. doi: 10.1016/j.jhydrol.2025.133213.

[169] Eurac Research and Permanent Secretariat of the Alpine Convention. Alpine convention perimeter, 2025.

[170] Franziska Aemisegger and Jesper Sjolte. A climatology of strong large-scale ocean evaporation events. part ii: Relevance for the deuterium excess signature of the evaporation flux. *Journal of Climate*, 31:7313–7336, 2018. doi: 10.1175/JCLI-D-17-0592.1.

[171] Ying Li, Chenghao Wang, Qiuhong Tang, Shangbin Xiao, et al. Unraveling the discrepancies between eulerian and lagrangian moisture tracking models in monsoon- and westerly-dominated basins of the tibetan plateau. *Atmospheric Chemistry and Physics*, 24(18):10741–10758, 2024. doi: 10.5194/acp-24-10741-2024.

[172] Juliette Blanchet, Antoine Blanc, and Jean-Dominique Creutin. Explaining recent trends in extreme precipitation in the southwestern alps by changes in atmospheric influences. *Weather and Climate Extremes*, 33:100356, 2021. doi: 10.1016/j.wace.2021.100356.

[173] Stefan K. Müller, Elena Pichelli, Erika Coppola, et al. The climate change response of alpine–mediterranean heavy precipitation events. *Climate Dynamics*, 62:165–186, 2024. doi: 10.1007/s00382-023-06901-9.

[174] Diego G. Miralles et al. Land–atmospheric feedbacks during droughts and heatwaves: State of the science and current challenges. *Annals of the New York Academy of Sciences*, 1436(1):19–35, 2019. doi: 10.1111/nyas.13912.

[175] David L. Schumacher, Jan Keune, Paul Dirmeyer, and Diego G. Miralles. Drought self-propagation in drylands due to land–atmosphere feedbacks. *Nature Geoscience*, 15(4):262–268, 2022. doi: 10.1038/s41561-022-00912-7.

[176] Francesco Avanzi, Simone Gabellani, Francesco Delogu, Francesco Silvestro, Francesca Pignone, Gianluca Bruno, Luca Pulvirenti, Giuseppe Squicciarino, Enrico Fiori, Lorenzo Rossi, Sara Puca, Andrea Toniazzo, Paola Giordano, Mauro Falzacappa, Sara Ratto, Hervé Stevenin, Andrea Cardillo, Marco Fioletti, Olivia Cazzuli, Elena Cremonese, Umberto Morra di Cella, and Luca Ferraris. It-snow: A snow reanalysis for italy blending modeling, in situ data, and satellite observations (2010–2021). *Earth System Science Data*, 15(2): 639–660, 2023. doi: 10.5194/essd-15-639-2023.

[177] Istituto Nazionale di Statistica (ISTAT). *Utilizzo della risorsa idrica a fini irrigui in agricoltura: VI Censimento Generale dell'Agricoltura*. ISTAT, 2014. ISBN 978-88-458-1805-9. URL https://www.istat.it/it/files/2014/11/Utilizzo_risorsa_idrica.pdf.

[178] Christian Bogdal, Peter Schmid, Markus Zennegg, Flavio S. Anselmetti, Martin Scheringer, and Konrad Hungerbühler. Blast from the past: Melting glaciers as a relevant source for persistent organic pollutants. *Environmental Science & Technology*, 43(21):8173–8177, 2009. doi: 10.1021/es901628x.

[179] Claudia Ferrario, Antonio Finizio, and Sara Villa. Contaminants in alpine glaciers: A never-ending story? University of Milano-Bicocca, 2016. URL https://boa.unimib.it/retrieve/e39773b9-4e15-35a3-e053-3a05fe0aac26/Articolo%20Alpi_2016.pdf.

[180] Cristiana Rizzi, Sara Villa, Luca Rossini, Andrea Mustoni, and Valeria Lencioni. Levels and ecological risk of selected organic pollutants in the high-altitude alpine cryosphere: The adamello–brenta natural park (italy) as a case study. *Environmental Advances*, 7:100178, 2022. doi: 10.1016/j.envadv.2022.100178.

[181] Ramesh Kumar, Prity S. Pippal, Alok Raj, and Rajesh Kumar. Toxic contaminants in glacial meltwater and their impact on the environment and human health. *Water Conservation Science and Engineering*, 10:54, 2025. doi: 10.1007/s41101-025-00379-8.

[182] Terry F. Bidleman. Atmospheric transport and air-surface exchange of pesticides. *Water, Air, and Soil Pollution*, 115:115–166, 1999. doi: 10.1023/A:1005249305515.

[183] Kimberly J. Hageman, Staci L. M. Simonich, Donald H. Campbell, Glen R. Wilson, and David H. Landers. Atmospheric deposition of current-use and historic-use pesticides in snow at national parks in the western united states. *Environmental Science & Technology*, 40(10):3174–3180, 2006. doi: 10.1021/es060157c.